Aus der Klinik für Strahlentherapie und Radioonkologie
der Medizinischen Fakultät Mannheim
(Direktor: Prof. Dr. med. Frank Giordano)

An Inverse Treatment Planning System for Robotic Seed Brachytherapy

Inauguraldissertation
zur Erlangung des
Doctor scientiarum humanarum (Dr. sc. hum.)
der
Medizinischen Fakultät Mannheim
der Ruprecht-Karls-Universität
zu
Heidelberg

vorgelegt von

Philipp Aumüller

aus
Augsburg
2023

Dekan: Prof. Dr. med. Sergij Goerdt
Referent: Prof. Dr. med. Frank Giordano

Contents

List of abbreviations

BT Brachytherapy. 2, 3, 5, 6, 8, 9, 15, 25, 30, 33, 39, 46, 60, 62, 66, 70–72, 74, 77, 79

CBCT Cone-Beam Computed Tomography. 10, 12, 78

CT Computed Tomography. 3–5, 16, 38, 59

CTV Clinical Target Volume. 3, 4, 15, 16, 22, 23, 27, 31, 35–37, 43, 46, 49, 52, 54–57, 62, 63, 66, 68, 69, 72, 73, 75

DICOM Digital Imaging and Communications in Medicine. 9, 20, 33, 60, 76

DVH dose-volume histogram. 46, 49, 63

EBRT External-Beam Radiation Therapy. 2, 15, 20, 48, 60, 69, 74, 77

MRI Magnetic Resonance Imaging. 4, 5, 7, 11, 37, 38, 56, 58, 59, 78, 79

NPA needle placement accuracy. 4, 7, 13, 33–35, 48, 51, 54, 57, 68, 69, 74, 80

OAR Organ at Risk. 4, 11, 16, 21, 31, 40, 53, 61, 62, 64, 68, 72, 74

OCP Oncentra Prostate. 9, 11, 12, 15, 20, 39, 41, 60

PTV Planning Target Volume. 3, 6, 41

RCM Remote Control Manipulator. 6, 7, 11, 13, 14, 22, 23, 37, 57, 61, 75, 77

SAA simulated annealing adaption. 13, 33, 35–37, 48, 51, 52, 55

SI simulated implantation. 7, 32–35, 48, 51–53, 68

TPS Treatment Planning System. 5–7, 9, 12, 14, 21, 23, 28, 37, 39, 41, 44, 60, 63, 67, 72, 75, 79

1 Introduction

Brachytherapy (BT) is a well-established therapy option for cancer treatment which roots back to the beginnings of radiotherapy with its first patient treated in 1901 only five years after the discovery of radioactivity in 1896 by Henri Becquerel [1]. The principal idea of curing cancer by the short-range radiation[1] of radionuclides remained the same up to modern state of the art BT.

Innovations in BT were driven by the optimisation of the treatment procedure to enhance patient related treatment outcomes and to reduce the staff's radiation exposure. The latter could be achieved by taking care in radiation protection techniques and choosing the most appropriate radioactive nuclide. Physical properties as the half-life, the radiation type and the dose depth curve in water have to be considered. In the 1910s to 1920s radium, the first radioactive element found, was used for prostate-BT [2]. Later on, a solution of ^{198}Au was implanted to treat prostate cancer by making use of the β^- component of the radioactive decay [3]. In the 1960s, iodine seeds with a low $E_\gamma = 28.37\,\text{keV}$ photon emission were developed in order to maintain a high dose to the tumour while reducing the staff's exposure [4]. The radioactive sources are encapsulated which facilitates their handling and prevents contamination of the operation theatre.

The intraoperative seed implantation was an early technique that got along without any imaging modalities by defining the target volume under sight within the tumour bed. In the 1970s 60 patients underwent intraoperative ^{125}I seed implantations into the prostate [4]. Retro pubic open surgery was used to stage the prostate cancer and then proceed with lymphadenectomy and seed implantation. The prostate size was estimated by the tumour bed and the needle path-length into the prostate to estimate the total activity needed for tumour control. The seeds were then implanted with 1 cm distance to each other. Because of the lack of intraoperative imaging, the needle tip was sensed with the physician's finger to prevent puncturing the rectum wall. From the 80s to the early 2000s intraoperative seed-BT was prescribed for unresectable pancreatic cancers [5, 6], lung cancer [7], liver metastases [8] as well as tumours causing spinal cord compression [9].

State of the art prostate Brachytherapy With the innovations in External-Beam Radiation Therapy (EBRT) conformal irradiation of the tumour without the need of surgery and anaesthesia were possible and BT had declining importance except for prostate BT. For the latter, a distinction is made between high-dose rate afterloading-BT (HDRBT) and low-dose rate seed-BT for prostate cancer. The afterloader seals the radiation source and is able to release it remotely with a wire, when the staff left the operation theatre. Nowadays, it used with a ^{192}Ir source temporarily irradiating the clinical target volume with a dose rate exceeding $12\,\frac{\text{Gy}}{\text{h}}$ [10]. Prostate seed-BT in contrast is called low-dose-rate (LDR) BT with a dose rate of less than $2\,\frac{\text{Gy}}{\text{h}}$. Both HDR BT and LDR BT can be applied as monotherapy or in combination with EBRT and lead to good treatment outcomes [11–14]. However, this thesis focuses on the use of seeds in LDR BT.

[1] "brachys" is short in Greece

Prostate seed-BT is a minimally invasive therapy option for early staged prostate carcinoma [15]. The modern approach is based on permanent implantation of stranded seeds in the prostate through a template grid, which is mounted to the transrectal ultrasound (TRUS) imaging device [16]. The latter is used for live imaging and intraoperative treatment planning. Antigen free survival outcomes in a comparative study for low and intermediate risk prostate carcinoma are shown to be higher than EBRT and surgery suggesting an excellent local tumour control [12]. Alongside a questionnaire to patients that underwent seed-BT in the local therapy department resulted in favourable long-term quality of life outcomes with an follow up after a median of 51 and 141 months respectively [17, 18].

The workflow starts with the acquisition of the 3D-TRUS image set which is contoured in the operation theatre. An inverse optimizer calculates the treatment plan defining the needle trajectories through the fixed template and the number of seeds used. The physicist optionally refines this plan by adjusting the insertion depth of the needles or by adding or removing seeds. These two steps are termed as intraoperative and interactive planning respectively [19]. The needles are then implanted under live TRUS imaging. The live needle position can be registered to update the live dose distribution, which is termed as dynamic dose calculation in [19]. The physician is then able do decide whether the seeds are released or the needle is repositioned. An underdosage of the target volume can be prevented by implanting additional needles at the end of the procedure. One day and six weeks after the implantation a Computed Tomography (CT) scan is acquired for quality assurance of the implant. In the past, seed migration was a common problem where mostly single loose seeds show pulmonary, distal toward the perineum or seminal vesicles migration after implantation. This effect could be minimized by using stranded seeds [20].

The therapy options for prostate seed-BT depend on the prostate carcinoma staging and the risk for distant metastases. For low risk and favourable intermediate risk prostate carcinoma the Clinical Target Volume (CTV) can be prescribed to 145 Gy as the covering isodose in a monotherapy [21]. The CTV here is the whole prostate delineated in the TRUS images plus margins with dose constraints to the urethra in order to prevent incontinence and sexual dysfunction after treatment. For intermediate and localized high-risk prostate carcinoma 115 Gy prescription dose as a boost to the CTV and 40 Gy of EBRT to the Planning Target Volume (PTV) is an alternative to EBRT alone [13].

Fields of modern research Prostate seed-BT is still subject of research. With prostate cancer having a high incidence but a relatively low mortality rate in Europe active surveillance is recommended first for low risk prostate carcinoma to prevent overtreatment [21]. For a curative treatment with less impairments of quality of life focal treatment approaches are investigated where only sub-volumes of the prostate were delineated as target volumes [22–26]. A patient study where only the hemi-gland was prescribed could not show a statistically significant benefit for quality of life [23] and hence even smaller volumes are considered in the ultra-focal approach [26].

However, these smaller target volumes raise the requirements for a successful implant

to the technique and the team. Retrospective simulations comparing the treatment of the whole prostate, the hemi gland or focal F-CTVs have shown the dependence of volume size and shape to seed displacements [22]. The smaller the target the less needles and seeds are used. Their displacement due to inaccurate needle placement and seed release lead to deviations from important dose constraints. It is the D90, the minimal dose of 90 % of the target volume, and V100 accounting for an effective treatment. Therefore, a high needle placement accuracy (NPA) is crucial for a successful and patient sparing treatment. The in-vivo NPA for perineal treatment is estimated to be $3 - 6\,\mathrm{mm}$ [27] and therefore first patient studies were pioneered with rather big safety margins i.e. the F-CTV of $(34 \pm 20)\,\%$ of the prostate volume [28] compromising the goal of focal treatment with a limited implantation accuracy.

It can be seen that the current transperineal TRUS guided implantation procedure is reaching its limits in terms of accuracy and image guidance. The use of new image modalities as the CT and Magnetic Resonance Imaging (MRI) in combination with new robotic assistants as navigation tools could have the potential to facilitate prostate-BT. The robotic automation enables to follow a standardized workflow independent of the tumour site and surrounding Organs at Risk (OARs) which decreases the operator dependence on the implantation quality and hence the safeness. Alongside the precision of placing the needle and the time-efficiency might be optimized. A better image modality could also enable dynamic dose calculations, which is the feedback of the released seeds to the treatment planning system to recalculate the dose distribution [19]. This can lead to novel adaption strategies that are elaborated in this thesis.

Facilitating the treatment procedure further could also solve a structural problem of BT which is the low accessibility of the treatment even in USA and Europe due to the limited number of capable physicians and physicists [29]. The use of this treatment modality is even declining [30] and too less education is done. An automated implantation procedure, a better imaging guidance and adaption to seed displacement could lead to a higher mastery of the procedure by the intervention team. Data shows that the quality of the implant presently highly depends on the experience of the intervention team, which should have accomplished more than 20 prostate seed-BTs under supervision as the associated learning curve suggests [31, 32]. The latter is apparent when analysing the dose coverage over the patient number that increases and then reaches a stable plateau after 20 patients. This can be related with the complex intervention workflow. The TRUS for instance is a challenging modality to delineate the whole prostate without any image artifacts because of missing physical contact to the rectum wall due to air in the rectum. Interestingly, Acher et al. found no learning curve when establishing seed-BT with dynamic dose feedback by registering the released single seeds in the TRUS images [33]. The hypothesized reason next to a proper mentorship program was the ability to adapt the implant with additional needles when needle displacement and a loss of dose coverage occurred. This might indicate that facilitating the implantation procedure by e.g. automation can lead to an easier start for unexperienced teams.

The following two paragraphs describe the current research using new image modalities as the CT and MRI for seed-BT and associated robotic systems.

CT guided interventions With upcoming CT free-hand percutaneous seed implantation was shown inter alia for pancreatic cancer, locoregional recurrent gastric cancer and recurrent spinal primary tumours [34–36]. However, this technique requires an experienced physician to accurately place the needle at the planned position. In addition, the high dose exposure due to the CT guidance is disadvantageous. A more recent approach aims to design surface adapted implantation templates by using 3D printing for coplanar and non-coplanar needles [37, 38]. The template wholes consider the planned trajectories with its injection angle that are placed virtually. With simulated annealing the optimal number of seeds is determined [39].

In a previous study, Smakic et al. showed a higher NPA and time efficiency in comparison to a manual needle placement by using a robotic navigation tool [40]. Rothfuss et al. recently has shown an approach using a robotic arm (guidoo, BEC GmbH, Pfullingen, Germany) that precisely steers an injection template with the correct injection angle to a planned position on the patient's surface [41]. The physician then only needs to inject the biopsy needle. In the AAPM 192 guidelines, such a device is classified as a level II robot. The robot arm is based on the LBR iiwa 14 R820 (KUKA AG, Augsburg, Germany). In a phantom experiment with 16 needle insertions, an experienced interventional radiologist achieved a mean deviation from the target point to tip point of 2.74 mm [42]. The seed's high dose gradient of the low keV photon emission leads to a small dose envelope of the prescription dose around the seed. Therefore, increasing the geometric positioning accuracy and reducing seed displacement due to a higher safeness in the automated workflow result in substantial improvements of the technique. In this thesis the use of this navigation tool is considered for a robotic seed-BT of a liver metastasis in scenario 1 (see Table 1 on 7).

MRI guided interventions The MRI yields the best soft-tissue contrast and the patient and staff are not exposed to radiation. However, the static magnetic field of the system requires MR-safe equipment to use for in-bore interventions. First prostate seed implantations were shown by D'Amico et al. with a real time intraoperative MR imaging unit in 1998 [43]. They used an MR-safe template and MR-imaging to guide the needles to its destination. An in-house developed Treatment Planning System (TPS) was used to contour the volumes and plan the intervention on the MR image data [44]. Issues in this field are given by artifacts due to magnetic field distortions. The MR-safe needle, especially the needle tip and seeds appear as signal voids with no magnetic resonance signal from them. Moreover, the signal voids further appear enlarged due to artifacts resulting from magnetic field disturbance. They complicate the precise localization of needles and seeds. Regardless of this the live needle feedback and the dynamic dose calculation in the interventional MRI was shown by Cormack et al. in [45]. They analysed the axial MRI image near the needle tip in the TPS. The needle tip coordinate was defined as the centre coordinate of the circular signal void. With the coordinate of the template injection-hole, the needle path could be recalculated to update the dose distribution as well as to calculate the needle displacement. They used on average two additional needles to adapt the plan to given needle displacement errors. To overcome

the given uncertainty due to artifacts the latter were as well simulated for a seed at the tip of the needle. This should enable to calculate the precise seed position by identifying the given artifact. Finally, this would enable the feedback of the precise seed position just before its release [46]. The simulations further revealed that the use of a plastic needle reduces the artifact to the seed. The group later focused on simulating HDR iridium sources with the intent to generate lookup tables to register the source position precisely [47, 48]. However, this is a difficult task as the artifacts depend on the magnetic field, which in turn depends on the scan parameters such as acquisition angle.

If stranded seeds are used the problem arises that the seeds are hardly distinguishable from the spacers between the seeds. Nosrati et al. used functional MRI and machine learning algorithms to automatically register the seed positions from stranded seeds in MRI, which would enable dynamic dose calculation [49]. Martin et al. showed the use of MRI visible seed spacers to ease the seed registration [50].

Robotic navigation tools have also been considered for MRI interventions to facilitate and speed up the needle placement for biopsy and therapeutic methods like BT [51–53]. One is the CE certified MR-compatible Remote Control Manipulator (RCM) (Soteria medical, Arnhem, the Netherlands) designed for transrectal in-bore biopsies [54, 55] leaving the needle implantation in the hand of the physician. It is a Level II robot as well. In contrast to the state of the art, the fixed template is replaced by the transrectal needle-guide, a water fillable injection template enabling MR-image guidance during the implantation. The needle guide is automatically rotated with pneumatic actuators around a fixed point such that the implantation trajectory points to the desired target. Together with the ability to move the needle guide forward and backward, the RCM counts three degrees of freedom. In this thesis, the RCM is considered for prostate seed-BT in an MR-only workflow.

Research objectives The main objective of this thesis is to pave the way to a new robotic seed-BT. This includes the development of a new intervention workflow as well as a novel TPS to fully benefit from the possibilities of the two robotic systems guidoo and RCM.

The TPS should contain a needle-path planning according to the degrees of freedom of the given robot and an inverse dose optimization. The guidoo has seven degrees of freedom which allows nearly arbitrary needle paths enabling to reach target volumes partly covered by complex risk structures [56]. Therefore the path planning should consider all directions around the PTV as possible needle trajectories. Siauw et al. introduced a needle candidate domain for skew catheter trajectories in a defined plane for prostate HDR-BT [57]. In this thesis, the concept of generating a needle candidate domain with all possible needle trajectories, which circumvent risk structures was inspired by this paper. The needle candidate domain would then serve as a basis for the inverse treatment planning. Scenario 1 refers to a liver metastasis to be treated with the assistance of the guidoo.

For transrectal needle implantations with the RCM the needle guide is constrained by the rectal wall. Possible displacements to the needle guide due to outer pressure of the

scenario	robot	implantation technique	target volume	D_{pr} (Gy)
1	Guidoo	transpercutaneous, multiple directions	liver metastasis	100
2	RCM	transrectal, fan shaped	prostate	115, 145
3	RCM	transrectal, fan shaped	intraprostatic lesion	160

Table 1: Describes the three scenarios and its unique features such as the used robot, the target volume location and the prescription dose D_{pr}. Details to the prescription schemes can be found in section 2.1.2

rectal wall by limited space or patient movement complicate a workflow centred on an intra-operative pre-plan. Therefore, a TPS with a highly adaptive implantation workflow is necessary. Scenario 2 refers to planning of the prostate CTV as it is established in the state of the art approach. Furthermore, scenario 3 focuses on intraprostatic ultra-focal target volumes (F-CTVs) in the prostate. In contrast to the guidoo, here all needle paths meet in the rotation isocentre (in the following termed as rotation point) of the transrectal needle guide. The rotation point is a freely chosen coordinate point on the registered needle guide trajectory. It should be chosen such in a way that the expected needle trajectories can be realised without reaching the movement limit of the RCM because of the limiting rectal wall.

Simulated implantations SIs for each scenario are used to study the impact of seed displacement to the given dose constraints for two assumed NPAs. One NPA represents the accuracy of the state of the art approach and the other a higher accuracy that might be achievable by using a robotic assistant. Moreover, the potential benefit of online needle adaption in the SI is to be analysed. Two alternative optimization algorithms are designed to automatically adapt the radiation treatment plan after each implanted needle to compensate possible seed displacements.

To test the feasibility of the transrectal intervention workflow an implantation experiment of scenario 3 is conducted using a recently published complex anthropomorphic pelvis phantom that contains prostate lesions [58]. MRI image guidance is used to register the needle guide alignment and thus to recalculate the needle trajectory. The feedback to the TPS enables to approve or realign the needle guide. Delivered seeds are registered with MRI using commercially available spacers (Sirius, C4 Imaging LLC, Texas, USA) [50]. The accuracy of each workflow step including needle guide and seed registration with MRI is determined.

Remarks to related contributions This thesis is associated to two master theses that contributed to the TPS [59, 60]. The TPS is based on a MATLAB (The MathWorks-R2020a) project of the preliminary master thesis [59]. The latter contains the object-oriented structure as the classes of intervention objects such as the target space, needle and seed, the input file specifying the treatment setup and the kinematic scripts to rotate and translate seeds within the target space.

The TPS validated on the example of a liver metastasis for external needle injections

described as scenario 1 was published my own publication [61]. The ideas and implementation of the TPS with the dose modelling, path planning, needle candidate domain and optimization algorithms are attributed to me as the first author. The co-authors contributed in proof reading, as well as discussions and retreats during the implementation phase.

The simulated annealing adaption algorithm in the context of scenario 1 was published in the poster session [62]. The co-authors contributed in comments to the abstract and poster.

For transrectal prostate-BT the TPS was then preliminary modified in the supervised master thesis project of [60]. Methods used from the latter are the introduction of margins to the TPS, the contouring and structure set generation of the five lesions and various urethra margins considered in scenario 3, the preliminary transfer of the candidate needle domain concept and the simulated annealing optimizer. However, I then rewrote the candidate needle domain generation and simulated annealing optimizer to match my purposes described in sections 2.4 and 2.5.5.

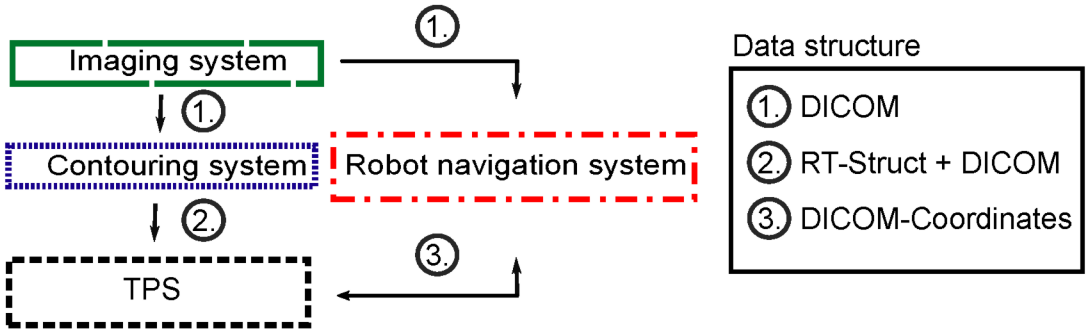

Figure 1: Data-flow during the intervention. The three data types are the Digital Imaging and Communications in Medicine (DICOM) format, the RT-Struct containing the contour information and coordinates of the world DICOM coordinate system.

2 Materials and methods

2.1 Setup for robotic brachytherapy

2.1.1 Robotic workflow

Within the scope of this work there are three robotic intervention scenarios that consist of a diagnostic imaging system, contouring system, TPS, and the robot navigation system.

Figure 1 on page 9 displays the data-flow between these systems. The world DICOM coordinate system of the imaging system is used for the treatment planning system. The robot's internal coordinate system is matched with the latter by scanning and registering the needle injection template with the imaging system.

The organs at risk as well as the target volume can be delineated with the contouring system. For this task the commercial treatment planning system (Oncentra Prostate (OCP) v.4.0, Nucletron B.V., subsidiary of Elekta AB, The Netherlands) is used. The structures are then exported as an RT-Struct file to the TPS presented in this thesis.

The TPS software is used to model the robotic intervention with needle path planning, dose optimization and to display these with the patient image data. The basic ideas of an object oriented seed-BT TPS with seed and needle classes can be found in [44]. The dose modelling, needle path planning as well as the optimization algorithms were developed during this thesis and are discussed in the following sections.

All calculations were conducted using an Intel® Core™ i5-6500 CPU with 3.2 Ghz, 16.0 GB RAM and a NVIDIA NVS 510 graphics card on Windows 10.

Scenario 1 In this section the workflow for percutaneous needle injections (scenario 1, Table 1 on page 7) is discussed. As a treatment example a complex, novel abdom-

inal phantom with a liver metastasis (40.3 ml) has been scanned with an Artis Zeego (Siemens, Erlangen, Germany), a robotic Cone-Beam Computed Tomography system designed for angiography.

a)

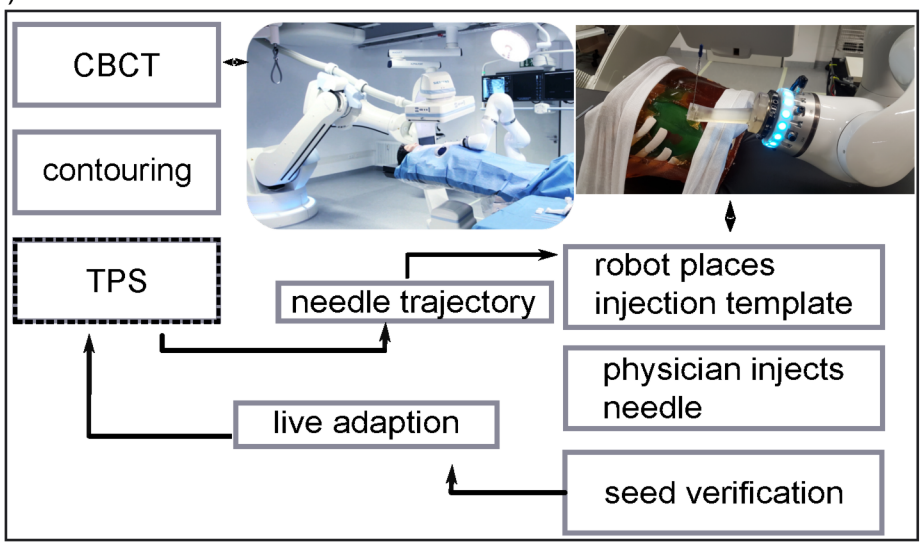

b)

Initialisation	Import contours and reconstruct 3 dimensional volumes
Path planning	Locate injection coordinates
Needle candidate domain	Combine injection with tip coordinates
Greedy optimizer	Generate initial plan with V100>99%
Remove seeds	Reduce the V200 in overdosed regions
Variate needle injection depth	Improve the seed distribution in the target
Coverage optimizer	Set final needles until V100'>V100+1%

Figure 2: a): The experimental setup and schematic workflow of scenario 1. a) left picture: The CBCT system Artis Zeego and the navigation assistance system guidoo. Right picture: The abdominal phantom and the injected needle with the positioned injection template. b): Short description of the TPS work steps. Adapted from own publication [61]

The workflow is visualised in Figure 2 and starts with a Cone-Beam Computed Tomography of the abdomen. The image data is contoured including the target volume,

bones and OARs. The RT-Struct is then transferred to the TPS with the scripts of [63]. Then 3D alpha shapes are generated with the MATLAB alphashape function which is based on Delaunay triangulation of the contour coordinates [64, 65].

Figure 3 on page 12 displays the initialised volumes that are the metastasis as target volume and the liver, aorta, vena cava and ribs as OARs.

The needle path planning (section 2.3) algorithm identifies all injection coordinates able to reach the target volume by circumventing risk structures. Then the needle candidate domain is generated which contains all combinations of the needle injection- and tip coordinates (section 2.4). Its structure contains pre-processed information used for the initial inverse optimization step (section 2.5.1). The treatment plan is then further optimized by three optimization functions (sections 2.5.2-2.5.4) to reach the given dose constraints by considering all degrees of freedom.

The robotic navigation systems receives subsequently each needle trajectory defined by the needle's tip and injection coordinate. It then aligns the injection template precisely on the patient surface internally calculating the injection angle from the given needle trajectory. The physician injects the needle verifying its position with fluoroscopy and releases the seeds. The implanted seeds' coordinates are registered with fluoroscopy to enable the live adaptation of the treatment plan in the TPS. This procedure and the adaptation optimizer has been studied with simulated implantations and is discussed in section 2.6.

Scenario 2-3 Scenario 2 and 3 (Table 1 on page 7) distinguish each other by the target volume and planning objectives. The workflow uses the RCM and is the same for both scenarios.

In these scenarios a robotic intervention to the prostate is investigated with MRI as imaging system. The robotic system is the RCM used to guide transrectal needle injections. Figure 4 on page 13 shows the pelvis phantom used for the image data set generation and experiments with the RCM.

The proposed workflow (Figure 5 on page 14) starts with T2 weighted images in transversal and sagittal slices. The acquisition angle is arranged (approx. 45°) such that the needle guide is cut along its trajectory to enable visualising the stitch canal in the central slice (compare Figure 4 on page 13. The images are sent to the RCM software to check the alignment to the patient to the RCM and to choose the rotation point that is used in the TPS later on. With a fixed rotation point the needle path planning is simplified in these scenarios. They are further imported in OCP to contour the prostate, F-CTVs, needle guide and OARs such as the urethra, bladder and rectum and imported as RT-Struct into the TPS to generate the needle candidate domain (section 2.4) and for inverse radiation treatment planning (section 2.5).

After preparing the needles with seeds the intervention starts and the first needles' tip coordinate is identified in the RCM navigation software. The needle guide can be registered semi automatically by double clicking on the needle guide easily visible due to the fillable water depot around the stitch canal. The needle guide is then prompted to navigate to the desired location. In the box of Figure 5 this is described in point 1.

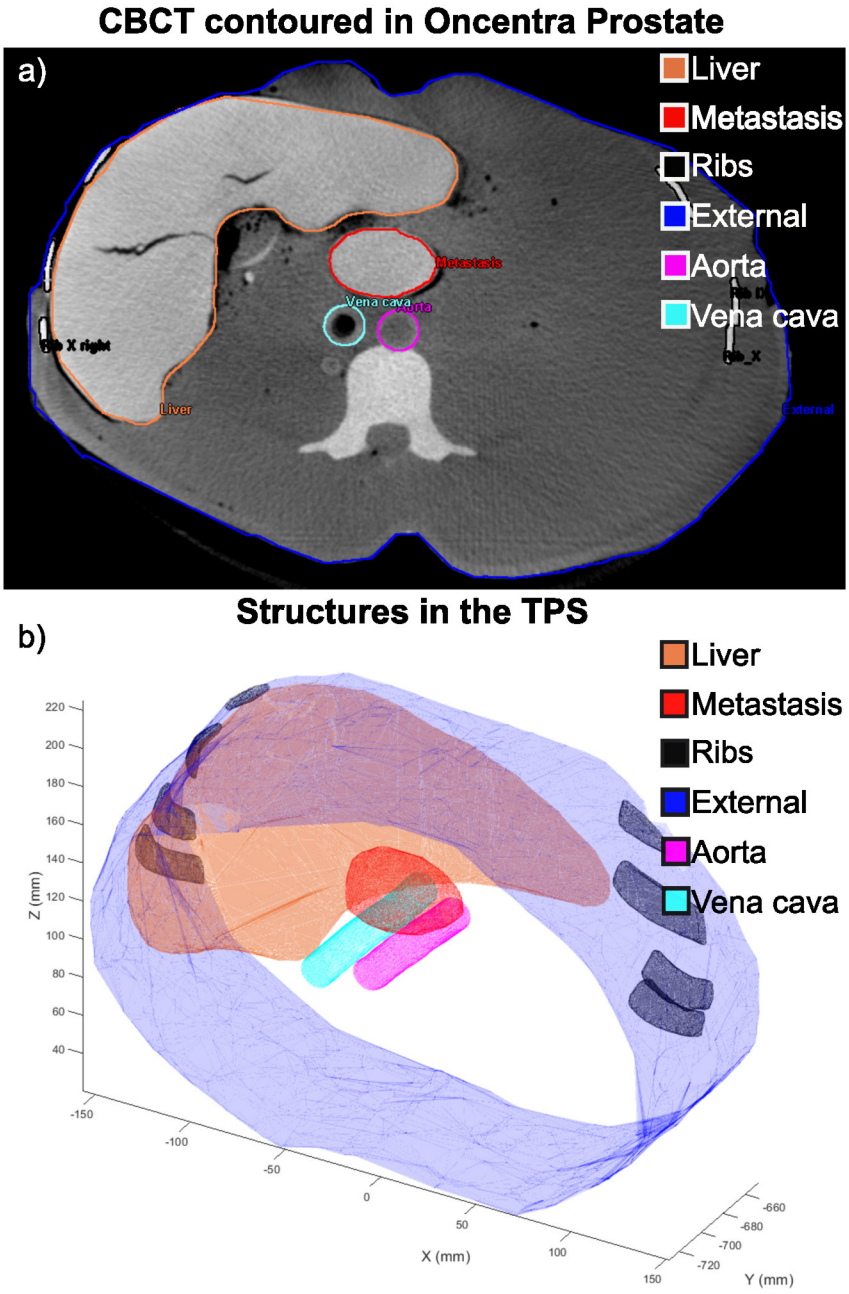

Figure 3: a) A contoured CBCT image of the abdominal phantom in OCP.b) The imported contours of scenario 1 as alpha shapes in the TPS. Adapted from own publication [61]

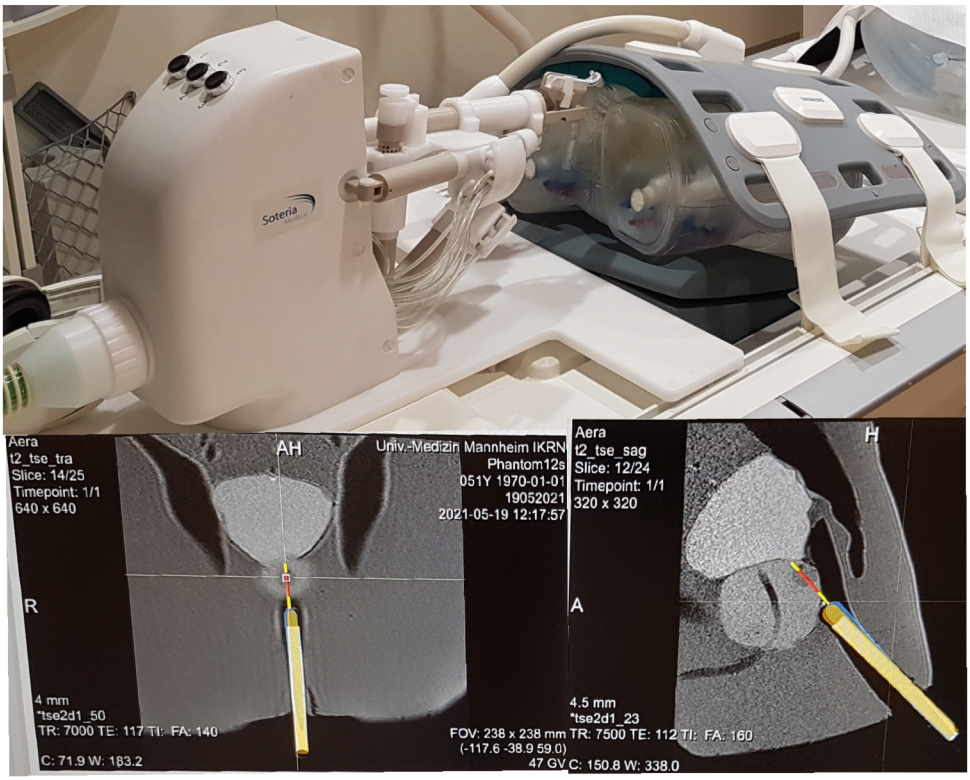

Figure 4: Up: The implantation setup showing the RCM with the docked needle guide and the phantom in prone position under the body coil on the MRI table. Down: Transversal and sagittal MRI images of the phantom with the registered needle guide (yellow) and the planned needle guide position (blue).

The latter is verified by MRI scans. The needle guide position is used to recalculate the needle trajectory with the use of the needle guide tip- and rotation point coordinate to adapt the insertion depth if necessary and approve the live needle trajectory (point 2 in Figure 5). The physician injects the first needle and releases the seeds, which are subsequently verified with another MRI scan. The feedback of the implanted seeds' coordinates located in the MRI images (point 3 in Figure 5) enables adapting the remaining needle trajectories (section 2.6) with the simulated annealing adaption (SAA) algorithm. The latter was benchmarked by simulating the needle injections with a given NPA and comparing the adapted simulations with the unadapted ones.

The whole workflow's feasibility was tested in a phantom experiment measuring the accuracy of each workflow step (section 2.7). A detailed description of this workflow in context of the experiment can be found there as well.

2.1.2 Planning objectives

Scenario 1 The liver metastasis is treated in this scenario with $D_{pr} = 100\,Gy$ prescribed as the enclosing isodose-shape. Therefore the percentage of the target volume

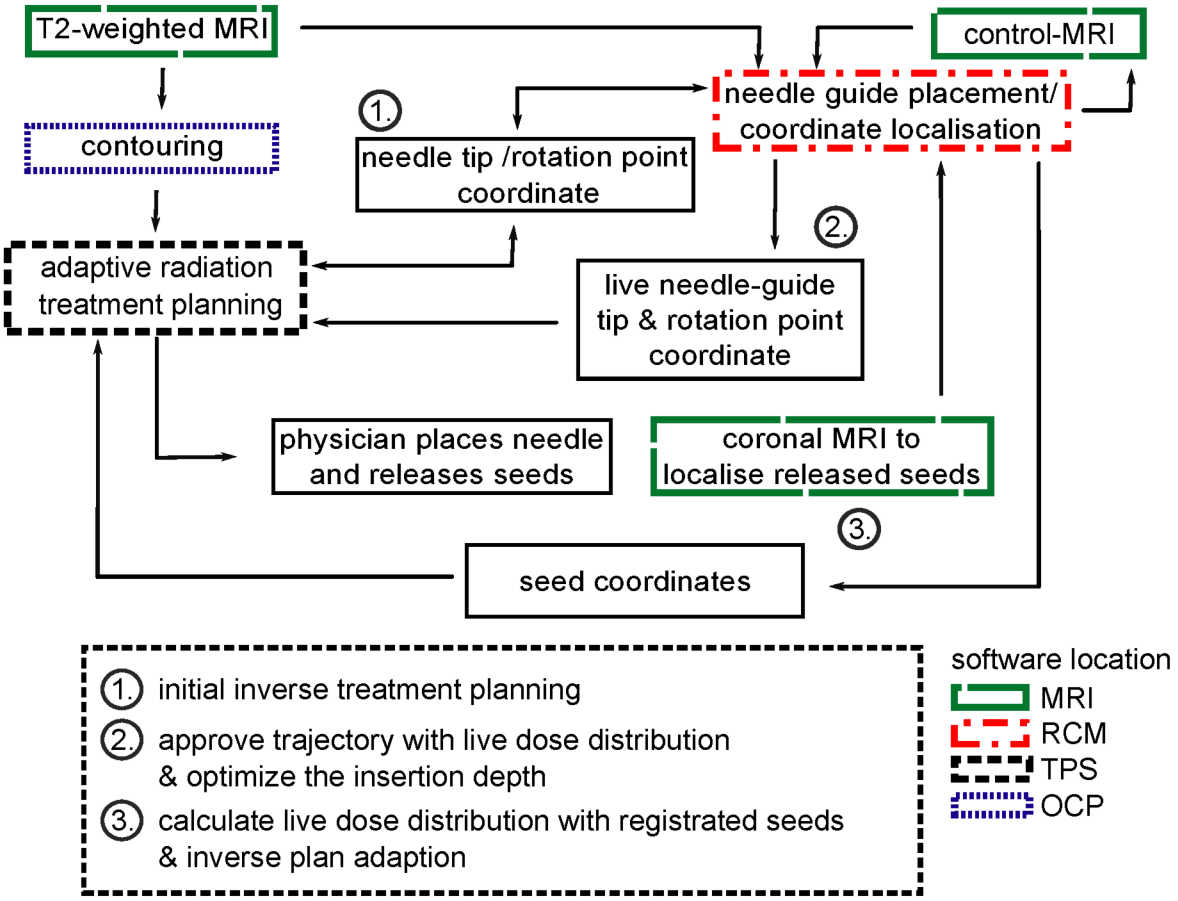

Figure 5: The workflow chart starting in the upper left corner just after the setup preparation. Three interactions 1-3 between the TPS and the RCM software are closer described in the box below. The first interaction is required to start the treatment planning. The second interaction is required after each automatic needle guide alignment by the RCM to control it. Then the needle implantation takes place. The third interaction is the seed coordinate feedback to enable control over the implantation and adaption strategies.

receiving the prescription dose (V100) should be close to 100 %. In the seeds' vicinity the irradiance is much stronger than further off which leads to a highly inhomogeneous dose distribution with high dose areas in the target volume receiving more than 150 % or 200 % (V150 and V200) of the prescription dose. However, the prescription dose is chosen considering organs at risk in close contact, which here are the aorta and vena cava. For these OARs, clinical constraints and effects for violations for seed doses are unknown. However, the maximum dose to 1 % of the OAR (D1) should be less than 100 Gy. On the other, a dose escalation to a metastasis with no organ at risk should also

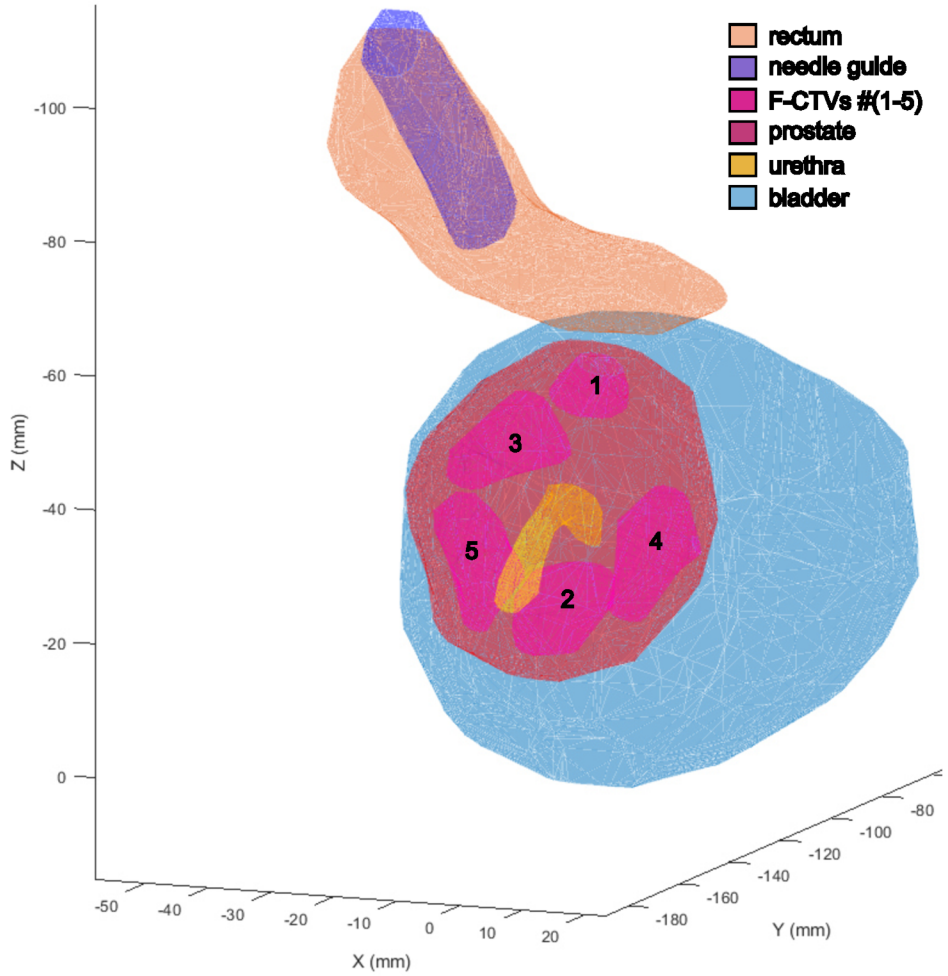

Figure 6: The alpha shapes of the contoured phantom in prone position with five F-CTVs as target volumes in the TPS for scenario 3.

be constrained to the point where no further tumour control is observable to maintain the number of used seeds at a feasible amount. Martinez-Monge et al. e.g. prescribed 160 Gy (equivalent to 144 Gy with TG-43) to liver metastases treated with seeds [8]. The planning constraints were defined as V100 $\leq$ 97 %, D90 $>$ 120 % of D_{pr} and a V200 as low as possible. The D90 is the minimum dose received by 90 % of the target volume. For the needle path planning algorithm the liver and the ribs were to be considered as risk structures that were not allowed being punctured.

Scenario 2-3 In scenario 2 (Table 1), the prostate is delineated as the target volume (CTV with V = 49.4 ml) with prescription doses of $D_{pr,1}$ = 145 Gy and $D_{pr,2}$ = 115 Gy. These are the state of the art prostate seed-BT dose concepts for the monotherapy and the combined therapy with additional 40 Gy of EBRT. To spare the urethra an urethra margin of 8 mm is generated in OCP to prevent seed locations in close distance to the

urethra. The planning objectives refer to the AAPM TG-137 report [66]. The prostate constraints are V100 > 95 %, V150 < 50 % and V200 < 20 % of the prescription dose and D90 > D_{pr}. The V100 and the D90 attribute the dose coverage of the CTV and the V150 and V200 constrain high dose volumes inside of the CTV to 50 % and 20 % respectively. The dose constraint D90 > D_{pr} could be related directly to the clinical outcome in [67]. Alongside, the four year freedom from biochemical failure rate was shown to be 92 % for a D90 > 140 Gy [68]. Organs at risk are the urethra and rectal wall, which are to be spared by too high doses related to side effects such as urinary symptoms and rectal bleeding [69]. The urethra constraints are primary the D10 < 1.5 D_{pr} and secondary D30 < 1.3 D_{pr}. The rectum constraints are primary $D_{2\,cc} < D_{pr}$ and secondary $D_{0.1\,cc} < 1.5\ D_{pr}$. Here $D_{2\,cc}$ signifies the maximum dose to 2 cm^3 and $D_{0.1\,cc}$ to 0.1 cm^3 of the rectum.

In scenario 3 (Table 1 on page 7), the target volumes are intraprostatic lesions. The contoured volumes are displayed in Figure 6 on page 15. Five F-CTVs were delineated as target volumes (lesions L1 (V = 0.6 mL), L2 (V = 1.8 mL), L3 (V = 1.3 mL), L4 (V = 1.5 mL) and L5 (V = 1.7 mL)). The prescription dose for the covering isodose was set to D_{pr} = 160 Gy for lesions L1/3/4/5 and to D_{pr} = 115 Gy for L2 due to its hardly reachable location behind the urethra. The case of L2 shows the limitations of the system due to the given geometry and is discussed in the limitations part (section 4.7).

The aim for the ultra-focal approach is a high V100 close to 100 % and an optimal sparing of the organ at risks with doses of urethra and rectum far below the current dose constraints described in the paragraph of scenario 2. The V150 and V200 dose constraints to the F-CTV are of minor importance in this setting having a small focal target volume, because the dose escalation inside of the F-CTV may be beneficial for a better local tumour control.

2.2 Dose modelling of Iodine-125 seeds

Iodine-125 seeds are radioactive sources emitting weighted mean E_γ = 28.37 keV photon radiation with a steep dose gradient [70]. The latter enables to reach a high dose in the target volume and low doses outside in the normal tissue and OARs [16]. Figure 7 on page 17 displays the seed structure and the seed strands with seeds and spacers.

Iodine-125 is adsorbed as silver iodide to the metal marker surface. The latter is used for a positive CT-image contrast to register implanted seeds after implantation. The seeds are sealed inside a titanium hull to avoid contamination during application.

In this thesis the use of seed strands is preferred to prevent seed migration and increase the stability of the seeds on the strand by limiting the displacement and rotation to each other [20].

The TG-43 line source (2D) formalism with the seed source BEBIG model S17plus ^{125}I is used for the dose modelling [70, 71]. The air-kerma strength per seed is set to 0.838 U as it is used in the local radiotherapy department. The latter is the source activity, which indirectly influences the number of seeds and needles in the optimization process due to the total dose emitted by each seed.

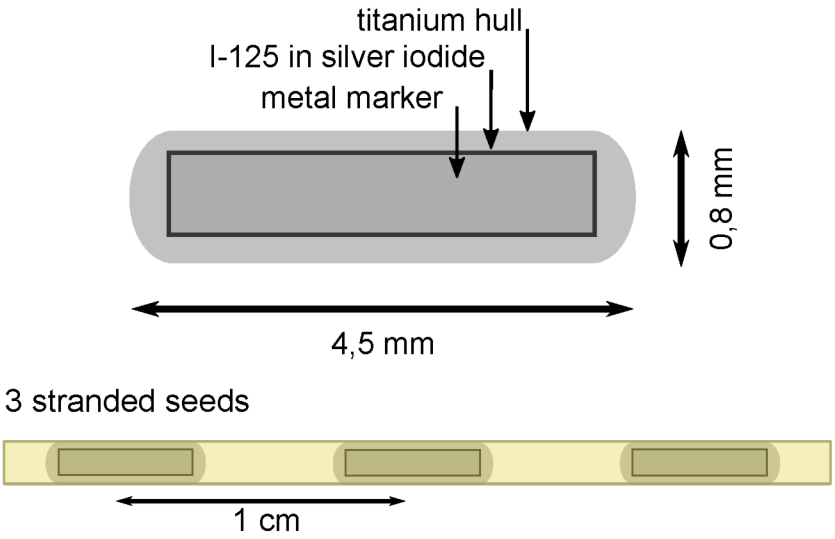

Figure 7: Up: A schematic view of an ^{125}I seed. Down: Three stranded seeds with 5.5 mm space to each other. The seed centres then are 1 cm apart from each other. Adapted from own publication [61]

In the TG-43, the AAPM recommendations report to the dosimetry of interstitial brachytherapy sources, the seed's dose rate at a point P is expressed in terms of P's spherical coordinates r and θ, where r is the distance from the seed's centre O and θ is the angle between the seed's axis and $\overrightarrow{OP}$ [72]. Because of the seed's cylindrical symmetry, the dose rate is independent of the azimuthal angle ϕ. The dose rates in water are tabulated for 2.5 mm $\leq r \leq$ 10 cm and $0 \leq \theta \leq 90°$ in [71]. The dose rates are integrated numerically over the time to obtain the absolute dose grid of one seed in water.

The seed is aligned with its 4.5 mm length along the 0° line. The dose matrix is flipped to match 360° by making use of the dose rate's symmetry to the seed centre. To have a more precise estimation of the steep dose gradient of the seed, the dose is extrapolated for each angle to the distance points $r = 1, 2$ mm and further to the seeds surface with dynamic distances to the seed centre r_{surf}. For $10° < \theta < 170°$ the corresponding surface point is in the lateral surface of the seed cylinder, whereas it is in the cylinder's base for $\theta \leq 10$ and $\theta \geq 170°$. So then θ is calculated with

$$\mathrm{r_{surf}}(\theta) = \frac{\mathrm{d_{seed}}}{2\sin(\theta)} \ (10° < \theta < 170°). \tag{1}$$

For $\theta \leq 10°$ (and $\theta \geq 170°$) the corresponding surface point is in the cylinder's base. Here r is approximated as the average of the distances of the proper surface ($r = L_{seed}/2 = 2.25$ mm for $\theta = 0°$) and the surface of the marker ($r = L_{marker}/2 = 1.85$ mm for $\theta = 0°$)

$$\text{outer} = \frac{\mathrm{L_{seed}}}{2\cos(\theta)}, \tag{2}$$

$$\text{inner} = \frac{\mathrm{L_{marker}}}{2\cos(\theta)}, \tag{3}$$

$$\mathrm{r_{surf}} = \frac{(L_{seed} + L_{marker})/2}{2\cos(\theta)}. \tag{4}$$

For the angles 0°, 2° and 5° 2.25, 2.20 and 2.1 mm for $\mathrm{r_{dist}}$ is chosen.

For each angle θ_i the dose values $D_{\theta_i}(r)$ are fitted with the power function $f(r) = a\ r^b$ along the distance r from the seed centre. Then the surface dose is

$$\mathrm{D_{\theta_i}(r_{surf})} = \mathrm{a\ r_{surf}^{b}}, \tag{5}$$

with a and b resulting from the fit. These fit functions are also used to calculate dose values at the distances $\mathrm{r} = \{3, 4, 6, 7\}$ mm. The dose modelling ranges from the seed's surface up to 10 cm radial distance from the seed's centre.

Figure 8 on page 19 shows the dose distribution in water in polar coordinates from the centre to the radius of 10 mm in the clinically relevant dose regimen below 300 Gy with a seed displayed in the centre. Along the seed axis, the dose declines faster than in the rectangular directions where the dose distribution is elliptically shaped. In 3D, the dose distribution then is spherically shaped with dented poles along the seed axis.

The resulting 2D polar dose distribution $\mathrm{D(r}, \theta)$ then has to be expanded to three dimensions. The Matlab function scatteredInterpolant is used to generate an interpolation function F with the 2D set of the parameterised $y = r\ \sin\theta$ along $\theta = 90°$ and $z = r\ \cos\theta$ along $\theta = 0°$ [73]. Note that in TG43 $\theta = 0°$ is the axis along the seed axis (z) and $\theta = 90°$ away from the axis (y). All sampling points r and ϕ are now defined in a Cartesian coordinate system. The three room directions x, y, z are then parameterised in spherical coordinates with

$$z_{3D} = r\sin(\phi)\cos\theta, \tag{6}$$

$$y_{3D} = r\sin\phi\sin\theta \tag{7}$$

and

$$x_{3D} = r\cos\phi \tag{8}$$

with $-180° \geq \phi \geq 180°$ varied in ten degree steps. Due to seed's rotational symmetry of the cylindrical seed along its long axis the dose with a specific distance to the seed centre and angle is constant independently of the ϕ angle. Therefore the 3D dose grid can be calculated by projecting each point back to the 2D grid by calculating the 3D grid by $F(\sqrt{x_{3D}^2 + z_{3D}^2}, y_{3D})$ for all sampling points of the spherical coordinates. The first argument signifies the distance of each sampling point to the seed centre which is used as value for z_{3D}.

Then the Cartesian 3D dose grid $\mathrm{D(x, y, z)}$ is calculated by interpolating between the 3D spherical dose grid and the Cartesian sample coordinates x, y, z with $-100\,\mathrm{mm} \leq$

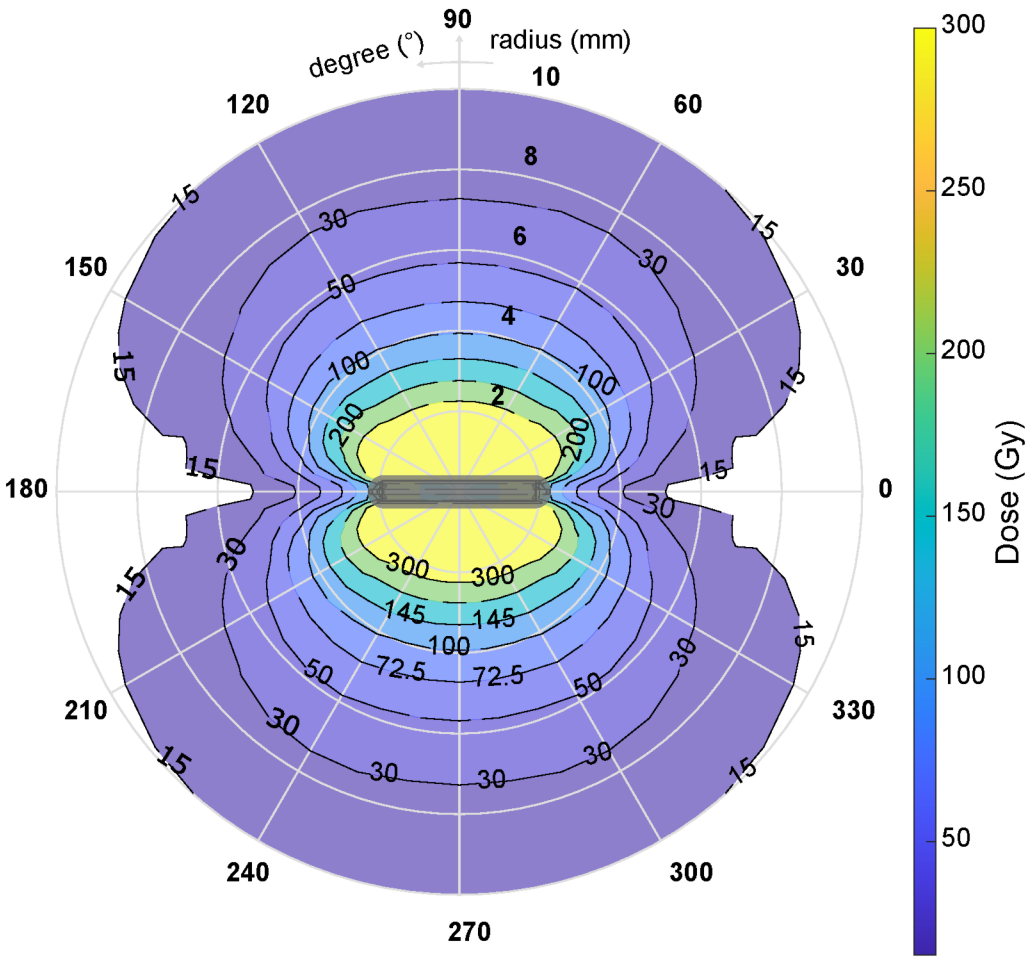

Figure 8: Shows the filled contour plot of a seed in the for the dose range of (300, 15) Gy up to r = 10 mm and $0° \leq \theta < 360°$ in polar coordinates with one seed in the centre.

$x, y, z \leq$ 100mm. The huge amount of grid points in the seed's vicinity $\{r_{surf} \leq r \leq$ 7 mm minimize the error of linear interpolation as in this area the distances to the Cartesian grid points are very small. The grid resolution then is the step width of x, y, z which is 2 mm for the plan optimization and 1 mm for the calculation model evaluation in this thesis.

Figure 9 on page 20 shows the seed's dose distribution in the x, y plane with a seed in the centre on a rectangular 1 mm grid. The rotational symmetry of the cylindrical seed can be seen.

To calculate the seed's dose with a specific location and alignment its local dose grid is translated and rotated accordingly. The grids of all seeds are interpolated to the central dose grid and super-positioned in the target space to calculate the dose of the

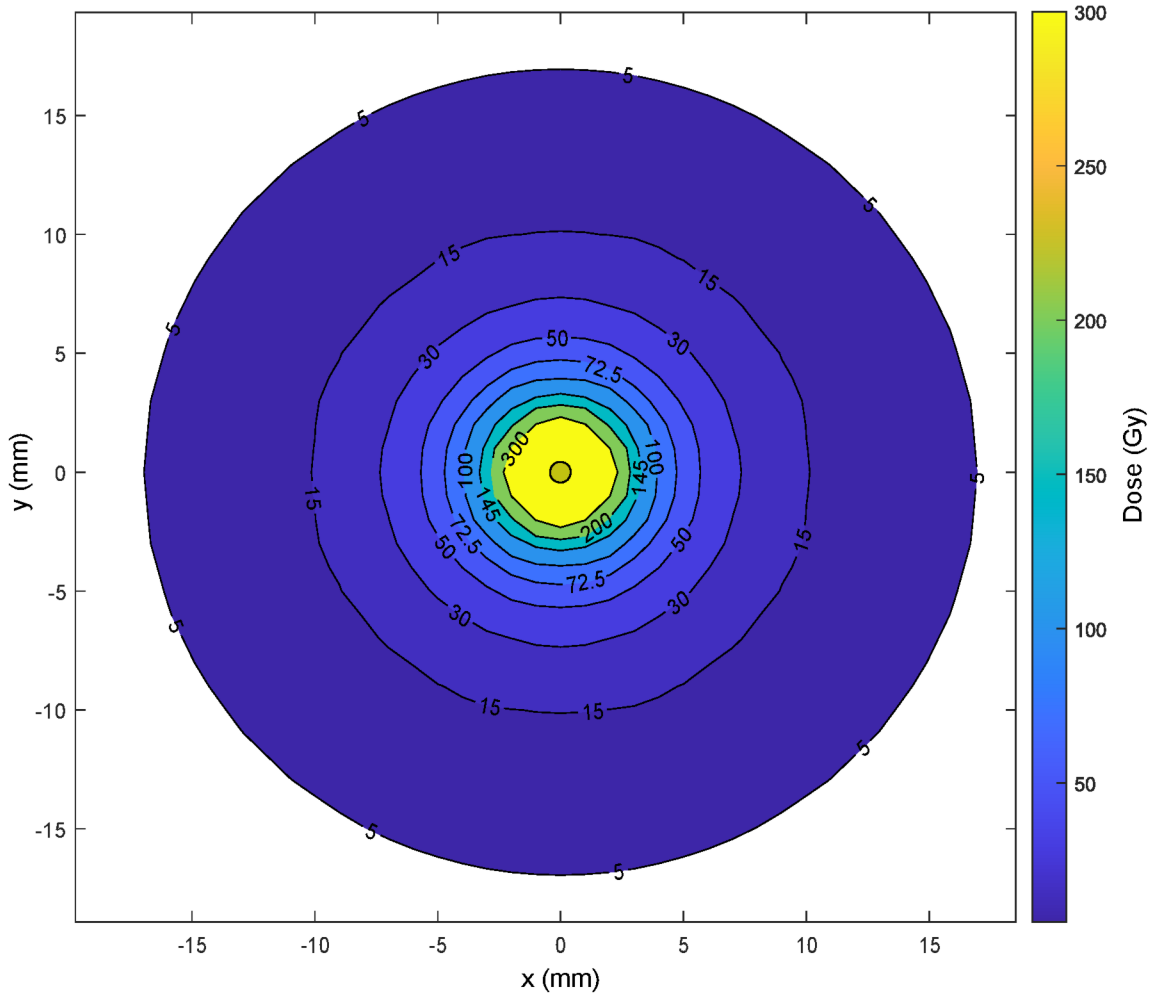

Figure 9: Shows the colour washed contour plot of a seed aligned along the z-axis in the x,y plane on a 1 mm rectangular grid.

total implant.

To validate the correct dose modelling of an $(1 \times 1 \times 1)\,\mathrm{mm}^3$ dose grid the needles of one treatment plan are re-planned in OCP by placing them according to the DICOM coordinates of the image set. Two representative dose planes are compared with a global gamma analysis in the commercial software OmniPro I'mRT (IBA -1.7b). The latter is a widely used method to compare dose planes of e.g. the planned dose vs. the measured dose in EBRT quality assurance [74].

2.3 Needle path planning

Scenario 1 The needle path planning aims to identify all feasible injection coordinates on the patient skin to reach the target volume by circumventing risk structures. The

injection coordinates here are a sub-domain of the contour points defining the patient's surface. A contour point is considered as an injection point if it passes all filter functions defined by the boundary conditions such as risk structures and needle length. The filter function's execution order is from coarse to fine to minimize the computational cost by minimizing the domain of contour points to be tested.

The first filter function filters contour points of the patient side, which is facing the treatment couch. The contour points with the sagittal component (direction -z) smaller than the z-component of the median coordinate of the patient's surface contour are filtered out.

To distinguish trajectories leading through risk structures to the target from valid ones a new algorithm has been designed. The needle trajectory can be mathematically seen as line segment between the injection point and the tip point. The idea is based on the fact that only one point on the trajectory found in the risk structure is sufficient to filter the trajectory out. This checkpoint is tested with the MATLAB function inShape which determines if a specific point is located inside of a given alpha shape [75]. The simplification of testing one checkpoint instead of the trajectory is on one hand side very cost effective but on the other not complete. This is no great problem as one can iteratively test the remaining trajectories with other checkpoints. To minimize computational costs the checkpoint chosen should exclude as many invalid trajectories as possible while the subsequent filters should exclude exceptional trajectories with e.g. short path length trough the risk structure difficult to capture.

For the first OAR-filter all needle trajectories with their injection points $\mathrm{IP_i}$ point with the tip point TP on the median of the target volume. The index i defines the position in the array of injection points as well as the needle trajectory together with TP.

The needle trajectory's unit vector from tip to injection is $\frac{\overrightarrow{\lambda_i}}{|\overrightarrow{\lambda_i}|}$, with $\overrightarrow{\lambda_i} = \overrightarrow{\mathrm{IP_i} - \mathrm{TP}}$. The checkpoint ($\mathrm{CP_i}$) is then calculated with

$$\overrightarrow{\mathrm{CP_i}} = \overrightarrow{\mathrm{TP}} + \mathrm{r}\,\frac{\overrightarrow{\lambda_i}}{|\overrightarrow{\lambda_i}|}. \tag{9}$$

The distance r is defined by the length of the median of the risk structure $\mathrm{M_R}$ to the median of the target volume $\mathrm{M_{TV}}$

$$\mathrm{r} = |\overrightarrow{\mathrm{M_R} - \mathrm{M_{TV}}}|. \tag{10}$$

Then the checkpoints are located on a spherical surface with the radius r. The index i defines the location in the array and relates the checkpoint $\mathrm{CP_i}$ on the trajectory $\overrightarrow{TP}$ to its injection point $\mathrm{IP_i}$. All $\mathrm{IP_i}$ with the $\mathrm{CP_i}$ located inside of the risk structure are filtered out. In the TPS the inShape function is able to efficiently process the whole array of checkpoints as one input which results in a fast computation as MATLAB is optimized for operations involving matrices.

The next filters aim to find remaining invalid injection points. The median of the risk

structure M_R and therefore the radius r is varied by

$$M'_R(x, y, z) = M_R(x, y, z) + (\delta \, \mathrm{std}(M_R(x, y, z))), \tag{11}$$

with $\delta = [-2 : 0.1 : 2]$ and $\mathrm{std}(M_R(x, y, z))$ being the standard deviation of the risk structures' contour points to the median. The raster of $\delta \, \mathrm{std}(M_R(x, y, z))$ scans the range of two standard deviations which includes about 95 % of normally distributed data considering a possible geometric asymmetry of the risk structures around their median.

To ensure the reachability of the whole CTV the tip point TP is then set on its contour surface. In each room direction the maximum and minimum of the contour points are subsequently set as TP. The filters are executed with the radius r as well as with the varied radius resulting of $M'_R(x, y, z)$ with $\delta = [-2 : 0.1 : 2]$.

The 18 gauge needles used in the local radiotherapy department have a length of 22.5 cm and a maximal insertion depth of around 20 cm. Here the maximum path length from injection point to tip point was set to 17.5 cm. The filter is used for the trajectories that point to the lowest contour point in the -z direction.

The number of injection points is further decreased by filtering out neighbouring injection points with a closer distance than 2 mm. The impact on the final treatment planning of this filter is low because needle trajectories with this small injection point distance would contribute almost identically to the treatment plan given the very small angle between the two directories pointing on the same tip point coordinate. Hence, by omitting these needle candidates the optimization process is facilitated in its decision process and converges faster to a solution.

The remaining injection points are used to generate the domain of needle candidates used for the inverse treatment plan optimization. When a needle candidate is chosen for the treatment plan, its trajectory is another time tested for collisions with risk structures. The checkpoints are equally sampled with 1 cm distance along the trajectory. However, in the case of blood vessels or smaller risk structures one would need to reduce the stepping width to ensure a safe implant. Due to the huge amount of needle candidates, computational cost is minimized here by conducting this last task only for the trajectories chosen for the treatment plan.

Scenario 2-3 In the case of transrectal needle injections the injection point is given by the rotation point of the RCM needle guide.

2.4 Needle candidate domain

Scenario 1 The contour points cp of the target volume TV must fulfil the equation

$$\mathrm{cp}(z) < \mathrm{median}(\mathrm{TV}(z)) + 1.5 \, \mathrm{std}(\mathrm{TV}(z)) \tag{12}$$

to be considered as possible tip points $\mathrm{TP_j}$ for the needle candidates. The index j defines the location in the array of needle tips. The tip points with a distance below 1 mm to

needle tip coordinate (x, y, z)	domain of injection coordinates (x, y, z) for a needle with n seeds				
	n=1	n=2	n=3	n=4	n=5
1st needle tip(x, y, z)	{injection coordinates (x, y, z)}	...			
⋮	...				

Table 2: The needle candidate domain is structured in a cell array in the TPS as displayed here. Each row contains in the first column the needle candidate's needle tip coordinate. The domain of all possible injection points pointing to this needle tip containing n seeds is stored in the $(n+1)^{th}$ column. After own publication [61]

each other are filtered out to shrink the domain size and accelerate the optimization process. Table 2 shows the structure of the needle candidate domain.

For each needle tip there is a domain of injection coordinates defining all needle candidates pointing to this needle tip. The number of the column defines the number of seeds that these needle candidates contain. In this scenario, the seeds must be placed inside of the target volume. The nth seed coordinate s_n of the $(j, i)^{th}$ needle can be calculated via

$$s_n = TP_j + (((n-1)\, L_{spacer}) + L_{tip} + L_{seed}/2)\, \frac{\overrightarrow{\lambda_i}}{|\overrightarrow{\lambda_i}|}, \tag{13}$$

with L_{spacer} and L_{seed} being the length of the seed and spacer as displayed in Figure 7 on page 17 and L_{tip} the length of the needle tip.

For each trajectory, the seed coordinates are tested if they are located inside of the target volume. The domain of valid injection points pointing to a specific tip point with the fourth seed tested would then be saved in the column five of the specific row. To prevent saving a needle candidate with a valid fourth seed but invalid seeds beforehand the injection point domain is filtered in the order from the first seed to the last. The maximum number of seeds per needle is set to $n_{max} = 5$. However, this value is defined by the target volume size and should be adapted if necessary. The candidate needle domain is used for the greedy optimizer in section 2.5.1 as a structured domain for needle candidates by navigating through it with loops over the rows j and columns i.

Scenario 2-3 In the transrectal treatment approach the needle candidate domain structure remains the same. The only injection point here is the needle guide's rotation point to be chosen in the RCM's navigation software. The rotation point coordinate remains constant to some degree during the whole intervention and therefore all needle trajectories are planned to overlap in this point.

In scenario 2, the tip point coordinates are defined initially as the prostate CTVs' contour point coordinates. To better cover the prostate they are shifted about 1.5 mm along their trajectory from the rotation point. Then the first seed coordinates are closer to the prostate contour, which facilitates to cover this part with the prescription dose.

Furthermore, the contour points of the urethra margin are chosen as additional tip points to enable covering the space between the urethra margin and the needle guide with needles. If a trajectory punctures the urethra or if its first seed coordinate is not in shape of the CTV it is removed. Then the number of possible stranded seeds for each needle trajectory is calculated. In contrast to scenario 1, the n^{th} seed-position for all tip points can be calculated by the modified equation 13

$$\{s_n\} = \{TP\} + (((n-1)\, L_{spacer}) + L_{tip} + L_{seed}/2) \left\{ \frac{\overrightarrow{\lambda_i}}{\overrightarrow{|\lambda_i|}} \right\} \tag{14}$$

by inserting the array of all tip points $\{TP\}$ and the array $\{\lambda_i\}$ which point from each tip point to the only rotation point. The seeds have to be located inside of the prostate CTV and outside of the urethra margin to be stored in the needle candidate domain. Therefore, needle trajectories may pass the urethra margin but no seed position inside the urethra margin is allowed. This enables short-stranded seeds in the anterior fibromuscular stroma, which is the space partly concealed behind the urethra.

In scenario 3, the tip points are the contour points of the F-CTV. The seed coordinate is valid if it lies inShape of the F-CTV. The first allowed seed position is defined as the tip point coordinate on the F-CTVs contour. The next seed positions are located on the needle trajectory with the inter-seed distance to each other. Therefore, the whole pathway distance through the F-CTV is used to calculate the allowed number of seeds for each needle trajectory.

2.5 Treatment plan optimization algorithms

In this section, plan optimization algorithms are described. The aim of these algorithms is to automate the planning process by formulating planning objectives described in section 2.1.2. In contrast to manual forward planning, this automated plan generation is termed inverse planning. Next to the directly defined planning objectives, another boundary condition to the optimization is the number of needles and stranded seeds. Reducing the number of needles and achieving the primary planning objective is a contradictory task that has to be balanced properly. Using short strands or single seeds increases the number of required needles to achieve the planning objectives. Single seeds would enable optimal dose distributions while achieving the primary planning objectives due to the highest degrees of freedom of placement. For the treatment outcome however, seed displacement and migration has to be considered since the seed radiation dose is delivered slowly with the half-life of 59.4 days. Therefore, a reduced number of needles by using long seed strands where reasonably usable is to be preferred, since one expects the seed displacement and migration to be smaller due to the greater volume and mass of the strand, which results in a greater stability to outer perturbation. A reduced number of needles as well reduces the implantation time and the harm to the patient by needle punctures and anaesthesia.

For scenario 1, the greedy optimizer (section 2.5.1), remove seeds algorithm (section 2.5.2), the needle-depth optimizer (section 2.5.3) and the coverage optimizer (section

2.5.4) were used (see also Figure 2 on page 10). For scenario 2, an adapted version of the greedy algorithm was used. For scenario 3, the greedy optimizer was used for an initial solution and a simulated annealing optimizer (section 2.5.5) for the optimization.

2.5.1 Greedy optimizer

Scenario 1 The greedy optimizer is designed to generate an initial treatment plan covering the target volume with the prescription dose V100 > 99%. The latter is structured in an array specifying each needle by the number of seeds and the tip- and injection point coordinates.

The optimizer adds each needle sequentially and irreversible to the target space gradually raising the dose to the required dose distribution in the target volume. Therefore the inverse optimization problem leading to a high V100 is divided into sub-problems solved by maximizing the objective function. This approach is well known as a greedy heuristic, which has been shown for prostate seed-BT as well in [76]. However, subdividing the problem may only lead to a local optimum while the global optimum of this optimization problem remains unknown. Solving the objective function of the subproblem therefore has to be related directly to fulfilling the planning constraint of the main problem which is V100 > 99%. In this procedure the dose contributions of the remaining needles is unknown. Hence, the sub-problem for each needle dynamically changes due to the dose contributions of the needles set beforehand. However, finding the global optimum is not necessarily required in this scenario as there might be a large number of needle combinations fulfilling the treatment constraint. To benchmark the statistical variations and the stability of the optimization results ten plans are generated and compared.

The first needle is the starting point of the optimization. The needle is chosen as one of the needle candidates with the maximum number of seeds $n_{max} = 5$. Its needle tip is best reachable as the one that contains the biggest array of injection points in the needle candidate domain. The injection point of the needle is then chosen as the geometrical median of the injection point array. This ensures that the first needle trajectory is aligned centrally assuming a high number of possible needle candidates with five seeds in the neighbouring space to be placed next. The first needle is set into the target space and the dose distribution is calculated on the target space's dose grid. The next needles are placed in an algorithm which is executed in a while loop stopping when the threshold V100 > 99 % is reached or no needle candidate is left due to the setting restrictions or the maximum needles number per plan of 30 needles. To decrease the number of objective function calls and saving computational cost the needle candidate domain is filtered to generate a sub-domain of considered needle candidates. Their tip points have to be located in the dose range DR of

$$\mathrm{DR} = [0.25\ \mathrm{D_{pr}}, 0.7\ \mathrm{D_{pr}} + 3\ \mathrm{N}]. \tag{15}$$

$\mathrm{D_{pr}}$ is the prescription dose and N the actual number of needles. The dynamic 3 N value takes into account that the sub-problem of the greedy optimizer changes for each needle

due to a modified dose distribution as well. The upper dose range limit is softened with each needle allowing to set needles closer to each other in the late optimization phase. The set of dose grid points fulfilling the DR condition enables generating an alpha shape to filter the domain of tip points with the inShape function. The first loop iterates the found tip points and the second nested loop the associated injection points. The latter are filtered another time by validating that each of the n seed coordinates are located inside of the DR as well. Then the objective function is called subsequently for the needle candidates defined by the remaining injection points. From this sub-domain, the needle maximizing the primary objective function output is chosen for the treatment plan. However, if the sub-domain is empty, because all needle candidates have been filtered out, the outer loop moves on to the next needle tip.

The objective function's inputs are the former dose distribution of the previous added needles and the needle candidate to be tested. It then copies the static target space, which is the super-class of the actual target space containing all constant parameters such as the generated volumes, adds the needle and computes the actual dose. The primary output is the volume size of the generated alpha shape that contains all dose grid points greater or equal the prescription dose (isoshape) and secondary the relative fraction of it inside of the target volume $V_{pr,TV}$ to the whole volume V_{pr}. The fraction $\frac{V_{pr,TV}}{V_{pr}} = 1$ shows that all dose grid points containing the prescription dose or higher are located inside of the target volume. If the fraction is smaller than one a fraction of the latter dose grid points are located outside of the target volume. Hence, the primary output relates to the prescription dose coverage of the tumour volume and the secondary to the conformity of the prescription dose shape to the target volume shape. The needle candidate has to pass the condition

$$\frac{V_{pr,TV}}{V_{pr}} > 0.96 - \frac{3\,N}{100} \tag{16}$$

to constrain implicitly the dose to the surrounding tissue by preventing needles to be set too close to the target volume contours. This would lower the fraction $\frac{V_{pr,TV}}{V_{pr}}$. However, in the late phase of the optimization this constraint is softened with a raising needles number N by $\frac{3\,N}{100}$ as the fraction $\frac{V_{pr,TV}}{V_{pr}}$ might be reduced by each peripheral needle.

During the evaluation the needle candidate maximizing the isoshape's volume size, fulfilling the constraint of equation 16 and passing the needle collision check is saved temporarily. The latter samples the needle trajectory in checkpoints each 1 cm to be validated with the inShape function. This captures the last remaining invalid needle candidate trajectories puncturing risk structures. These are trajectories with tip points other than the six maximum and minimum testing tip points used by the needle path planner in section 2.3. After evaluating the needle candidate sub-domain the temporarily saved needle candidate is chosen for the treatment plan. The dose is actualized and the next sub-problem is initialized. If there is no injection point of all tip points left that satisfy the dose range condition (equation 15) the number of seeds is reduced by one. Then the injection points are filtered with one seed position less in equation 15 which enables new valid needle candidates. After solving this problem, the seed

number however remains reduced for the next problem. For each sub-problem, the needle candidate domain is shuffled randomly. The optimizer than generates different treatment plans as different needle candidates are validated in each sub-problem. A possible dependence of the needle candidate order in the domain thus can be avoided. The statistical variation of the treatment plans is analysed by generating ten treatment plans.

Scenario 2 To treat the prostate CTV the greedy optimizer stops if V100 $> 95\,\%$ or if the number of needles is higher than 30. The first needle chosen has the maximum number of possible needles and is the one that maximizes the objective function. The latter evaluates the volume

$$\mathrm{V} = \mathrm{V}_{\mathrm{pr,TV}} - (25\ \mathrm{V200(margin)}), \tag{17}$$

with $\mathrm{V}_{\mathrm{pr,TV}}$ being the prescription dose volume inside the target volume which is reduced by 25 times the volume of the V200 inside the urethra margin. The latter penalises needles with seed coordinates close to the urethra margin to fulfil the urethra constraints. Due to the central urethra, this needle will be placed on one lateral side. In contrast to scenario 1 the dose range for the next needle tip 15 is set to

$$[0,\ 0.1\ \mathrm{D}_{\mathrm{pr}}]. \tag{18}$$

Therefore, the next needle's tip as well as its seed positions have more distance to the first needle and are mostly located on the contra-lateral gland of the prostate. The objective function for all needles except the first is then not maximizing $\mathrm{V}_{\mathrm{pr,TV}}$, but instead only minimizing V200(margin)). Therefore, the needle candidate with the lowest V200 contribution to the urethra margin is chosen. The objective function is evaluated for all needle candidates in the domain with the needle tips and seed positions inside the given dose range. After the second needle the dose range is

$$[0.2\ \mathrm{D}_{\mathrm{pr}}, 0.7\ \mathrm{D}_{\mathrm{pr}} + 3\ \mathrm{N}] \tag{19}$$

for the rest of the needles' tip points and seed positions.

Scenario 3 For scenario 3 the greedy algorithm was slightly modified in the here described way. The algorithm adds needles sequentially to the solution space until the stopping criteria are met. The latter is V100 $> 97\%$ or V150 $> 80\%$. The first needle is set as the first in the needle candidate domain containing the maximum number of seeds. The needle candidate domain is randomly permuted to generate new plans by each optimization. The next needles' tip and all seed positions have to be located in the dose range $\mathrm{DR} = [0.1\ \mathrm{D}_{\mathrm{pr}}, 1.5\ \mathrm{D}_{\mathrm{pr}} + 3\ \mathrm{N}]$. The first needle in the needle candidate domain fulfilling this condition is chosen. If there is no needle left with the specified number of seeds, the latter is reduced by 1.

2.5.2 Remove-seeds algorithm

Needles with seeds contributing to the high dose regions inside of the target volume ($D > 2\ D_{pr}$) are located to remove single seeds. The algorithm therefore aims to minimize the V200 while trying to influence the V100 as low as possible. Therefore, the optimizer chooses the needle located centrally in the high dose region as well as centrally to the outer dose gradient. The medians of the dose grid points with $D > 2\ D_{pr}$ and $D < 0.5\ D_{pr}$ are used to calculate the mean coordinate of these two points. The needle with the seed coordinate closest to the latter is identified. For the first and last seed of this needle eight sample coordinates c_j are defined by

$$c_j = \vec{s} \pm 5\ \frac{\vec{n_i}}{|\vec{n_i}|} \pm 2\ \frac{\vec{\lambda}}{|\vec{\lambda}|}. \tag{20}$$

Here $\vec{n_i}$ is one of two orthogonal vectors to the needle trajectory, $\vec{\lambda}$ is the direction vector of the trajectory and $\vec{s}$ is the seed coordinate. They are counted to the *count* variable if they are inside of the alpha shape defined by dose grid points exceeding the 200 % prescription dose. These sample coordinates however are necessary to evaluate the space around the seed, because the seed coordinate itself is always inside the V200 due to its near field dose distribution. The sample coordinates therefore have a distance of 5.4 mm to the seed coordinate. A decision threshold then evaluates the *count* variable by

$$count \geq 8 - n + 2, \tag{21}$$

with the actual number of seeds n of the needle. For the outer seeds evaluated first, the threshold is lower than for the inner seeds. This takes into account that the outer seeds are located near the target volume contour and therefore near as well to the decreasing dose gradient. The inner seeds on the other hands are closer to the high dose region and should therefore located there with more of the sample coordinates. If the *count* variable of the first and the last seed pass the decision threshold the one with the higher *count* is removed together with its dose contribution to the dose grid. Then the next two outer seeds are analysed until no further seed fulfils the decision threshold. In the TPS removing the last seed is equivalent of reducing the first seed and retracting the needle along its trajectory by the inter-seed-distance. However, removing only inner seeds is not possible because in the current workflow stranded seed sequences only are available with the inter-seed-distance.

2.5.3 Needle-depth optimizer

The needle insertion depth is a degree of freedom addressed by this optimizer. The initial needle candidates pointed with its tips on the contour points of the target volume or were retracted by the remove seeds algorithm. However, by varying the insertion depth the source distribution and therefore the dose homogeneity might be optimized leading to a higher V100 and lower V150 and V200. The primary goal is to maximize the V100 by shifting nearby needles closer to the under-dosed areas inside of the target

volume.

The needle with its tip on the target volume contour can be pushed forward 2 mm with the first seed coordinate remaining inside of the target contour. To retract the needle the position of the last seed before leaving the target volume is calculated by generating check points along the needle trajectory until one checkpoint is outside of the target volume. Its distance from the actual last seed coordinate is sampled in 1 mm steps.

The following algorithm is executed in a while loop only ending if all needles have been adapted or the optimizer is about to choose a previously adapted needle once again. For the first needle depth adaption the needle with its tip closest to the dose grid points with $D < D_{pr}$ is searched by calculating the distance of each under-dosed grid point to each needle tip. The needle depth then is varied by $(0, 1, 2)$ mm in the forward direction and the greedy objective function is evaluated. The configuration maximizing the prescription dose volume inside of the target volume $V_{pr,TV}$ is chosen. The needles are always retracted and pushed forward in an alternating matter. Hence the even needle numbers are retracted and the uneven ones pushed forward. It is assumed that pushing forward the first needle might generate an under-dosed region backwards. Further might the high dose region centre remain near the centre of the tumour volume without being shifted in one direction. For the retracted needles, the distance of the most backward seeds to the under-dosed voxels is calculated to choose the next needle.

2.5.4 Coverage optimizer

In the case that the treatment plan's V100 has been below 99 % the coverage optimizer is executed. It raises the V100 by adding additional needles with one or two seeds to the target volume's under-dosed regions. For this purpose the needle tips closest to the under dosed voxels have to be found to generate a small amount of suitable needle candidates. They should be part of the original candidate needle domain as well to ensure implantation safety according to the path planning.

The MATLAB function nearestNeighbour is used to find the nearest target volume's contour point for each under-dosed dose grid point. These contour points are intersected with the first column tip points of the needle candidate domain generating the list of indices of these tip points to refer to the related injection points for one or two seed needle candidates. For the first needle the number of seeds is $n = 2$. The injection points then are filtered for the ones that got all seeds located in the alpha shape, which is generated by the under-dosed grid points in the tumour volume. For the remaining needle candidates the objective function is called. The latter is equivalent to the greedy objective function but outputs as well the V100 value for the evaluated needle candidate. The needle candidate raising the $V_{pr,TV}$ and passing the condition

$$\frac{V_{pr,TV}}{V_{pr}} > 0.7. \tag{22}$$

is further considered. As the needle candidates are picked from the candidate needle

domain the second time, a function proves if the needle candidate has already been placed in the treatment plan by comparing the needle injection points and tip points. If the test is passed $V_{pr,TV}$ is saved as the best current value such that the next needles have to surpass it. A needle candidate however must further pass the needle collision check and is then set as a new needle if the V100 exceeds 99 % or it is the fifth needle candidate surpassing the $V_{pr,TV}$ value of the prior needle candidates and raising the

$$V100' > V100 + \frac{n}{2} \tag{23}$$

with the number of seeds n. If there are no more needle candidates left the number of seeds is reduced to one to enable further needle trajectories to be considered.

2.5.5 Simulated annealing

For scenario 3, the initial radiation treatment plan by the greedy optimizer is further optimized by a simulated annealing optimizer using the MATLAB simulannealbnd function [77]. Simulated annealing is an established optimization technique to enable finding a global minimum to a given objective function, first adapted for inverse radiation treatment planning of prostate seed brachytherapy by Pouliot et al. in 1996 [78]. Instead of modifying the seed positions that are constraint by a given set of needle trajectories resulting from the transperineal fixed template as it is the case for state of the art prostate-BT, the needles' tip coordinates are one after another varied randomly within their given boundaries, while the other needle positions are held constant and an objective function y is evaluated.

In each iteration k of the simulannealbnd function a random new needle configuration is proposed resulting in y_{new}. If y_{knew} is smaller than the previous saved $y_{current}$ the latter is updated. If it is higher, the $y_{current}$ configuration is updated with a probability of

$$p = \frac{1}{1 + \exp(\frac{y - y_{best}}{T})}, \tag{24}$$

nevertheless. This is done to possibly escape local minima. The probability depends on the temperature T that is $T_{initial} = 30$ at the beginning and lowered at each iteration k by $T_{initial}\ 0.95^k$. During the whole process the configuration resulting in the smallest y is updated as the best solution with y_{best}. In the end, this configuration is the result of the respective optimization step. A maximum number of 20 iterations and a time limit of ten seconds are set for the optimization of every needle.

It is assumed that the optimal needle tip position is somewhere around the current needle tip position since the initial configuration results from the greedy optimizer. To avoid the algorithm varying the needle tip to an unlikely reasonable position the space in which the new configuration is searched for is limited. For this eight help points located as a cube with a side length of 6 mm around the needle tip in the centre and two additional help points along the needle trajectory 3 mm forward and 5 mm backwards are calculated. All helping points located inside of the urethra shape are removed preventing

function	weight w_i	threshold D_{thresh} (Gy)	dose percentage $X(\%)$
f_1: V100	1		
f_2: D30(urethra)	0.01	145	30
f_3: D10(urethra)	0.01	180	10
f_4: D2(rectum)	0.01	120	2
f_5: D0.1(rectum)	0.01	180	0.1
f_6: D0.5prostate	0.01	200	0.5
f_7: D0.1normal	0.001	200	0.1

Table 3: The table shows the weighting factors, thresholds and dose percentages used for each error function $f_{(1-7)}$ which are summed up to calculate the objective function to be minimized by the optimizer.

configurations with needle trajectories passing the urethra. Then the maximum and minimum values of the helping points' direction coordinates x, y and z are chosen as the lower and upper boundaries of the space considered reasonable to contain a better needle tip position.

The objective function value is designed to match the treatment aims in case of a minimum function value. A high V100 and low OAR doses lead to a small objective function value. The objective function

$$\mathrm{y} = \sum_i f_i \, w_i \tag{25}$$

is the sum of all error functions f_i and their error weights w_i. The V100Err function is given by

$$f_1 = \mathrm{V100Err} = \frac{(100 - \mathrm{V100})^2}{100}. \tag{26}$$

f_1 is zero in the case of V100 = 100 and increases quadratically with a decreasing V100 value. In contrast to the linear error function the quadratic one weights the dose deviation greater than 1 (e.g. V100 < 99) more and smaller than 1 (V100 > 99) less. The other error functions are given by

$$f_{i)} = \frac{(\mathrm{Dx_{OAR,i}} - \mathrm{D_{thresh,i}})^2}{100} \tag{27}$$

with $2 \leq i \leq 7$, $\mathrm{Dx_{OAR,i}}$ being the minimum dose value of x percent of the OARs volume and $\mathrm{D_{thresh,i}}$ a threshold value to penalise an exceeding $\mathrm{Dx_{OAR,i}}$ value. If $\mathrm{Dx_{OAR,i}} < \mathrm{D_{thresh,i}}$ the error functions is set to 0. f_1 maximizes the F-CTVs V100 and $f_{(2-7)}$ are designed to spare OARs and reduce dose inside of the prostate and the normal tissue. Table 3 shows the used weighting factors and thresholds.

The result of the simulannealbnd function is a modified needle tip coordinate that is accepted if the belonging needle passed the collision check function. The latter checks

if sample points with 1 mm spacing along the needle trajectory are located inside of the urethra. The optimization stops if the V100 = 100%, the time limit of five minutes is run out or no better solution is found after iterating through all needles the second time.

Within this optimization strategy, seeds outside of the F-CTV are possible. To remove these outer seeds with minor importance to the dose constraints the "remove outer seed function" has been designed. A loop iterates through all seeds and finds the minimum spatial distance between the seed coordinate and the contour points of the F-CTV. The seed with the highest distance and not being localised in the F-CTV shape is removed. Then the simulated annealing optimizer is run another time to correct a worsened V100 value. These two functions are conducted as long as the F-CTVs V150 > 79%, V100 > 96% and the minimum dose of 3% of the prostate volume D3(prostate) > 1.15 D_{pr}, a measure of high dose values outside of the F-CTV. This is e.g. for D_{pr} = 160 Gy D3(prostate) > 184 Gy. The latter is illustrated by Figure 10 on page 32.

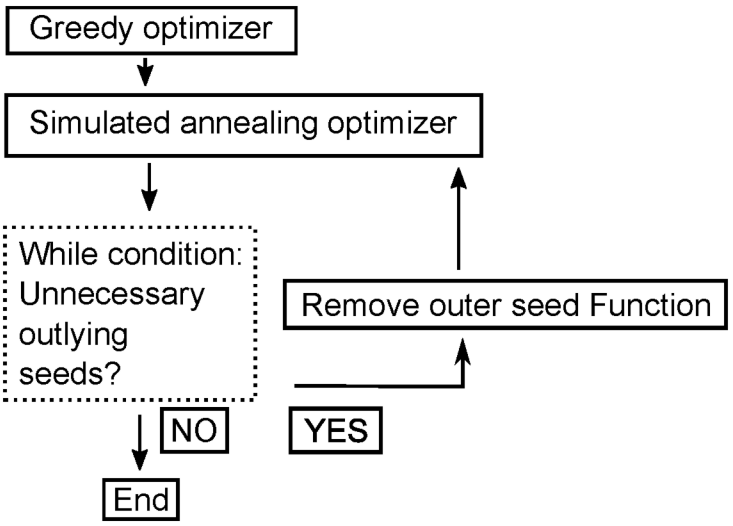

Figure 10: The inverse optimization flowchart for scenario 3 with the initial optimization with the greedy optimizer (section 2.5.1) and the final optimization (section 2.5.5).

2.6 In-vivo seed displacement adaption

The spatial registration of the implanted needles or stranded seeds with feedback to the planning system enables adapting the remaining treatment plan to correct systematic and statistical errors during the implantation procedure. This part is displayed as live adaption in the workflow of Figure 2 on page 10.

A set of simulated implantations (SI)s show the statistic robustness of a radiation treatment plan and an estimation of post treatment dose constraints that might differ from the pre-treatment ones due to needle and seed displacement. It enables exploring

online needle adaption strategies to optimize the in-vivo dose constraints and to correct seed displacement. These are enabled by in-vivo seed registration, that is detecting of implanted seeds in the diagnostic images and registering the seed coordinates on the same DICOM coordinates used for the dose calculation. The subsequent needle trajectories then are adapted. For the SIs it is assumed to know the released seed coordinates to optimize the in-vivo treatment plan.

The SI is a loop through the needle list of the inverse radiation treatment plan with each needle sequentially implanted. The online dose distribution for the loop over n needles at iteration i is calculated by

$$\mathrm{D_{online}} = \sum_{1}^{\mathrm{i}} \mathrm{D_{SI}} + \sum_{\mathrm{i+1}}^{\mathrm{n}} \mathrm{D_{PP}}, \tag{28}$$

with $\mathrm{D_{SI}}$ being the dose distribution resulting from implanted needles and $\mathrm{D_{PP}}$ from pre-planned ones.

The simulated annealing adaption (SAA) algorithm presented here is used to optimize the online dose distribution during implantation. It is assumed that the NPA depends of statistical and systematic errors depending on the patient storage relative to the system setup, the implantation technique and patient movement during the intervention. To simulate a needle implantation a normally distributed or constant deviation is added to the needle's tip coordinate. The standard deviations of the normal distribution are chosen with $\sigma = 1\,\mathrm{mm}$ and $\sigma = 3\,\mathrm{mm}$. The former relates to the NPA that a brachytherapy robot should reach at a seed placement accuracy $< 1 \pm 0.5\,\mathrm{mm}$ in a phantom experiment [27]. The latter was chosen in accordance with the NPA of a good perineal TRUS guided seed-BT, which is assumed to be $3 - 6\,\mathrm{mm}$ [27]. The constant deviation is chosen as 2 mm randomly added to each coordinate. The latter can be assumed as a result of a systematic error source.

The SAA algorithm uses simulated annealing with the same quadratic error functions as in equation 27. Additionally the error function

$$g_2 = \frac{V200_{CTV}}{100} \tag{29}$$

yielding a linear relation between the V200 and the function value g_2 is introduced. The lower the V200 the better the functional value. Further the search space is reduced to a cube with a side length of 3 mm. Hence the lower and upper bounds for each room direction are $\pm 1.5\,\mathrm{mm}$. The term SAA is in the following thesis used as the SI with the additional use of the SAA algorithm. It is compared to the SI, which presents the simulation of an unadapted implantation.

Two studies for scenario 1 and 3 are conducted and described in the following two sections. For scenario 2 however a more cost effective greedy adaption optimizer is presented.

Scenario 1 The SAA algorithm aims to achieve the same constraints as the treatment planning in order to compensate possible loss of dose coverage. Only the dose constraint to the D1(aorta) which is the maximum dose to 1 % of the aorta is constraint more restrictive. Ten SIs of one of the ten optimized plans in scenario 1 with the NPA of ±1 mm and ±3 mm are compared with the SAA. In this study, all needles except the first one are adapted by SAA. Table 4 displays the chosen optimization parameters. Figure 11 on page 34 displays plots of the weighted penalty functions. It can be seen, that g_1 has the highest and g_2 the lowest impact on the objective function strongly depending on the chosen error weight w_i. For g_3 and g_6 the error weights had to be adjusted such that they contribute in the same range to the objective function. The highest dose on 1 % of the aorta (D1(aorta)) was set to 60 Gy to spare the aorta of high dose peaks. Thereby, all plan parameters are optimized to remain near the pre-treatment values. Ten SIs of one treatment plan with needle tip deviations of ±1 mm and ±3 mm are compared with SAA.

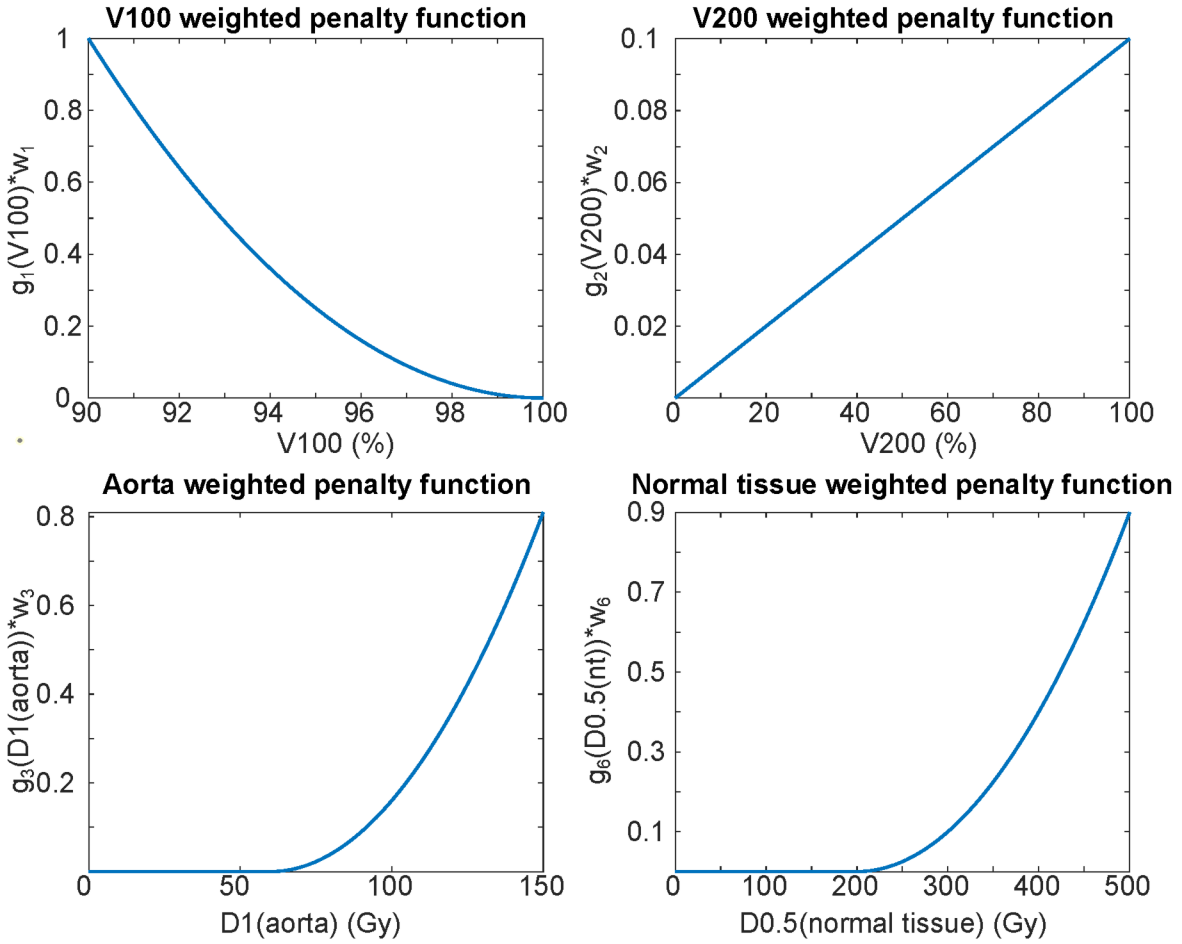

Figure 11: Plots of the weighted penalty functions g_1 w_1, g_2 w_2, g_3 w_3 and g_6 w_6.

function	weight w_i	threshold D_{thresh} (Gy)	dose percentage $X(\%)$	pre-treatment dose DX_{oar} (Gy)
g_1: V100	1			
g_2: V200	0.1			
g_3: aorta	0.01	60	1	96.98
g_4: vena cava	0.01	60	1	69.91
g_5: liver	0.01	90	1	89.82
g_6: normal tissue	0.001	200	0.5	142.15

Table 4: Parameter values used for the external needle injection approach in the objective function in equation 25.

Scenario 2 The treatment plans for the prostate CTV contain the highest number of needles and seeds in contrast to scenario 1 and 2. Due to the CTV size, the treatment constraints are less dependent on the seed displacement as for the other two scenarios. However, the constraints D10(urethra) and $D_{0.1\,\mathrm{cc}}$(rectum) can be influenced highly by one displaced nearby seed.

To efficiently adapt the next needle the greedy adaptive optimizer (GA) is presented. In contrast to the SAA here only the next needle is adapted. To calculate the former dose distribution the next needle is removed. This dose distribution can be given to the objective function sparing the cost of recalculating the dose for each seed.

The upper and lower bounds of the next needle tip are the tip coordinate $\pm 1.5\,\mathrm{mm}$. The upper and lower bounds as well as the needle tip coordinate are used to generate new possible tip points by randomly permuting the x, y and z coordinates of the tip coordinate and its bounds. In contrast to simulated annealing, the domain of needle candidates is highly reduced from an infinite continuous domain to 27 needle candidates. The latter is the result of three positions $-1.5 : 1.5 : 1.5\,\mathrm{mm}$ for each room direction x, y, z. Regardless of the loss of the V100 all needles except the first one are adapted with the GA algorithm. However, the optimizer compares the objective function value of the pre-planned needle position as well with the others such that no shift to the needle is possible as well. Reducing the number of needle candidates for the adaption saves computational cost and speeds up the optimization.

The objective function then evaluates the sum of the functions $f_1 - f_5$ equivalently to Table 3, but with the weightings of $w_{2+3} = 0.3$ to better spare the urethra. The tip coordinate minimizing the objective function is used to implant the next needle.

Scenario 3 In this approach, the number of needles as well as the volumes are small. Hence, the number of possibilities to adapt the seed displacement is reduced as well. The whole algorithm is illustrated in Figure 12 on page 36. It shows how the SI is compared to the SI with the SAA algorithm. If the loss of the V100 is greater than the threshold ($th = 1\%$ and $th = 0.5\%$ for the NPA of 3 mm and 1 mm) the SAA algorithm optionally optimizes the treatment plan. Then two tracks are evaluated where each needle is implanted with the same random implantation error. In the adaption track

there are $1 \leq \text{SAA} \leq N - 1$ adaptions where N is total number of needles. The first needle is never adapted.

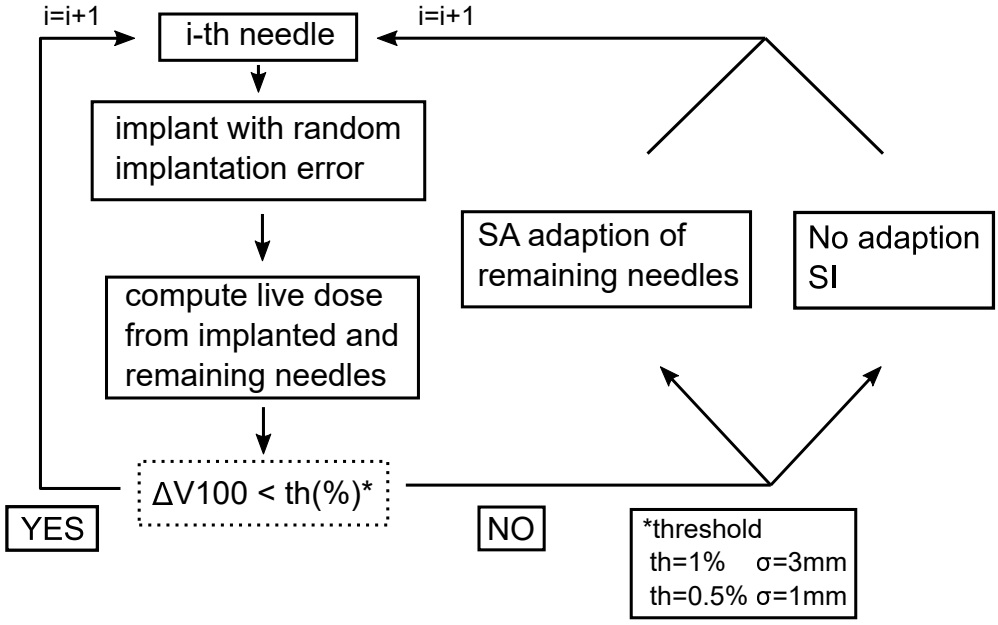

Figure 12: The simulated implantation workflow chart is shown. ΔV100 specifies the change of the V100 due to the shifted implanted needle. The threshold is 1 % for a needle placement accuracy of 3 mm and 0.5 % for 1 mm respectively. If the threshold is exceeded the SAA optionally optimizes the remaining needles.

Ten plans of the F-CTVs 1/3/4/5 are simulated with and without simulated annealing adaption to compare the effect of needle adaption.

The SAA optimizes the dose distribution D_{PP} for the remaining n-i needles to enable correcting an implanted seed deviation resulting in suboptimal dose parameters. Here all remaining trajectories are modified simultaneously within ± 1.5 mm tip point deviation. The stopping criteria are a maximum of 25 iterations or a maximum of iterations equally to five times the number of remaining needles. The online dose is calculated and if the V100 drops more than 1 % for $\sigma = 3$ mm or 0.5 % for $\sigma = 1$ mm the SAA algorithm adapts the remaining needle trajectories.

The error functions are used similar to Table 3 except of the weightings for the two urethra functions that are $w_{2,3} = 0.3$ and the included V200 function ($g2$) equally as in table 4. Further, there is no error function for the prostate tissue.

The SA adapted implants are compared with the simulated implants for all F-CTVs together and for each F-CTV alone. As each F-CTV has a different size, the number of needles and seeds used might differ. This however influences the number of possible SA adaptions.

2.7 Transrectal implantation experiment

A phantom experiment for scenario 3 is conducted in order to test the workflow, determine the seed placement as well as the robotic accuracy and the possibility to register the released seeds in the MRI images. The F-CTV #1 was chosen to be treated by a prescription dose of $D_{pr} = 160\,Gy$ hence this one is best reachable in the phantom setup (see Figure 4 on page 13). The total workflow was tested by implanting two needles with two seeds each. The seeds were located in the MR images and its coordinates were used to optimize the radiation treatment plan with the SAA algorithm. The live trajectory was calculated from the needle guide location of the actual image set. The workflow displayed in 5 on page 14 was followed and is described there more detailed on the given experiment.

Procedure The phantom was positioned on the MRI table as shown in Figure 4 on page 13 with the standard body coil attached. T2-weighted scans of 1 mm slice thickness with an angle of approximately 45° were performed and sent to the RCM software to approve the setup of the robot and phantom. The needle guide was prompted to move into the initial planning position by adjusting the insertion depth and position by aiming at a central point of the lesion. Then the volumes and the F-CTV were contoured with the RCM. The RT-Struct was then manually transferred to the TPS for inverse radiation treatment planning.

(1.) in Figure 5 on page 14 is using the rotation point coordinate from the RCM for the treatment planning and the first needle tip point as treatment target.

(2.) is to determine the live needle trajectory after the RCM movement by the actual rotation- and tip-point. The tip coordinate was localised in the RCM software by searching the nearest coordinate in the MR-image set and the robot automatically positioned the needle guide. Another MRI scan confirmed the latter. The needle guide was re-calibrated on the actual image set to locate precisely the rotation point coordinate. The needle guide tip coordinate can be extracted from the image set as well.

With these coordinates, the needle trajectory is calculated. The insertion depth is measured along the actual needle trajectory from needle guide tip to the target to determine the live needle tip and the seed coordinates in difference to the pre-planned needle. The depth optimizer calculates the optimal insertion depth for the needle by altering the latter in 1 mm steps in the range of $(-3, 3)$ mm and minimizing the SAA objective function. The trajectory is approved or the robot is moved repeatedly to further optimize the needle guide placement.

To implant the needle with the correct insertion depth the length of the needle guide tip to the target point is measured in the software. The needle is placed into the needle guide up to the needle guide tip. Therefore, the needle guide length has to be marked on the needle beforehand. Then the needle is pushed forward about the insertion depth and the seeds are released. The next MRI scan should be acquired along the implantation trajectory with 1 mm slice thickness to register the seeds that are aligned with their long side in the same direction. Here the seeds are seen as circular signal voids in up to four successive image planes and the spacers with positive signal such that the seed

coordinate centre can be registered the most accurate. The SAA algorithm adapts the remaining needle trajectories if necessary. The next needles are implanted the same way.

Evaluation The needle guide accuracy is measured by comparing the pre-planned seed positions to the recalculated approved ones that result from the approved needle trajectory without altering the needle insertion depth. To validate the accuracy of registering seed coordinates in the MRI CT scans were acquired after the experiment and the data sets then were matched with a rigid image registration with the commercial image data toolkit Velocity (varian Medical Systems, Palo Alto, USA). The CT scan seed registration here serves as the gold standard to measure the seed displacement according to the pre-planned and approved seed coordinates and the deviation to the MR-only seed registration.

The experiment is evaluated by measuring two accuracy measures. The first is the spatial deviation, which is the length of the connection vector between planned and experimentally achieved position. The second is the depth deviation, which measures the displacement in relation to the insertion depth. This can be done by finding the coordinate on the needle trajectory with the shortest distance to the displaced seed. The deviation of this coordinate to the seed coordinate on the trajectory is then defined as the depth deviation. This measure along the needle path was also recorded as a quality measure in [42] and is influenced by the physician who inserts the needle. It is calculated by a function, which proceeds the following steps. The plane P is calculated which on one hand contains the displaced seed coordinate (S_D) and one the other hand is perpendicular to the needle trajectory vector $\overrightarrow{\lambda}$ being the normal vector (compare eq. 9). The plane is in a normal form with the constant d calculated by

$$\overrightarrow{S_D} \cdot \overrightarrow{\lambda} = \mathrm{d}, \tag{30}$$

with $\overrightarrow{S_D}$ being the position vector of S_D. The plane P is then given by

$$\overrightarrow{x} \cdot \overrightarrow{\lambda} - \mathrm{d} = 0. \tag{31}$$

Inserting the parameterized form of the needle trajectory as a line

$$\overrightarrow{x} = \overrightarrow{TP} + \mu \cdot \overrightarrow{\lambda} \tag{32}$$

into the normalized plane enables to calculate the parameter

$$\mu = \frac{\mathrm{d} - (\overrightarrow{TP} \cdot \overrightarrow{\lambda})}{\overrightarrow{\lambda}^2}. \tag{33}$$

Inserting μ into the equation 32 results in the coordinate that lies on P and the trajectory with the shortest distance to the displaced seed coordinate. As the trajectory vector $\overrightarrow{\lambda}$ points from the rotation point to the tip point it holds that $\mu > 1$ signifies a depth deviation directed into the patient.

3 Results

3.1 Dose modelling of Iodine-125 seeds

Table 3.1 shows the resulting parameters of fitting the dose values $D_{\theta_i}(r)$ with $f(r) = a\ r^b$ for each angle θ. The seed in this model is aligned along the $\theta = 0°$ axis. It can be seen that the fit functions with θ angles near to 90° have an dose gradient of $\approx 1/r^2$. The data points used for the fitting have the highest distance to the seeds surface and there one expects this dose gradient. For the angles with the seed surface closer to the first data point due to the seed's spatial extent the b value raises up to a dose gradient of $\approx 1/r^2.7$.

θ (°)	a	(95 % confidence bounds)	b	(95 % confidence bounds)
0	2.832	(2.095, 3.569)	-2.609	(-2.799, -2.42)
2	3.079	(2.091, 4.066)	-2.552	(-2.787, -2.318)
5	6.709	(6.385, 7.034)	-2.069	(-2.105, -2.034)
7	5.871	(5.186, 6.557)	-2.404	(-2.49, -2.319)
10	5.338	(4.253, 6.424)	-2.735	(-2.883, -2.587)
15	6.553	(5.354, 7.752)	-2.777	(-2.911, -2.644)
20	7.79	(6.54, 9.04)	-2.762	(-2.879, -2.645)
25	9.213	(8.023, 10.4)	-2.666	(-2.761, -2.572)
30	10.68	(9.661, 11.69)	-2.547	(-2.617, -2.478)
40	13.51	(13.14, 13.88)	-2.293	(-2.313, -2.272)
50	16.11	(15.39, 16.83)	-2.045	(-2.079, -2.012)
60	16.96	(15.99, 17.93)	-1.965	(-2.008, -1.922)
70	16.45	(15.83, 17.08)	-1.953	(-1.982, -1.925)
80	16.29	(15.52, 17.06)	-1.94	(-1.975, -1.904)
90	16.32	(15.44, 17.2)	-1.928	(-1.969, -1.888)

Table 5: The fit parameters of the power function $f(r) = a\ r^b$ for each angle θ of the seed.

The dose distribution of a five seed strand is displayed in Figure 13. Figure 14 on page 41 (a) and (b) show the compared dose planes of the TPS and OCP respectively. Figure 14 c) shows the dose along the x-axis for the y-value ($y = 38.38$ cm) marked with a white line in a), b) and d). The latter (d) shows the gamma map, the visualisation of the gamma test. Red pixels with value 1 have failed, whereas the others have passed. The closer the pixel is near zero the better the agreement. Here the dose was normalized to 290 Gy which is the dose accounted for the V200 of the 145 Gy prescription dose for prostate seed-BT. The gamma test with the threshold of 1 % = 2.9 Gy and 1 mm passed for 98.5 % of the pixels.

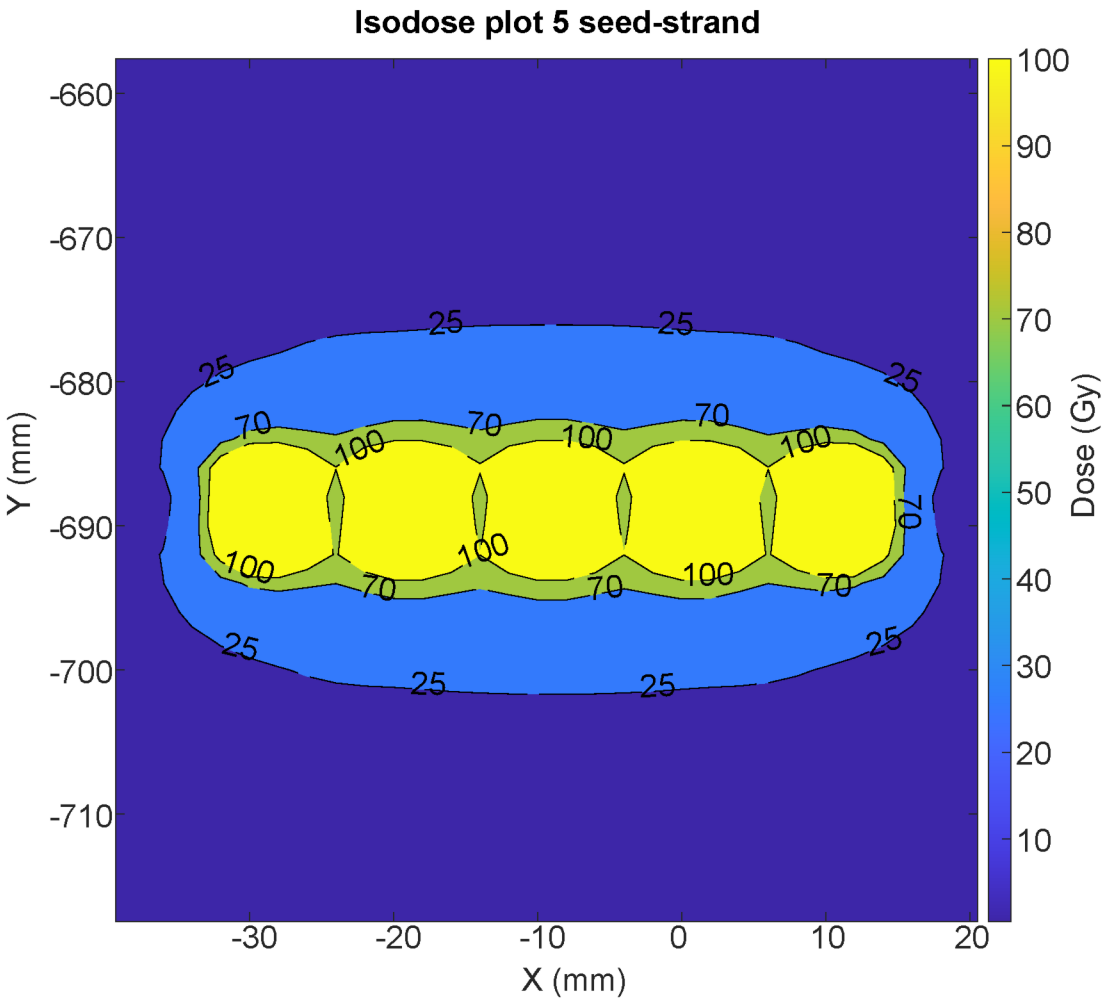

Figure 13: A filled isodose contour plot through the centres of five stranded seeds lined along the X-axis with the isodose lines $(100, 70, 25)$ Gy. Adapted from own publication [61].

3.2 Path planning and needle candidate domain

Scenario 1 The path planning is visualised in Figure 15 on page 42. Figure 15(a) displays the injection points IP_i dismissed due to the checkpoint sphere inside of the liver shape CP_i. This is the first OAR filter where the checkpoint sphere's radius r is the distance of the liver contour's median to the target volume's median. Figure 15(b) shows all injection points and marks the valid ones remaining after the filter process. The total number of injection points of 5699 was reduced during the path planning to 1568 in 9.7 seconds. The first OAR filter removed 44.7 % and the next 290 filter steps 27.8 % of all injection points. Removing the neighbouring needle candidates that were located closer than 2 mm to each other reduced the number of injection further to 827 injection points

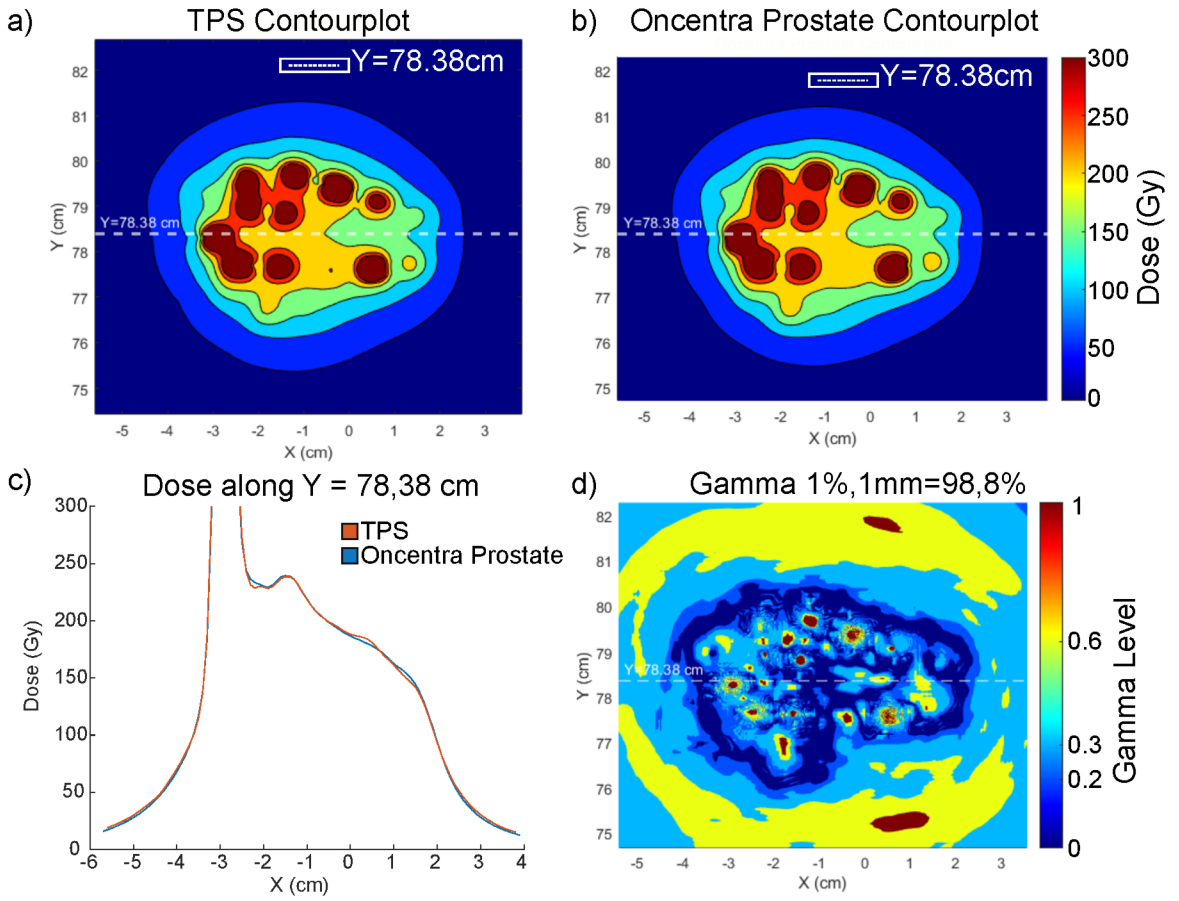

Figure 14: a) and b): The isodose plot of the compared dose planes calculated by the TPS (a) and OCP (b). The colours red, orange, yellow, green, cyan, blue and dark blue specify the colour wash of the isodose lines of $(300, 250, 200, 150, 100, 50, 0)$ Gy respectively. c): The line plot along $Y = 78,38$ cm of both planes shown in a) and b) as the white dashed line. d): The gamma plane resulting from the gamma test with gamma $= 1\,\%$, 1 mm with $100\,\% = 290$ Gy of the planes of a) and b). The colours dark red, yellow, cyan, blue and dark blue specify the colour wash of the gamma levels (1, 0.6, 0.3, 0.2, 0) respectively. A failed pixel has the gamma level 1, all other levels count as a passed pixel. Adapted from own publication [61].

(14.5 % of the total number) that were considered for the needle candidates. Figure 15(c) visualises the number of filtered injection points over the number of executed filters. The first filter is reducing the injection points in the direction of the treatment couch as well as the first OAR filter that locates the majority of the filtered injection points which can be seen in the outer graph. The yellow background marks the other used OAR filters with an adapted radius defined by equation 11. On the blue background the filter steps with the varied TP which were the minimum and maximum contour points of the PTV in all room directions with additionally varied radius were conducted. The inner graph

shows that these varied filter functions detected up to 160 invalid injection points per evaluation.

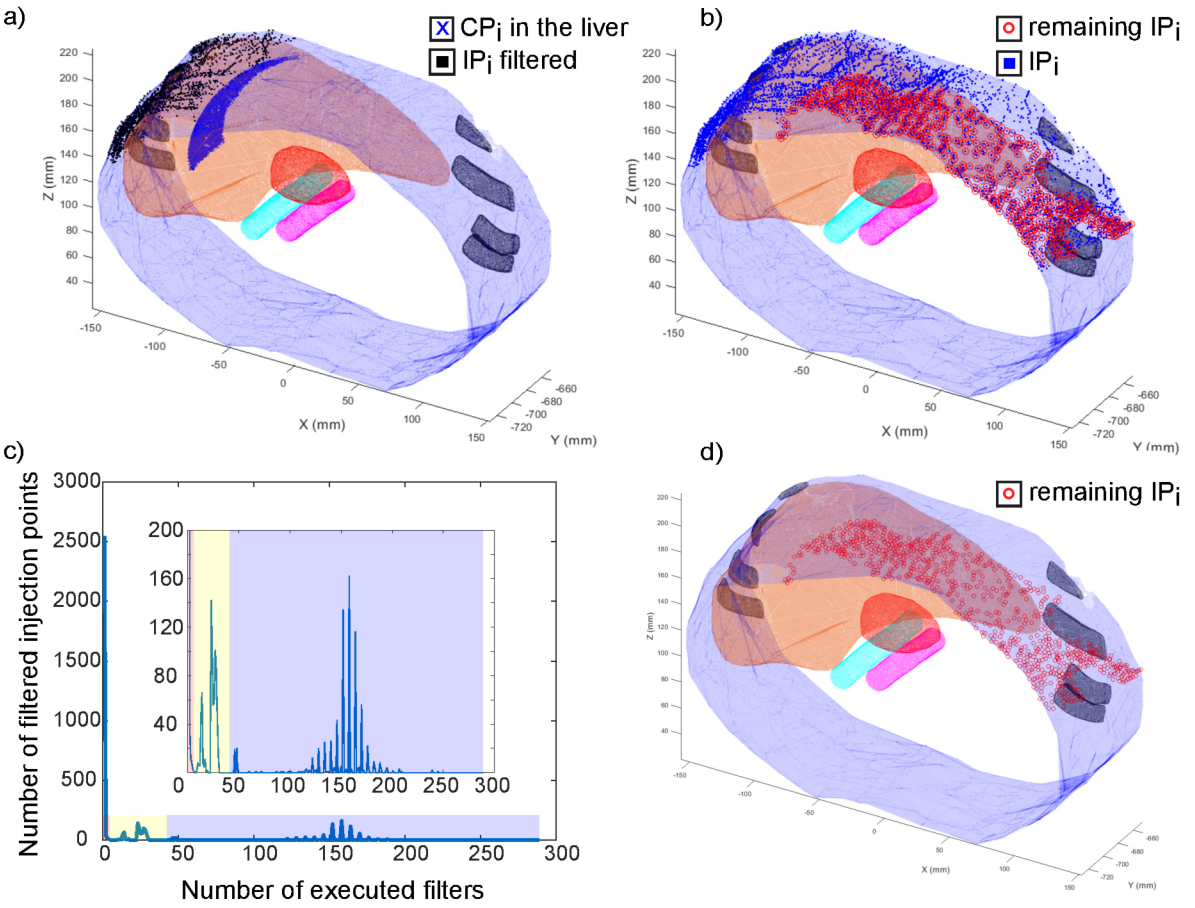

Figure 15: a): The checkpoints CP_i (blue x) have the same distance to the median of the target volume than the liver median and are located inside of the liver. Therefore the associated injection points IP_i (black dot) are removed. b): Shows all injection points (blue dot) and the remaining ones (red circle). c): Plots the number of filtered injection points over the number of executed filters hence demonstrating the effectiveness of each filter. The inner graph zooms into the range of $[0, 200]$ removed injection points. d): The remaining IP_i (red circle) used for the needle candidate domain. Adapted from own publication [61]

The resulting injection points are shown in Figure 15(d). The needle candidate domain contained 1971 tip points and the amount of valid needle trajectories to deliver one seed was $1.01\ 10^6$. From two to five seeds the amount of needle trajectories decreased from $8\ 10^5$ to $8\ 10^4$. Figure 16 on page 43 demonstrates a decreasing number of valid injection points with an increasing number of seeds per needle due to the longer required path length in the target volume. For needles with one seed, a great number of needle tip points were accessible by all injection points (Figure 16(a)). These were the ones on the

ground and more to the liver directed opposite to the injection points located upside and on the left. For the needle candidates with three seeds the area of tip points best reachable was the same as for the one seed needles but smaller, because three seed-strands could still be placed by needle candidates from upside (Figure 16(b)). However, this changed with five-seed-strands where the tip points on the left were still reachable by 40 % of the injection points from the right side with lateral needle trajectories (Figure 16(c)). Five-seed-strands from upside would have resulted in seeds outside of the target volume whereas they were filtered out.

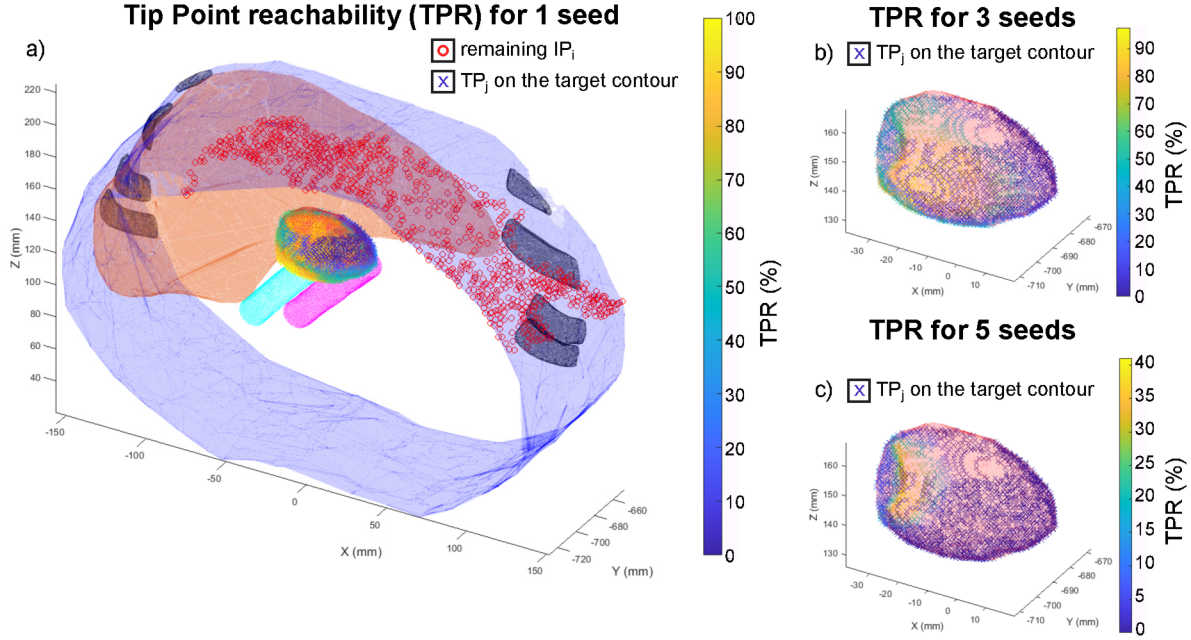

Figure 16: a): The target volume's contour points are the needle candidates' tip points. Their colours are defined by the percentage of injection points IP$_i$ (red circle) that combine to a valid needle candidate containing one seed (Tip point reachability, TPR) if the seed is located inside of the target volume. b) and c): The target volume with the tip points coloured after the TPR for a three seed and five seed strand respectively. Adapted from own publication [61]

The tip points, which were best reachable therefore were the ones on the right part of the target volume near the liver as most of the injection points were located on the right side and upside. The path planning and generation of the needle candidate domain took 0.7 min.

Scenario 2-3 There were initially 2072 tip points for scenario 2 that were reduced to 1431 tip points by omitting all second needle tips with a quadratic distance of less than 1 mm. After filtering for the seed positions inside the prostate CTV and outside of the urethra margin there remained 625 tip points. The needle candidate domain had eleven

needle candidates containing four seeds, 152 with three, 373 with two and 625 needle candidates with one seed.

In the scenario 3 the number of needle candidates per lesion was highly reduced due to the smaller amount of F-CTVs' contour points. The number of needle candidates counted 33.8 ± 12.6 with two- and one stranded seeds for the lesions 1-5.

3.3 Treatment plan optimization

Scenario 1 The optimization algorithms achieved the treatment aims with a high V100. The development of the latter as well as the V150 and V200 during each optimization step of the four algorithms is displayed in Figure 17 on page 45 for one example treatment plan. For the greedy optimizer each step signifies a solved sub-problem with a needle candidate chosen for the treatment plan. As the dose contribution of each needle depends on the number of stranded seeds, the increase of the dose coverage is nonlinear. Therefore, the curves increase sharply for the first needles containing five seeds. When the number of seeds is reduced, the curves flatten. Because of the high dose in the seed's close vicinity, the V200 is also apparent in the first optimization step. Due to superposition of lower dose components, the V100 value increases more than the V150 and V200 values. However, for the last needles it is the other way round as they are allowed being placed closer to the higher dose region in equation 15 on page 25.

The remove-seeds algorithm efficiently reduces the V200 by $\approx 15\,\%$ while losing only a small amount of dose coverage by the V100 of $\approx 1\,\%$. The depth optimizer improves the dose homogeneity slightly by an increased V100 and decreased V150 and V200. The coverage optimizer sets a new needle increasing the V100 over 99 % to the disadvantage of raising the V150 and V200 by 7 % and 6 % respectively.

Figure 18 on page 46 shows the structure set with a treatment plan configuration of 13 needles and 35 seeds and the prescription dose envelope. The V100, V150 and V200 were acceptable with $(99.0, 75.9, 34.2)\,\%$. The D90 $> 120\,\%$ D_{pr} was achieved with 124.8 Gy.

Ten treatment plans with $(2 \times 2 \times 2)\,\mathrm{mm}^3$ grid resolution have been generated to test the stability and statistical variability of the inverse optimization process. The referring box and whisker plots are shown in Figure 19 on page 47. The treatment aims of a V100 close to 100 % were achieved in all ten plans with V100 $= (99.1 \pm 0.3)\,\%$ (Figure 19(a)). The V150 and V200 were $(76.4 \pm 2.5)\,\%$ and $(44.5 \pm 5.5)\,\%$ respectively. In addition, the D90 $= 125.9 \pm 3.6$ Gy value was over 120 Gy for all ten plans matching the treatment aim of good dose coverage (Figure 19(d)). The plans contained 10.7 ± 1.3 needles with 34.0 ± 0.8 seeds (Figure 19(b)) and the optimization time median was 2.6 min with the 75 % percentile of 3.2 min and 25 % percentile of 2.1 min (Figure 19(c)). However, two outliers regarding the optimization time were detected with 10.5 min and 29.2 min. Here the coverage optimizer called the objective function repeatedly for many needle candidates without fulfilling the required passing condition such as $\frac{V_{pr,TV}}{V_{pr}} > 0.7$. The TPS total running time median was 4.4 min which includes loading the structure set, the dose modelling data, the path planning and the needle candidate generation and the inverse optimization.

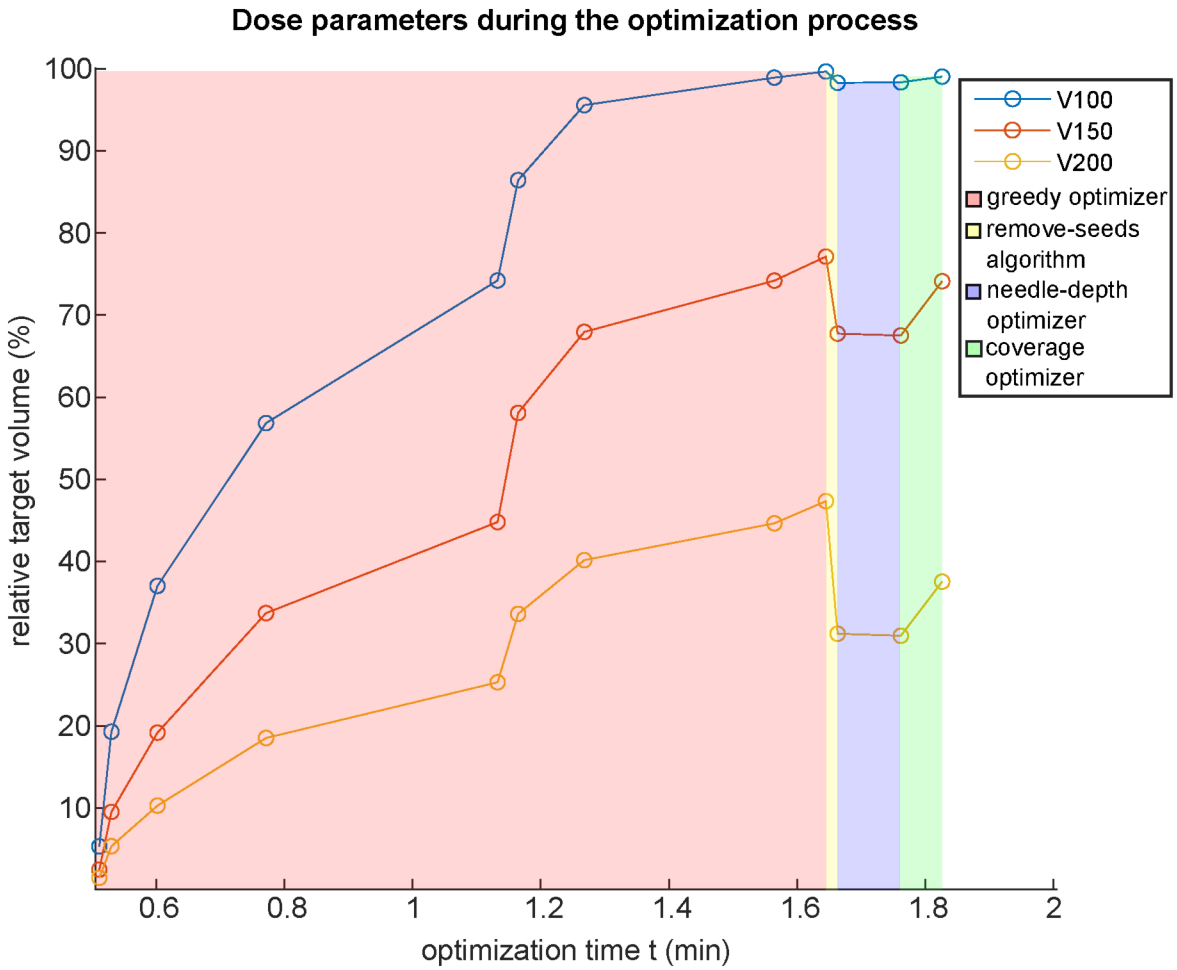

Figure 17: The optimization time-resolved dose parameters V100 (blue), V150 (red), V200 (yellow) as the percentage of the target volume. Each background colour shows the currently running optimizer. Adapted from own publication [61]

Scenario 2 Table 6 on page 48 shows the planning results and dose constraints for the optimization with the prescription doses of $D_{pr,1} = 145\,Gy$ and $D_{pr,2} = 115\,Gy$. For both prescription doses the ten plans were acceptable in terms of the most important dose constraints which are the V100, D90, urethra D10, D30 and rectum $D_{2\,cc}$ and $D_{0.1\,cc}$. However, the urethra D30 was violated slightly three times of ten for $D_{pr,1}$ and eight of ten times for $D_{pr,2}$. The V150 and V200 were higher than the proposed constraints. The results for $D_{pr,1} = 145\,Gy$ were better in terms of the urethra D30 constraint indicating that the greedy optimizer setup fits better to the higher prescription dose. The difference in the results can be explained by the seed's nonlinear dose gradient leading to different spatial spreading of the valid dose range for the needle tips and seeds in equation 15 on page 25. For $D_{pr,2} = 115\,Gy$ the optimal seed spacing to each other and the urethra is

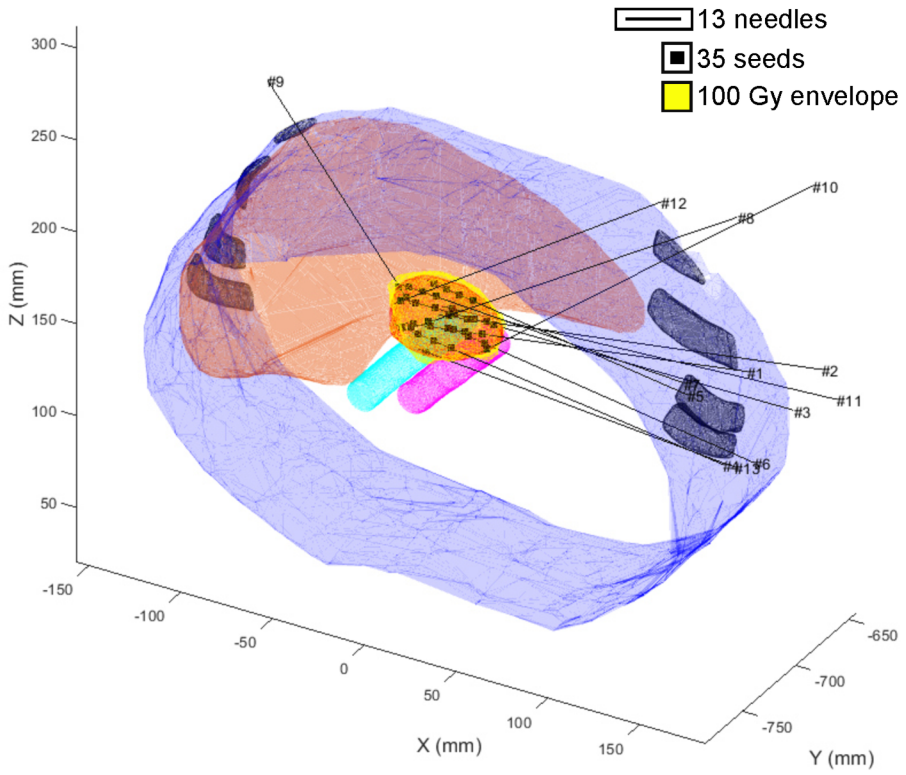

Figure 18: Overview of one of the ten final treatment plans containing 13 needles and 35 seeds (black dots). The $D_{pr} = 100\,Gy$ dose envelope (yellow) encloses the target volume (red contour). Adapted from own publication [61].

increased which results in a modified optimization problem.

Figure 20 on page 49 shows the overview, a central dose plane and the dose volume histogram of one of the ten plans with the prescription dose $D_{pr} = 145\,Gy$. The very steep dose falloff for the urethra in the high dose region is needed to fulfil the dose constraints D30 and D10, the points on the urethra in the dose-volume histogram (DVH) (Figure 20 c)) for the volume 30 % and 10 %. In the dose plane (Figure 20 b)) the orange contour is $D = 1.5\,D_{pr} = 217.5\,Gy$. It may only cover 10 % of the urethra to fulfil the D10 constraint. Here only the green contour showing the 145 Gy isodose covers the area around the urethra such as it is expected for state of the art prostate seed-BT as well.

Scenario 3 Examples of the V100, V150 and V200 progression during the optimization steps for different F-CTVs are displayed in Figure21 on page 50.

Each point on the red background displays the dose parameters V100, V150 and V200, which are changed when a new needle is added to the solution space. On the grey background on each optimization step, a needle trajectory is modified within the simulated annealing optimizer. On the blue background, the "remove outer seed function" was

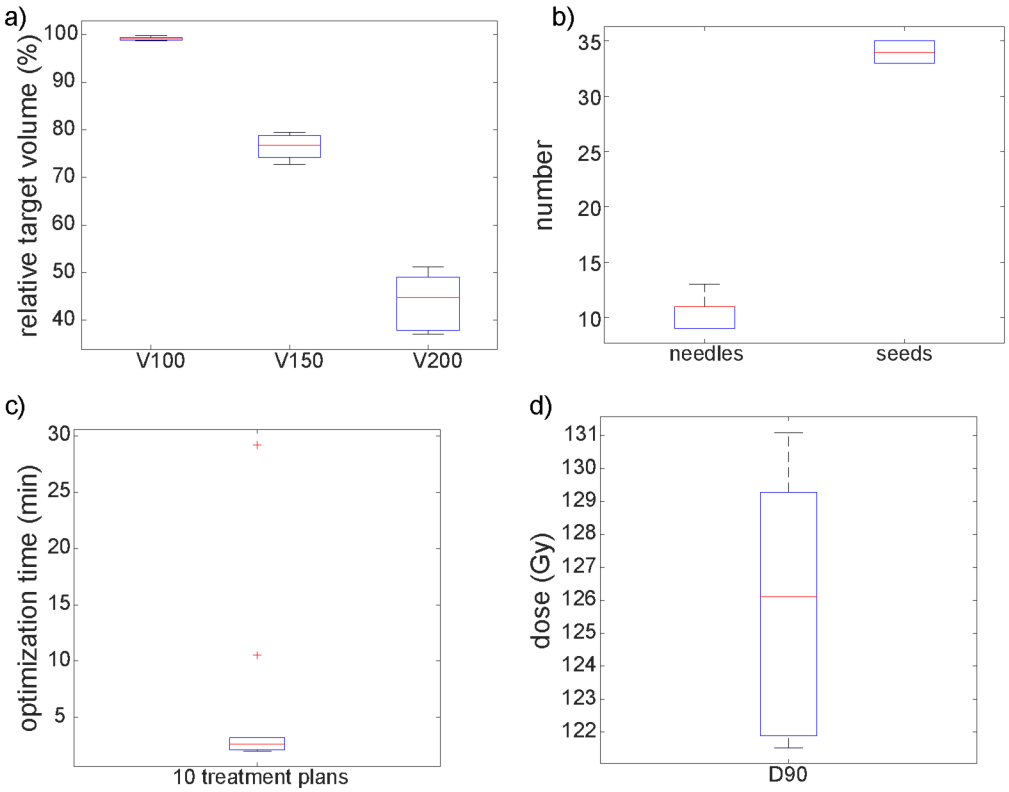

Figure 19: Box and whisker plots of the ten treatment plans are shown with the median (red line), the 75$^{\text{th}}$ and 25th percentiles (top and bottom box edges), whiskers (dashed vertical line and horizontal line) for extreme data values and outliers (red cross). a): The dose parameters V100, V150 and V200 as percentage of the target volume. b): The number of used needles and seeds. c): The optimization time containing two outliers. d): The D90 dose parameter for the target volume. Adapted from own publication [61]

executed. The greedy optimizer stops the optimization with a V100 around $90-95\,\%$ and the simulated annealing optimizer then is able to optimize the coverage with this amount of needles and seeds. On Figure 21b) a seed is removed resulting in a drop of the V150 and V200 while the V100 is reduced a little. The second simulated annealing algorithm is then able to optimize the $V100 = 100\,\%$ without this seed.

The overall percentage of the F-CTVs of L1/3/4/5 and with the prescription dose $D_{pr} = 160\,\text{Gy}$ yielded $V100 = 99.2 \pm 1.2\,\%$. The trajectories circumvented the urethra as intended to reach the F-CTV #2, but due to the limited reachability the V100 yielded $V100 = 93.9 \pm 4.5\,\%$ for $D_{(pr,2)} = 115\,\text{Gy}$. For $D_{pr,1} = 145\,\text{Gy}$ there was no acceptable dose coverage reachable.

The urethra D10 $< 150\,\%$ and D30 $< 130\,\%$ of the prescription dose as well as the rectum constraints were met easily for the lesions L1/3/4/5 with together $D10 = 42.8 \pm 14.9\,\text{Gy}$, $D30 = 32.0 \pm 10.7\,\text{Gy}$ of the urethra and $D_{0.1\,\text{cc}}(\text{rectum}) = 37.3 \pm 44.4\,\text{Gy}$

				CTV				urethra		rectum	
	D_{pr} (Gy)	#N	#S	V100 (%)	V150 (%)	V200 (%)	D90 (Gy)	D10 (Gy)	D30 (Gy)	$D_{2\,cc}$ (Gy)	$D_{0.1\,cc}$ (Gy)
mean	145	23.5	47	95.8	64.6	28.6	167.84	194.6	185.5	69.1	126.6
std (±)	-	1.4	1.2	0.5	3.1	2.6	3.4	5.6	5.1	2.3	11.4
constraints	-	-	-	> 95	< 50	< 20	> 145	< 217.5	< 188.5	< 145	< 217.5
mean	115	18.2	38.5	95.4	65.6	31.2	131.3	162.0	152.6	57.3	107.3
std (±)	-	1.1	0.7	0.4	1.9	1.6	1.3	4.4	3.6	1.9	13.3
constraints	-	-	-	> 95	< 50	< 20	> 115	< 172.5	< 149.5	< 115	< 172.5

Table 6: The planning results on the prostate CTV of 10 plans each with $D_{pr,1} = 145\,Gy$ and $D_{pr,2} = 115\,Gy$.

and $D_{2\,cc}(\text{rectum}) = 14.8 \pm 13.2\,Gy$ for the rectum. For the lesion #1 closest to the rectum its constraints were $D_{0.1\,cc} = 110.8 \pm 16.8\,Gy$ and $D_{2\,cc} = 36.3 \pm 3.9\,Gy$. For all F-CTVs 5.10 ± 1.25 needles and 6.50 ± 1.34 seeds were used.

3.4 In-vivo seed displacement adaption

Scenario 1 The pre-treatment plan as well as the SAA and SIs are visualised in Figure 22 on page 51. Figure 22 b) and d) show how the needle tip position is changed during each SAA optimization step. The last position before the simulated implantation is shown as a triangle. Then the random SI with a NPA of b) 1 mm (green x) and d) 3 mm (blue x) is shown. c) Shows the two SIs without prior SAA optimization.

Table 7 on page 52 displays the resulting treatment parameters of one plan with ten SIs. The D1(aorta) was reduced on average (mean± standard deviation) in the SAA setting with an NPA of ±1 mm from initially 96.98 Gy to $80.44 \pm 4.64\,Gy$ and to $83.56 \pm 8.37\,Gy$ for an NPA of ±3 mm. The other constraint mean values remained constant. The SIs without adaptation showed better results for the smaller NPA of 1 mm with mean values near to the pre-plan. For a NPA of ±3 mm the plan parameters differed more which resulted in higher standard deviations. Figure 23 on page 53 shows the bar plots of ten SIs comparing simulated implants with and without SAA for different organ at risks.

Scenario 2 The simulation results are displayed in Table 8 on page 52. Four cases can be distinguished for each unadapted vs. adapted SI. On one hand differed the prescription dose of $D_{pr} = 145\,Gy$ for the monotherapy or $D_{pr} = 115\,Gy$ for the combined therapy with additional 40 Gy EBRT as defined in chapter 2.1.2. On the other hand the NPA was varied of 1 mm or 3 mm.

The simulated implantation without further adaption for $D_{pr} = 145\,Gy$ and NPA of 1 mm showed very good results close to the pre-plans (Table 8 row 1). The constraints for the V100 and D90 were fulfilled as well as the constraints for urethra and rectum. If such a high robotic implantation accuracy were achievable, the in-vivo plan adaption

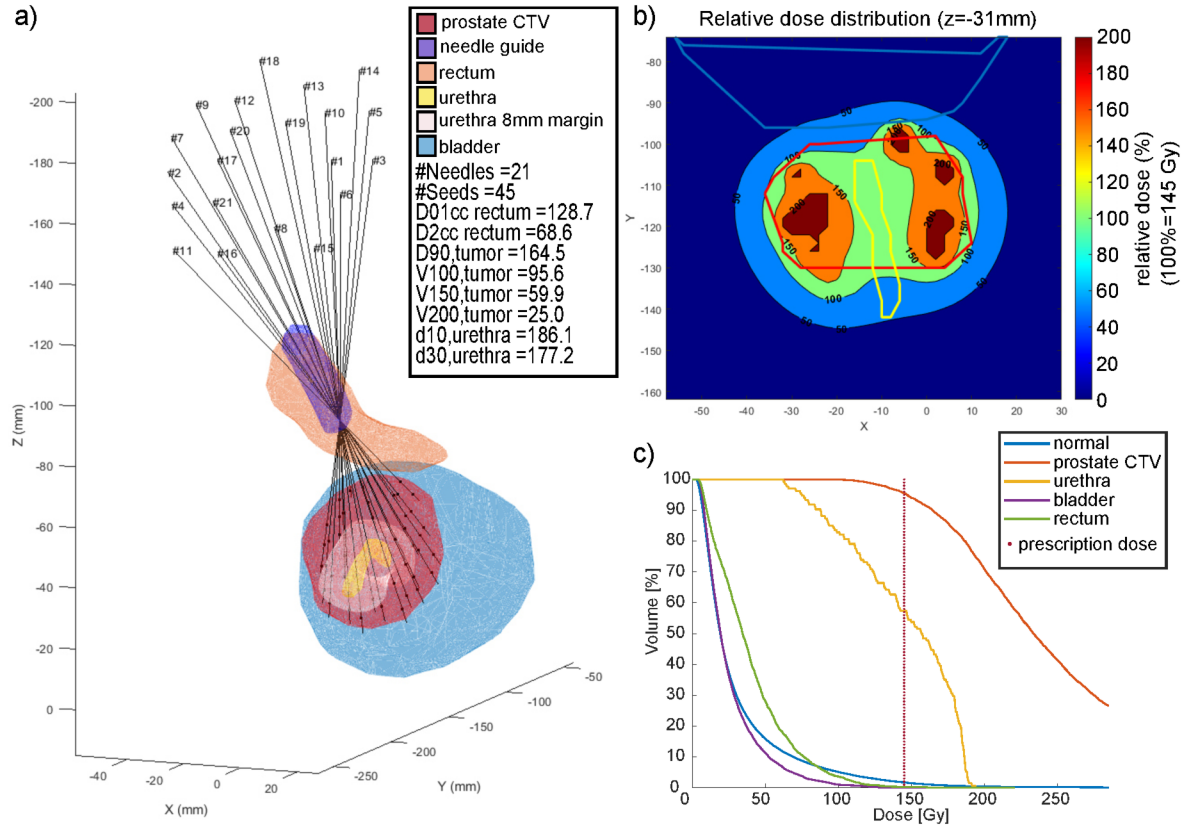

Figure 20: a) The plan overview with the volume structures, needles and seeds. b) The dose distribution for the plane z=31 mm. c) The plan's DVH.

would only be necessary if a seed strand is displaced strongly by mistake.

With a raising NPA of 3 mm the V100 dropped to 93.6 ± 1.5mm and the D90 to 155.8 ± 4.4 Gy (Table 8 row 3). Additionally the D30(urethra) of 192.5 ± 13.9 mm slightly violated the planning constraint. Three of the ten plans fulfilled the D30(urethra) constraint but three had a D30 > 200 Gy as well.

The greedy adaption algorithm for the NPA of 1 mm and 145 Gy showed a reduced dose in the CTV with the V150 and V200 fulfilling the planning constraints but with a reduced V100 of 93.6 % as well (Table 8 row 2). The urethra constraints however were much lower than the pre-planned values. These results can be attributed to the objective function where the urethra sparing is weighted strongly with $w_{2,3} = 0.3$ against the V100 weighting $w_1 = 1$. The optimizer obviously chose repeatedly to move the needle away from the urethra resulting in a more homogeneous and widespread dose distribution to the peripheral prostate and the neighbouring normal tissue.

The prescription dose of 145 Gy with a higher NPA of 3 mm showed a more reduced V100 and higher standard deviations especially for the dose constraints evaluating a small volume such as the rectum $D_{0.1\,cc}$ and the D10(urethra) (Table 8 row 4). However, for both cases the D90 still fulfilled its dose constraint such that the therapy should still

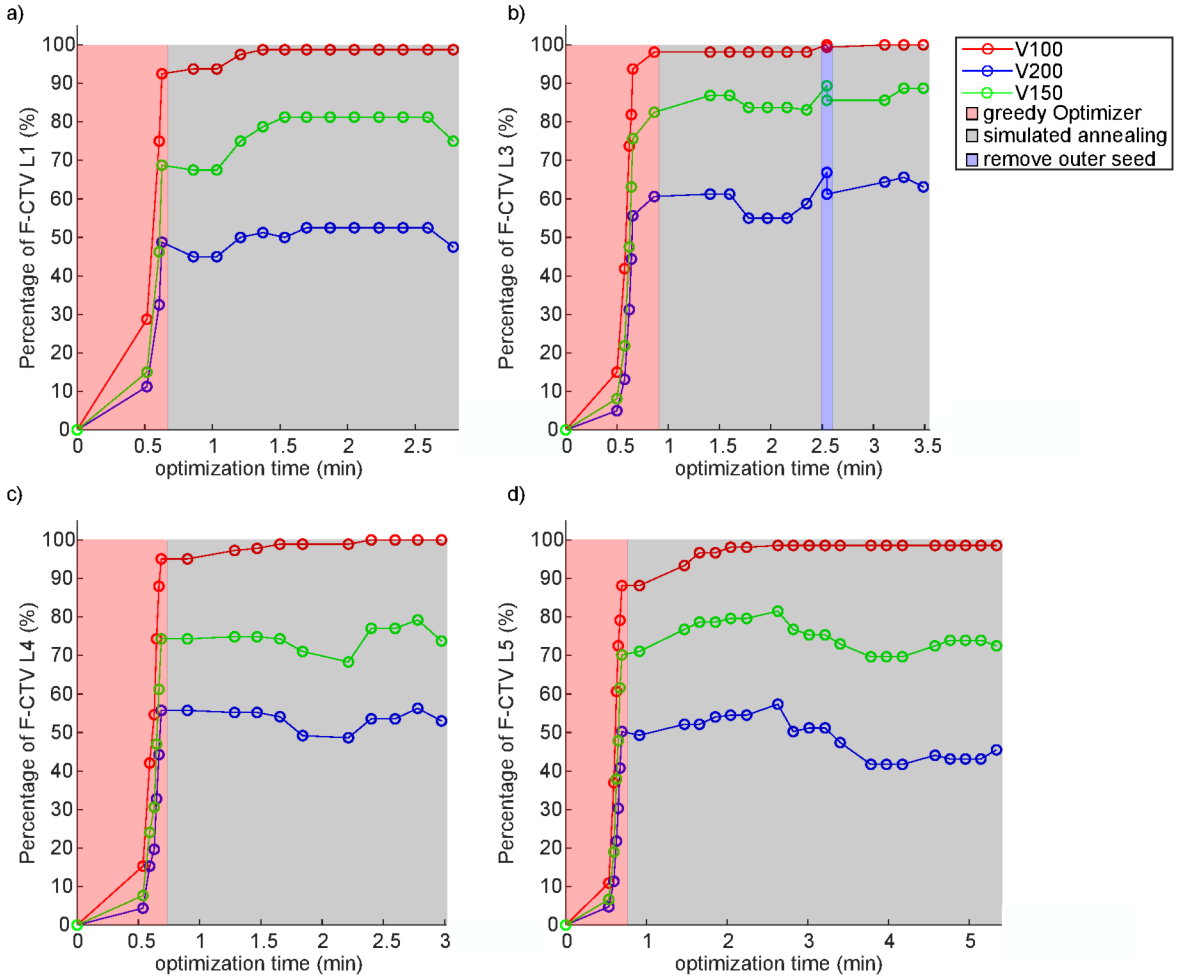

Figure 21: The dose constraints V100, V150 and V200 are shown along each optimization step over the optimization time. a)–d) show one optimization of the lesions L1/3/4/5. The red background marks the greedy optimizer where each data point specifies a needle added to the solution space. The grey background shows the simulated annealing optimization where each data point signifies one needle shifted to a new position. The blue background shows the remove outer seed function where a seed is removed while reducing the V200 at most.

be successful.

The SIs for $D_{pr} = 115\,Gy$ as well as the pre-plans resulted in a D30(urethra) slightly higher than the planning constraint (Table 8 row 6). The best results however achieved the 1 mm greedy adaption optimizer with an even better V100, V150, V200 and D30(urethra) than the means of the pre-plans.

The SI without adaption here resulted in dose constraints very close to the pre-plan mean values (Table 8 row 5).

However, for the SIs with a higher NPA of 3 mm the urethra dose constraints D10 and D30 were both violated definitely with high standard deviations (Table 8 row 7).

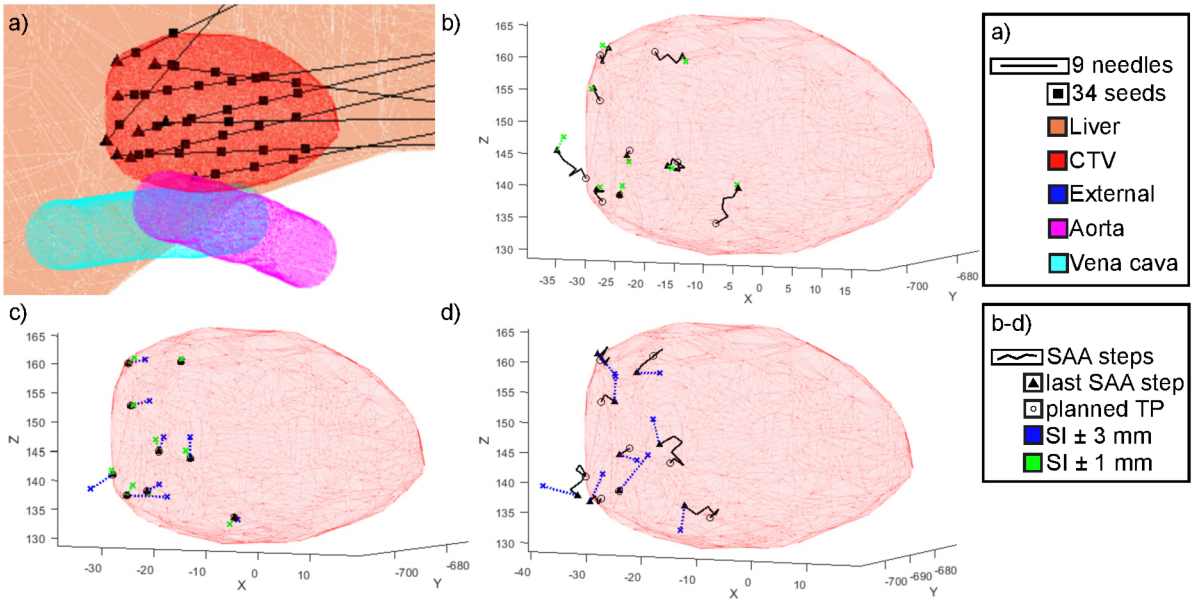

Figure 22: The CTV with the visualised pre-planned, intermediate (line corners b) and d)) and final needle tip coordinates (green NPA of 1 mm, red of 3 mm), of each scenario compared. a) Closer view on the target volume with seeds (squares) and the needle tips (triangles) b)SI with SAA and 1 mm NPA. c) SI with $\pm 1; 3$ mm NPA. d) SI with SAA ± 3 mm NPA. Adapted from [62].

These can be attributed to the pre-plans' needles close to the urethra shifted towards the urethra during the SI. The rectum $D_{0.1\,cc}$ mean was acceptable, but there were two outliers that violated this constraint with 282.0 Gy and 312.6 Gy resulting in a high standard deviation of 81.9 Gy. Here seeds were placed too near to the rectal wall.

The greedy adaption however showed a D10 and D30 close to the pre-plans even for the NPA of 3 mm (Table 8 row 8). The D10(urethra) $= 166.0 \pm 7.7$ Gy showed that the optimizer chose to move the nearest needles away from the urethra. The adaption distance of 1.5 mm here was sufficient to hold the urethra D10 close to the pre-plans' mean value. Considering the same V100 (93.0 ± 2.7 % (SI) vs. 92.7 ± 1.7 (GA)) the greedy adaption simulation showed better outcomes with better urethra and rectum sparing in contrast to the SI plans.

Scenario 3 The resulting V100, V150 and V200 of the pre-plans PP, SIs and SAAs of ten plans each of the lesions L1/3/4/5 for a NPA of 1 mm and for the NPA of 3 mm are displayed in Figure 24 on page 54.

An NPA of 1 mm led to an in-vivo V100 of around 12 % higher than the NPA = 3 mm NPA for both SI and SAA. The SAA showed an in-vivo V100 benefit of about 2 % to the SIs for both NPAs. The SAA algorithm was executed 1.88 ± 0.82 times for each plan for NPA = 1 mm and 2.70 ± 1.81 times for NPA = 3 mm respectively. Even though the threshold of coverage loss was 0.5 % for NPA of 1 mm against 1 % for the NPA of 3 mm the higher uncertainty for needle displacement resulted in more adaptions per simulated

	initially	SI ± 1mm		SI ± 3mm	
		SAA	SI	SAA	SI
V100 (%)	99.12	98.52 ± 0.29	98.85 ± 0.42	97.01 ± 1.21	96.02 ± 1.30
V150 (%)	78.04	75.71 ± 1.40	77.43 ± 0.52	71.16 ± 3.53	70.25 ± 4.31
V200 (%)	48.52	48.27 ± 4.86	48.64 ± 1.98	45.93 ± 6.26	41.25 ± 7.70
D1 aorta (Gy)	96.98	80.44 ± 4.64	$97,72 \pm 4.68$	83.56 ± 8.37	102.10 ± 10.69
D1 vena cava (Gy)	69.92	67.61 ± 3.95	71.06 ± 3.40	70.32 ± 7.62	76.19 ± 10.54
D1 liver (Gy)	89.82	88.65 ± 8.38	87.92 ± 3.63	85.97 ± 14.42	85.70 ± 15.15
D1 normal tissue (Gy)	118.12	119.20 ± 2.90	118.93 ± 2.51	118.62 ± 5.65	125.74 ± 7.70
coin	0.74	0.74 ± 0.02	0.74 ± 0.01	0.73 ± 0.03	0.69 ± 0.03

Table 7: Treatment plan parameters (mean± standard deviation) before and after SI ± 1mm and SI ± 3 mm with SAA and SI for the liver simulation of ten plans.

						CTV				urethra		rectum	
		D_{pr} (Gy)	NPA (mm)	#N	#S (%)	V100 (%)	V150 (%)	V200 (Gy)	D90 (Gy)	D10 (Gy)	D30 (Gy)	$D_{2\,cc}$ (Gy)	$D_{0.1\,cc}$
SI	mean	145	1	23.5	47.0	95.3	63.3	27.8	165.0	196.6	186.6	69.7	123.8
	std (±)		-	1.4	1.2	0.7	3.5	3.1	3.3	7.2	7.4	4.2	11.9
GA	mean	145	1	23.5	47.0	93.6	49.2	19.4	154.9	169.8	161.0	72.8	142.9
	std (±)		-	1.4	1.2	0.7	2.6	1.4	2.7	4.8	3.9	2.7	17.9
SI	mean	145	3	23.5	47.0	93.6	54.9	24.2	155.8	202.3	192.5	69.3	137.7
	std (±)		-	1.4	1.2	1.5	5.5	2.8	4.4	15.6	13.9	8.0	42.7
GA	mean	145	3	23.5	47.0	91.7	44.8	19.4	148.1	177.5	167.4	64.7	116.1
	std (±)		-	1.4	1.2	1.5	4.3	1.8	4.5	12.7	9.5	5.7	16.8
	constr.	145	-	-	-	> 95	< 50	< 20	> 145	< 217.5	< 188.5	< 145	< 217.5
SI	mean	115	1	18.2	38.5	95.0	63.8	29.8	129.4	161.9	152.2	57.9	110.2
	std (±)		-	1.1	0.7	0.8	2.6	2.1	2.5	7.6	6.9	3.4	16.2
GA	mean	115	1	18.2	38.5	95.7	62.5	28.0	130.9	162.7	150.3	60.3	117.4
	std (±)		-	1.1	0.7	0.7	2.4	1.4	2.5	3.4	1.7	2.4	17.5
SI	mean	115	3	18.2	38.5	93.0	60.3	44.8	122.2	184.4	169.6	60.2	143.5
	std (±)		-	1.1	0.7	2.7	4.8	3.0	6.5	25.8	21.8	5.1	81.9
GA	mean	115	3	18.2	38.5	92.7	53.9	23.9	121.3	166.0	153.2	60.5	122.6
	std (±)		-	1.1	0.7	1.7	3.6	1.8	3.9	7.7	5.2	8.5	32.3
	constr.	115	-	-	-	> 95	< 50	< 20	> 115	< 172.5	< 149.5	< 115	< 172.5

Table 8: The simulated implantation results on the prostate CTV of 10 pre-plans (SI) and additionally with the greedy adaption (GA).

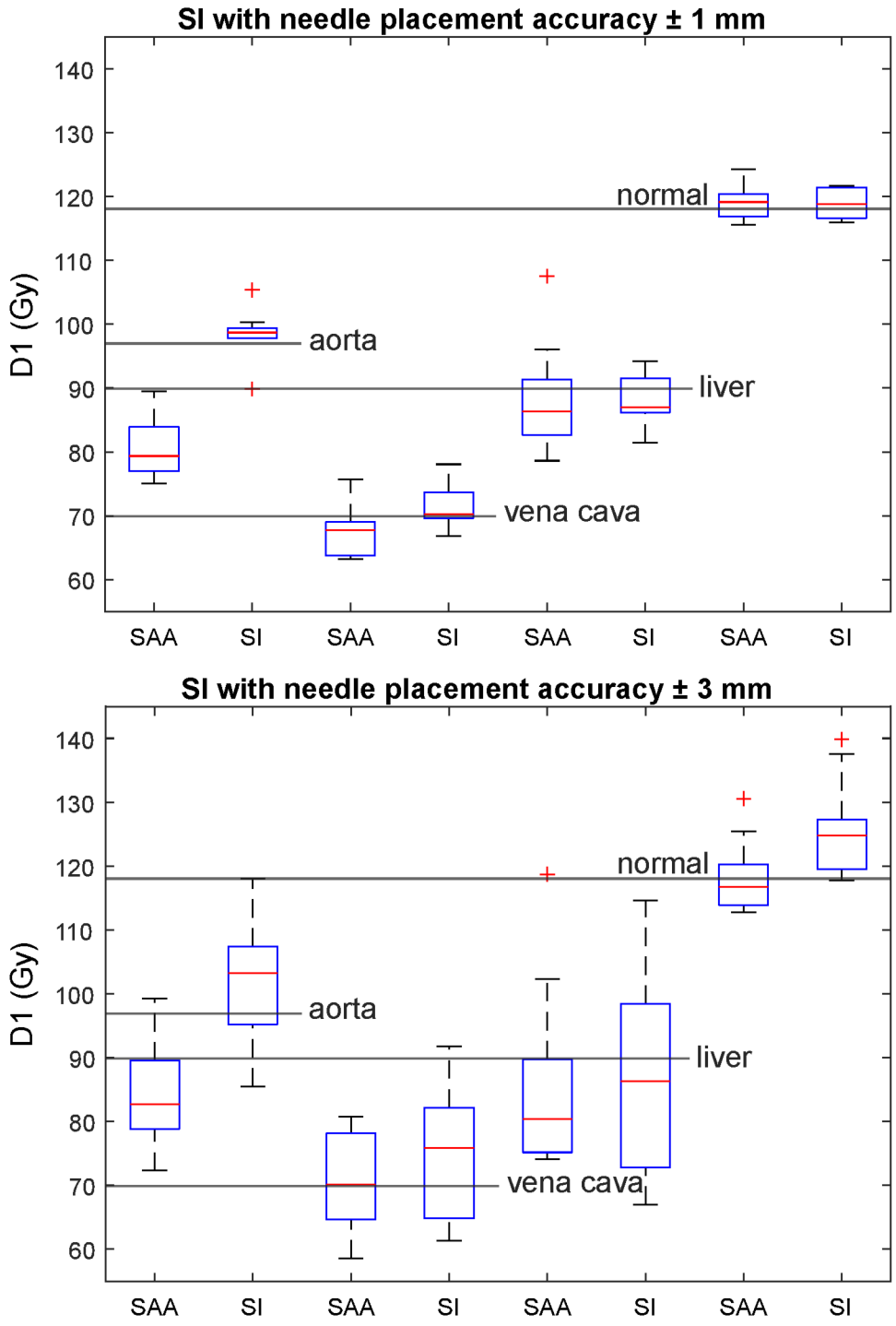

Figure 23: Bars and whisker plots of the OAR D1 doses of SIs with the needle placement accuracy of ±1 mm or ±3 mm with the median (red line), 25th and 75th percentile (blue bar), whiskers and outliers (red cross). The annotated lines (grey) display the pre-planned doses. Adapted from [62].

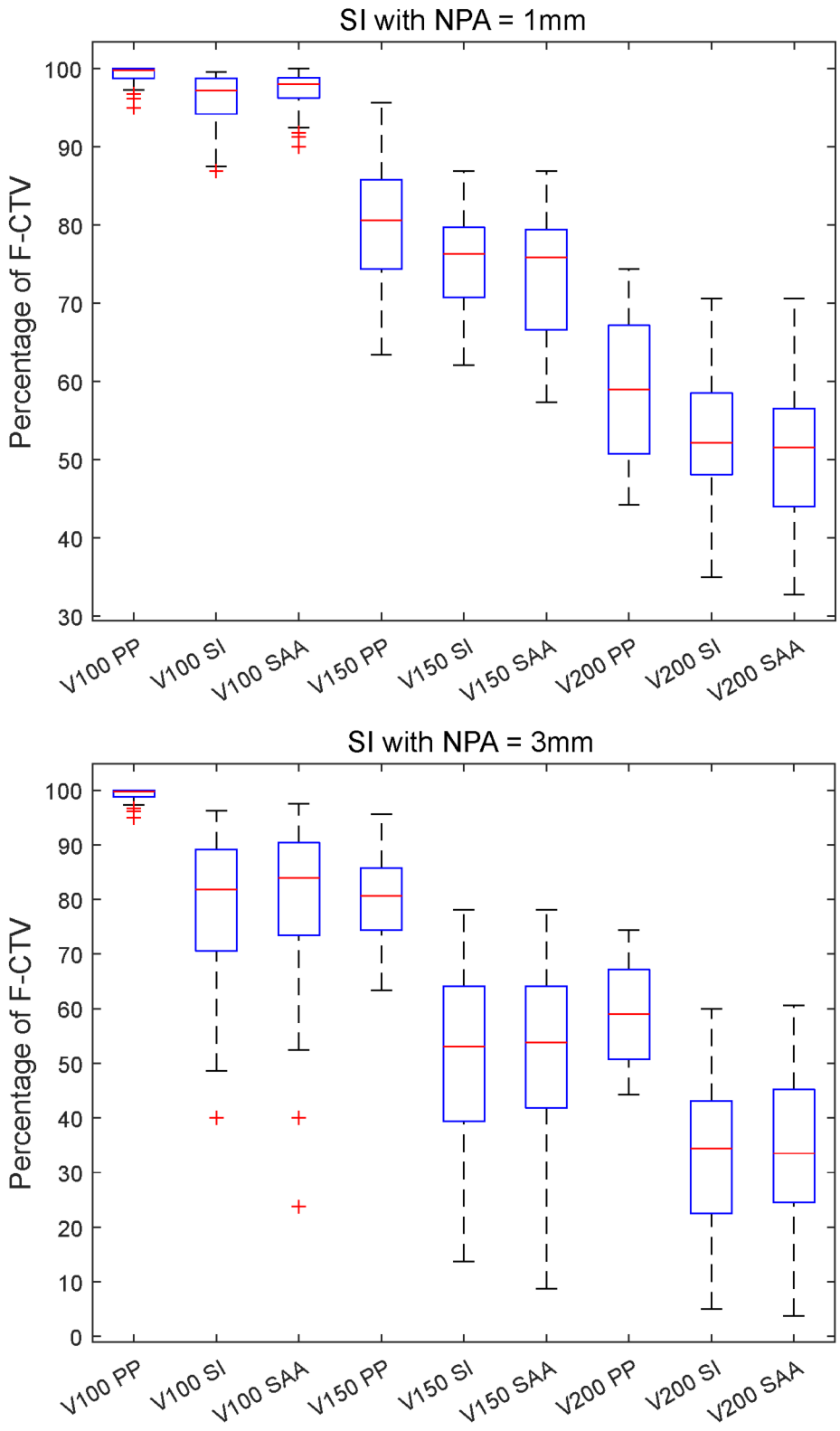

Figure 24: Bars and whisker plots of the V100, V150 and V200 of the F-CTVs 1/3/4/5. The ten pre-plans (PP) of each F-CTV were simulated implanted (SI) without and with simulated annealing adaption (SAA).The NPA for the needle tip is 1 mm (up) and 3 mm respectively (down).

implant.

For an NPA of 1 mm the post treatment V100 was close to the range of the pre-planned values with V100 = 97.1 ± 2.5 %. The SI without any adaption resulted in a post treatment V100 of V100 = 96.1 ± 3.3 %. The V150 and V200 dropped for SI either with or without SAA against the pre-plans as the inter-seed distance is statistically increasing and the dose distribution is smeared out. This effect increases with a lower NPA of 3 mm. The same effects were seen for constant deviations of 2 mm in Figure 25. Therefore, the post treatment V100 benefits from SAA independently of statistically random needle displacement given with the NPAs as normally distributed deviations.

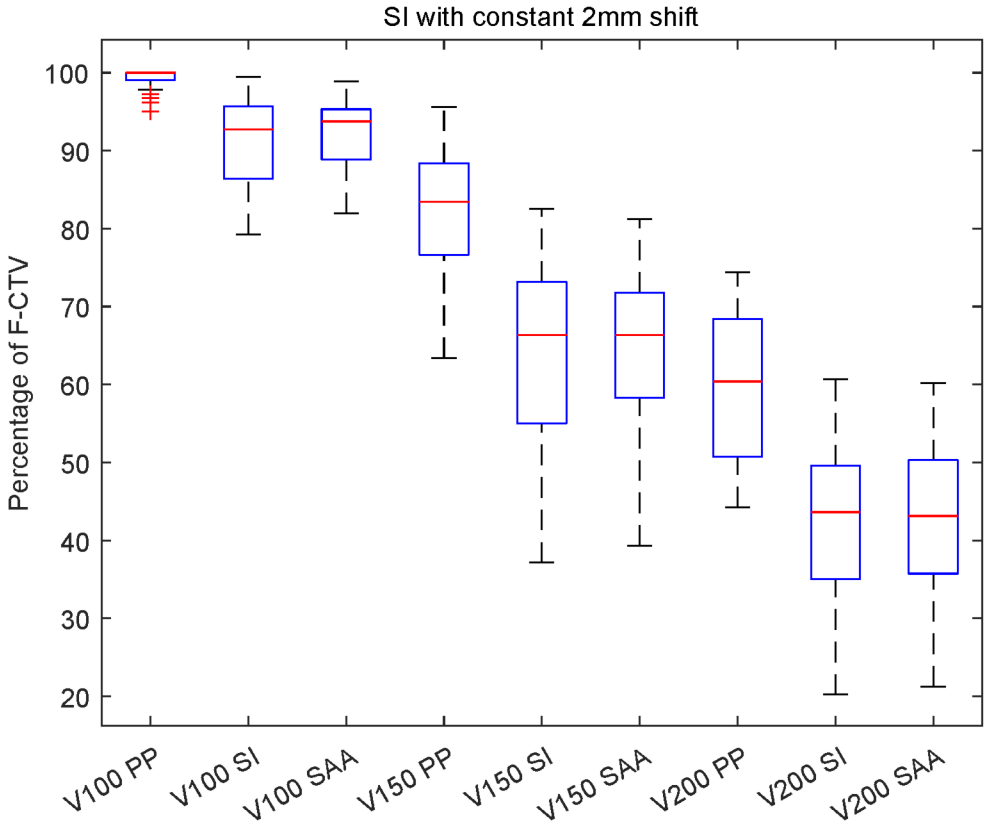

Figure 25: Bars and whisker plots of the V100, V150 and V200 of the F-CTVs of L1/3/4/5. The 10 pre-plans (PP) of each F-CTV were simulated implanted (SI) without and with simulated annealing adaption (SAA) by adding a constant shift of 2 mm to the needle tip.

Lesion L2 was excluded in the graph as the pre-plan V100 reached only V100 = 93.9 ± 4.5 % and in the SI needles sometimes punctured the urethra. The SAA algorithm then dismissed the helping points inside of the urethra which led to a safer implant but on the other side a worsened V100 value of 82 % against 92 % of the SI. Lesion L2 was therefore not reasonably reachable by this setup.

Figure 26 on page 57 shows the V100 of ten plans for each lesion L1/3/4/5 in the pre-plan, simulated implantation and SAA. F-CTV #3 showed the best results of the

F-CTV (#)	size (ml)	needles	25/75th percentile	seeds	25/75th percentile
1	0.6	3	(3-4)	5	(5-6)
3	1.3	5	(5)	7	(7)
4	1.5	6	(5-6)	7	(7-8)
5	1.7	7	(6-7)	8	(8)

Table 9: The table shows the F-CTVs' size and used number of needles and seeds.

pre-plans with a median V100 = 100 % but with one outlier of 95 %. The lowest median V100 had #4 with V100 = 98.6 % and with a 25th percentile of 97.3 %. By comparing the results of each lesion in terms of the simulated implantations, it is worth analysing the size of the F-CTVs and the used number of needles and seeds. The latter is displayed in Table 9 on page 56. The number of used needles raised with the F-CTV volume from the smallest F-CTV #1 with three needles to the largest F-CTV #5 with seven needles. The simulated implant showed the trend that the higher number of needles resulted in less loss of the V100. Comparing the SAA statistics one can see an improvement to the simulated implant. Especially the 25th percentiles were higher and the outliers were reduced. By correcting the dose distribution and the V100 after a failed needle implantation, the implantation success was more stable.

3.5 Transrectal implantation experiment

In the phantom experiment, two needles with two dummy seeds and two Sirius spacers were implanted. The robot was navigated to direct centrally to the lesion displayed in Figure 4 on page 13. The latter was located at the F-CTV #1 from the planning studies and was contoured with a 1 mm margin as the target F-CTV with 1.3 ml size to be treated by the prescription dose D_{pr} = 160 Gy as the covering isodose envelope.

The workflow described in section 2.7 was followed. Therefore, an inverse treatment plan with five needles and seven seeds was planned. For both needles the needle insertion depth optimizer did not alter the insertion depth. The V100 in the pre-plan and after the needle guide registration were V100 = 100 %. After the first needle implantation the seeds were registered in the MRI images and the online dose distribution was calculated. The V100 dropped to 98.26 % and the SAA algorithm was used to optimize the remaining needles. However, the V100 remained constant. Then this procedure was repeated with the second needle to complete the whole workflow cycle once.

With the MRI to CT matched evaluation, the V100 dropped to V100 = 95.35 % after the first implanted needle and to 91.86 % after the second one. Here the dose distribution was calculated by the sum of the remaining needles of the pre-plan and the implanted seeds. The SAA algorithm would have been able to adapt the remaining needles after the first needle from V100 = 95.35 % to 99.42 % by two optimization executions and after the second needle from 91.86 % to 93.60 %.

The Table 10 on page 58 shows the resulting spatial deviation of each seed respectively. The deviation from the initially pre-planned to approved seed coordinates (In./

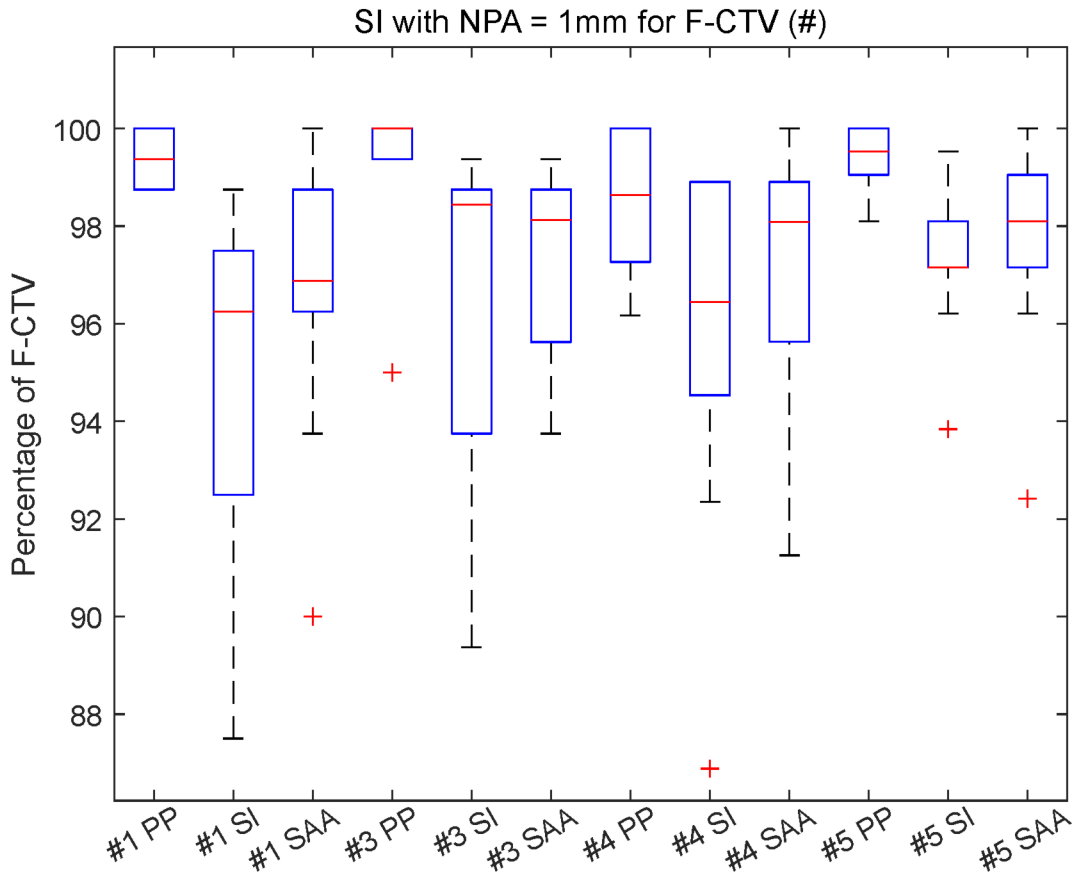

Figure 26: Bars and whisker plots of the V100 of each F-CTV #1 and #(2-5) for the preplan (PP) after the simulated implantation (SI) and with simulated annealing adaption (SAA). The NPA for the needle tip is 1 mm.

App.) was 0.58 ± 0.22 mm. This deviation is attributed to the deviations resulting by choosing the needle tip coordinate aim in the image set with the computer mouse and the movement by the RCM. A low slice thickness was required to enable choosing the closest coordinate to the pre-planned one. The seed coordinates deviation from MRI only to the MRI-CT matched data sets (MRI/ MRI+CT) was 2.78 ± 1.43 mm resulting from the different seed registration accuracies. In the MRI, the seed registration was difficult due to artifacts from magnetic field distortion around the seed. The seed registrations for the seeds #s1 and #s2 of the first needle were quite close with 1.21 mm and 1.86 mm. For seed #2 of the second needle, the seed registration failed with 5.00 mm spatial deviation.

Figure 27 on page 59 shows a registered seed in the matched MRI-CT image. The deviations of initially planned and approved seed coordinates to the MRI-CT matched data set were 2.63 ± 0.87 mm and 2.62 ± 1.24 mm respectively depending on the accuracy of needle placement and seed release.

#N	#S	Δ(In./App.) (mm)	Δ(In./MRI) (mm)	Δ(In./MR+CT) (mm)	Δ(App./MR+CT) (mm)	Δ(App./MRI) (mm)	Δ(MR/MR+CT) (mm)
1	1	0.36	3.66	3.15	3.11	3.53	1.21
1	2	0.40	3.08	2.49	2.74	3.12	1.86
2	1	0.67	4.07	3.61	4.02	4.01	3.06
2	2	0.91	5.61	1.29	0.63	5.55	5.00
		0.58 ± 0.22	4.11 ± 0.87	2.63 ± 0.87	2.62 ± 1.24	4.05 ± 0.92	2.78 ± 1.43

Table 10: The spatial deviation of each seed #S of the #Nth needle with the first seed located nearest to the needle tip. In: Initially planned seed coordinate. App.: Seed coordinate after recalibrating the needle guide and approving the trajectory. MRI: Seed coordinate derived from the MRI images. MR+CT: Seed coordinate derived from the matched CT to MRI image.

#N	#S	Δ(In./App.) (mm)	Δ(In./MRI) (mm)	Δ(App./MRI) (mm)	Δ(In./MR+CT) (mm)	Δ(App./MR+CT) (mm)
1	1	+0.31	-0.98	-1.17	+0.98	+0.72
1	2	+0.32	+0.93	+0.71	-0.02	-0.30
2	1	+0.43	+3.42	+3.06	+0.66	+0.35
2	2	+0.44	+5.27	+4.90	+1.06	+0.62
		0.38 ± 0.06	2.16 ± 2.38	$1.88 \pm 2,30$	0.67 ± 0.43	0.35 ± 0.40

Table 11: The depth deviations of each seed #S of the #Nth needle. In: Initially planned seed coordinate. App.: Seed coordinate after recalibrating the needle guide and approving the trajectory. MRI: Seed coordinate derived from the MRI images. MR+CT: Seed coordinate derived from the matched CT to MRI image. A positive value signifies a deviation directed into the patient.

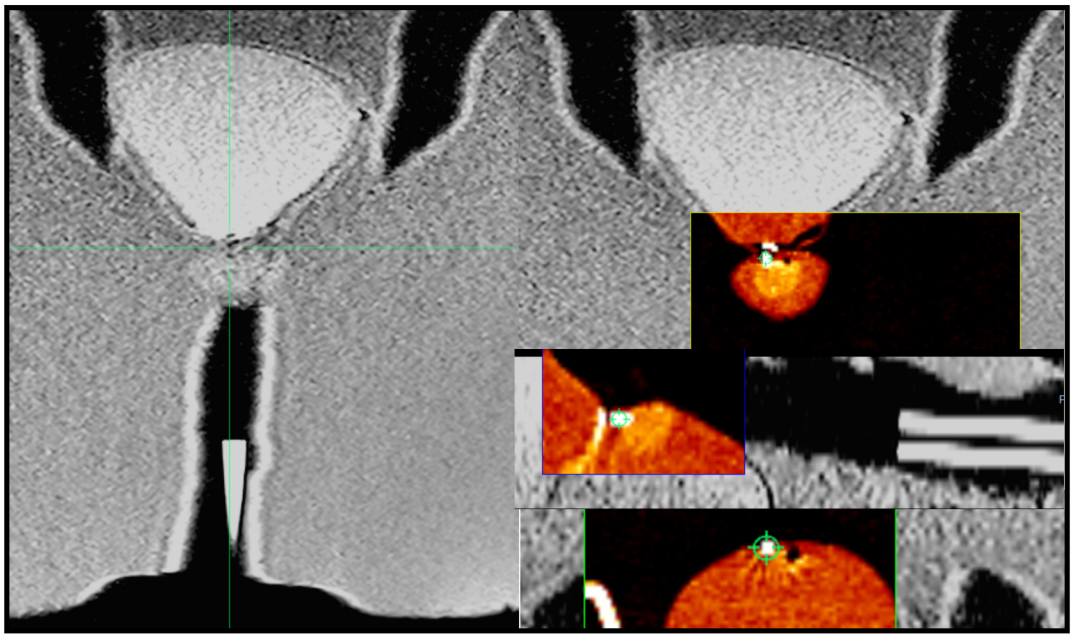

Figure 27: The image registration between MRI and CT is shown. Left: The transversal image with the green lines marking the registered seed. Right: The overlay of the CT images in the transversal (up), sagittal (mid) and coronal (down) directions with the green cross pointing the clearly visible seed.

Table 11 on page 58 shows the analysed depth deviations. The results for IN./App. show that the approved seed coordinates are located 0.38 ± 0.06 mm deeper in the patient. This depends on the insertion depth measured from the approved needle guide tip to the target point that is slightly longer than the initial insertion depth. The needle depth deviations of the approved seed coordinates were closer to the CT registered seeds than the initial seed coordinates (App/MRI+CT to In./MRI+CT). This effect was not visible for the spatial deviations. It could be explained with needle bending as the bevelled tip was directed into the direction of the initially planned needle trajectory. The results of the seed registration on the MRI images shows that the spatial deviation of #S2 of #N2 of 5.55 mm was close to the needle depth deviation with 4.90 mm. It should be noted that the needle depth deviation can only be calculated for one coordinate point and one trajectory. Therefore, a direct comparison between the MRI and MRI+CT seed registration is not possible, as these are two coordinate points and the trajectory is missing.

4 Discussion

4.1 Dose modelling of Iodine-125 seeds

The two dose planes by OCP and the TPS were comparable with small differences in the close vicinity of the seeds and far-off the seeds. The failed pixels in close distance with d < 0.25 mm to the seeds have a dose difference of D > 1% up to a distance of 1 mm. Here the dose calculation is not delineated by the TG-43 formalism as there is a high uncertainty to the dose rate. In the TG-43 formalism, the latter are only given up to the radius of r = 2.5 mm. In this work the dose is extrapolated to the seed surface for every angle θ to approximate the high dose delivered in the seed's close vicinity. It gives a good idea of the high inhomogeneity of the dose distribution of seed-BT with its low keV radiation in contrast to EBRT prescribed homogeneously. The extrapolation shows higher maximum dose values than OCP where the dose is extrapolated on the lateral side up to 1 mm. From the formula $D_{\Phi_i}(r_{surf}) = a\, r_{surf}^{b}$ it can be seen that D_{Φ_i} is greatest for the smallest distance r_{surf} from the seed centre when the fit parameter b is negative. 26 % of the failed pixels contained higher doses than 500 Gy. In the line plot of Figure 14(c)) the dose maximum of the TPS is 1508 Gy and of OCP 1017 Gy. In clinical practice it is sufficient to know if the dose of one pixel is higher than 200 % of the prescription dose. Than it is considered as part of the V200 which is the only measure for hotspots in the target volume. In the region with 2 mm $\leq r \leq$ 7 mm where the dose was accurately interpolated with the fit functions, the gamma values were near zero indicating a very good agreement of the two planning systems. As can be seen in Figure 8 on page 19 this range is most important for the treatment planning with the therapeutic doses of 200 to 30 Gy. A solely linear interpolation between the tabulated distances of $r = 2.5/5/7.5$ mm would lead to an overestimation of the dose in distances of $r = 3/4/6/7)$ mm, because the dose gradient is approximately proportional to $\frac{1}{r^2}$ and not linear. Furthermore, deviations can occur due to the manual reconstruction of the needle catheters and seeds in OCP, which would result in slightly shifted seed coordinates. Another source is the transformation of the dose grid from the internal coordinate system of OCP to DICOM coordinates. This can result in small shifts to each dose grid point due to round-off errors when the whole dose grid is shifted to match the DICOM coordinates.

4.2 Path planning

Scenario 1 The path planning is designed to reduce efficiently the number of injection points. This can be done by ordering the filter functions by its effectiveness and excluding failed injection points immediately, because the number of injection points to be tested influences the computational costs. However, the remaining injection points are then tested by more specific filters to find the last invalid injection points. In this way the path planning is mostly time efficient. The first risk structures filter excludes 44, 7 % of all injection points by using the checkpoints calculated with equation 9 on page 21. Because only one point per needle trajectory is tested, invalid trajectories remain puncturing the

risk structure somewhere else along its track. This is especially the case for complex risk structures like the liver that are asymmetrically shaped to their median coordinate. The filter is failing if the median coordinate of the OAR is not inside of its alpha shape. This is possible if the structure is enclosing other structures such as the ribcage as whole structure would. Therefore, these complex structures have to be contoured separately as was done for each rib. To catch invalid trajectories referring to this issue more specific filters based on equation 11 add the spatial standard deviation vector of the shape coordinates to the median coordinate. Each filter uses a different length of this vector $(-2 : 0.1 : 2)$ std. It points towards the room direction with the most outlying shape coordinates. For a spherical structure, the standard deviation would be equal in all room directions with a standard deviation pointing skew e.g. (1,1,1). For the aorta and vena cava e.g. with a cylinder shape along the Y-axis, the standard deviation vector points strongly in the y-axis and skew to x and z similar as in the spherical case for all three dimensions. For normally distributed data, the raster of $-2 : 0.1 : 2$ std includes 95 % of the points. It therefore samples each OAR according to its specific geometry. This approach is more automated than sampling the checkpoints along defined radial distances as e.g $(5 : 0.5 : 5)$ cm. Including the standard deviation ensures choosing checkpoints within the OAR.

Contouring each bone separately is a time consuming task but it could be automated by including novel contouring algorithms [79].

The needle insertion depth is an important parameter with impact on the needle placement accuracy. Due to needle bending shorter insertion depths are preferable. In scenario 1 with a central metastasis, the trajectories with an insertion depth longer than 17.5 cm to the most posterior contour point in the -z direction were rejected. The margin of 2.5 cm should ensure that all contour points of the remaining injection points should be reachable considering slightly longer insertion depths for skew trajectories. However, this depends to some degree on the target volume size and could be insufficient. To generalise this insertion depth filter each side of the target volume should be considered.

Scenario 2-3 For scenario 2 only the urethra is an OAR to be considered in the path planning process. For this planning study, only one injection point being the RCMs rotation point of the needle guide was considered. Therefore, no additional filters were necessary. In scenario 2 the rotation point was set centrally on a needle guide which is positioned with the needle guide on the rectal wall next to the prostate. In Scenario 3, the rotation point was set near to the sphincter with the longest distance to the prostate lesions.

4.3 Needle candidate domain

Scenario 1 The size of the needle candidate domain results from the number of valid injection points and their maximum number of possible seeds as well as the number of contour points being the tip points of the needle candidates. The number of possible seeds depends on the length of the needle trajectories through the target volume. Hence, the size of the needle candidate domain depends on the diameter and surface area of

the target volume. The liver metastasis provided the largest needle candidate domain in contrast to the prostate CTV and the F-CTVs of scenario 1 and 2 respectively. It contains about 1.01 10^6 possible needle trajectories resulting out of 827 injection points and 1971 tip points. The state of the art template based approach for prostate seed-BT however works with 125 parallel injection holes on the template in the local radiotherapy department. This gap of complexity has to be considered for the planning process. From the state of the art approach, one can see that a much smaller amount of needle candidates is sufficient to achieve clinically acceptable plans. For the liver metastasis, there might be a high number of clinically acceptable plans achievable. The structure of the needle candidate domain therefore is designed to enable fast optimization while dealing with a higher complexity. The idea is to pre-process as much information as possible before the optimization takes place and to structure the domain in a way that fast access during the optimization is possible. The structure itself implicitly contains information e.g. number of seeds $(i-1)$ of the domain of injection points in the ith column. Also pre-processed is the information that every possible needle configuration out of the needle candidate domain contains seeds within the target volume.

Scenario 2 In contrast to scenario 1 with OARs around the target volume, here the only OAR to be considered for path planning is the urethra within the target volume. Tip points behind the urethra were filtered out by the OAR filter. The seed positions then are allowed being placed inside of the target volume but outside of the urethra and the urethra margin. This results in needle candidates with trajectories passing the urethra within the urethra margin. However, these only contain needles with one or two seeds in the space between the urethra margin and the prostate contour surface. The caudal space from urethra to rectum could be covered by needle candidates with the needle tip on the urethra margin contour points. However, longer seed strands covered this area as Figure 20 shows. With these needle candidates the domain enables to use needle trajectories with seeds inside of the prostate CTV with a spacing of at least 8 mm margin to the urethra that are able to cover the whole prostate except the space directly hidden behind the urethra. The latter can be better covered with dose by shifting the tip point coordinates 1.5 mm along their trajectory. Then the seed coordinates are located closer to the CTV contour and eventually an additional seed can be placed on the needle candidates between the urethra margin and the prostate contour. Altogether due to this shift all needle pathways through the prostate are extended by 1.5 mm except the ones with the tip points on the urethra margin leading eventually to longer seed strands for some needle candidates.

Scenario 3 The needle candidate domain resulted in a small a set of 33.8 ± 12.6 possible needle trajectories and short needle pathways trough the target volume. With needle tips on the F-CTV's contour points this would have led to needle candidates containing mostly one seed. However, the seed migration for single seeds is a greater issue than for the stranded ones and more needles might be necessary to cover the F-CTV with single seeds. To allow more seeds on the needle trajectories the whole pathway through

the F-CTV is taken into account such that the first seed coordinate can be located on the contour points where the needle tip is assumed initially. This resulted in two to one seeds per needle. In contrast to scenario 2, the needles tips are here not shifted, but there are valid second seeds located outside of the F-CTV. Since the simulated annealing approach varies the needle tip position to optimize the dose coverage this adaption were sufficient. Further, the remove seed algorithm is introduced to detect seeds outside of the F-CTV with little importance to the V100. This is the case when the simulated annealing shifted the needle backwards such that the first seed is placed centrally and the second one outside.

4.4 Treatment plan optimization

In the TPS the optimization algorithms are implemented as functions, which enables to use them in a modular way. This enables the user to analyse each optimization step before starting further optimizations. For each individual target volume, there might be an individual combination necessary for optimal treatment results. The TPS can be compared to the simulated annealing optimizer with OAR sparing in [39] tested on lung adenocarcinoma and a tumour at the spine. In contrast to the automatic needle path planning of this TPS the needle candidates are adjusted manually by the physician. Then the seeds source positions are optimized by the simulated annealing algorithm with a fixed number of seeds, the first defined by a seeds per volume size monogram. The latter is then varied to generate various plans used to generate plan evaluation DVHs. They are then compared to a clinically acceptable reference DVH to determine the optimal number of seeds. Note that the simulated annealing used in this work varies the needle trajectory with fixed seed positions, whereas here it is done the other way round. If a subpart of the CTV is too far distanced to a catheter adjusted by the physician the optimizer has no degree of freedom to cover it efficiently. Therefore, this approach is strongly user dependent. In this TPS the needle path planning and the total number of needles and seeds is part of the inverse optimization process.

Scenario 1 The greedy optimizer loops efficiently through the needle candidate domain to generate the initial treatment plan. To spare time it validates only subsets of the domain to choose the next needle. The theoretical risk of a greedy optimizer is to be trapped in a local minima of the solution space. Then there is no needle candidate left to be placed when the threshold of V100 $> 99\,\%$ is not yet reached. This is the case if a needle is placed in a way that there exists uncovered space not reachable by needles with a single seed. To counteract this behaviour especially the first subsequent needles are only allowed being placed next to the anterior ones by introducing the dose range condition of equation 15 ($\mathrm{DR} = [0.25\ \mathrm{D_{pr}}, 0.7\ \mathrm{D_{pr}} + 3\ \mathrm{N}]$). The next needle candidate's tip such as the seeds have to be placed within the space defined by the dose range. In Figure 13 on page 40 the space between the dose levels $[25, 70]$ Gy resulting by a needle with five seeds can be seen in light blue. On the lateral side it spans more than 3 mm. Therefore, the first needles are placed along the similar direction since their needle tip and stranded seeds only then fit in the dose range space. This can be seen in Figure

18 on page 46 for the needles #1/2/3. This is geared to the state of the art template based approach where only co-planar needles are possible. If no limitations to the OARs are given this is a good strategy to cover the target volume with the prescription dose without generating cold spots in between the needles because of improper spaced seeds.

The first needle is particularly important as the starting point for the next needle candidates allowed being set. Therefore, its needle tip coordinate is the one best reachable by needle candidates with five seeds assuming that the neighbouring possible needle tip coordinate are evenly reachable. The first needle's injection point is the median of the subset of possible injection points. Then the needle trajectory should be positioned centrally enabling enough neighbouring needle candidates to be set.

The dose range condition is important for the success for the optimizer as it limits the sub-set of needle candidates considered next. The volume defined by DR dynamically changes with each needle placed. The upper boundary $0.7\ \mathrm{D_{pr}} + 3\ \mathrm{N}$ limits the valid dose in which the seed and needle tip is to be placed. Because every seed is surrounded by high dose in its vicinity, the inter-seed-distance is influenced by this boundary as well. The lower bound $0.25\ \mathrm{D_{pr}}$ however restricts considering needles with too much distance from the current dose distribution to limit the number of needle candidates for the optimizer and to prevent cold spots between the needles.

The DR volume grows with each needle placed as the seed dose contributes to the dose gird up to 10 cm. With each needle the superimposition of the lower dose contributions of each seed becomes more relevant such that the volumes defined by the boundaries in equation 15 grow towards the target volumes contours. To prevent limiting peripheral needle candidates without having the prescription dose coverage at these regions the dynamic term 3 N is added to the upper boundary. N here is the actual number of needles set by the optimizer. Therefore, the upper bound is steadily increased to allow needles in higher dose regions and therefore with closer distance to the other seeds in the late phase of the optimization. The tenth needle e.g. has an amplified DR of $[25, 100]$ Gy.

The optimizer is structured to choose the needle candidates with the highest number of seeds. At some point there is no needle candidate with this amount of seeds left which fulfils the DR condition. This ensures choosing as much long seed strands as possible before reducing the number of seeds. It is assumed that this approach leads to a minimum number of required needles which results in a faster and less harmful implantation procedure.

From these results it can be seen that the DR has an important influence on the plan parameters such as the final number of needles and seeds and if the optimizer achieves the planning goals. If the lower boundary $0.25\ \mathrm{D_pr}$ is chosen too high the risk to find no needle candidate fulfilling the DR condition rises. Same yields for the upper boundary of $0.7\ \mathrm{D_pr} + 3$ N. Lowering it leads to less remaining space in the uncovered target volume. Therefore, the optimizer reduces the number of seeds faster, which finally results in treatment plans with a higher number of needles with less seeds each. However, for the given DR this was not the case as all of the ten initial treatment plans resulted in a $\mathrm{V100} > 99\,\%$.

The remove-seed algorithm aims to minimize the number of seeds of the initial treatment plan by searching for the seed closest to the medians of the volumes enclosing

200 % and 50 % of the prescription dose (in this context V200 and V50). The V200 is the region with too high dose, which should be minimized by reducing seeds from there. It is apparent in the close vicinity of each seed and is raised by the superimposition of the lower dose contribution by the neighbouring seeds as can be seen in the dose planes of Figure 14 on page 41 (light red contours). The median of the V50 was considered as well to choose a seed that is also well distanced to the low dose region as removing the seed could lead to a loss of the V100. The seed found by this procedure most likely located near of the target volume centre and therefore often one of the inner seeds of the strand. However, only the outer seeds can be removed by shortening the strand by one seed and adapting the needle position. Therefore, the whole seed strand containing the found seed is analysed by the sample coordinates. The sample coordinates of equation 20 are located 5.4 mm from the seed centre. For the first of an isolated five seed strand the dose at these coordinates is around 30 Gy. If their dose exceeds the V200 = 200 Gy they are located in the high dose region resulting by superimposition of nearby seeds. The number of sample coordinates located in the high dose region enables to validate the seed position relative to the high dose region. The higher the number the more dispensable the seed gets. The subtraction of the actual seed number n of the strand in equation 21 on page 28 raises the decision threshold for the inner seeds more likely to be inside of the V200 region e.g. from five to eight for a five seed strand. The outer seed often is located near of the target volume shape where the dose rapidly falls off. Therefore, the dose distribution is actualised after removing one seed and before validating the next seed's sample coordinates. Note that validating only the seed centre coordinate is insufficient as it is always located inside of the V200 due to self-contribution.

The needle-depth optimizer is varied to compensate a loss of the V100 by the remove seeds algorithm. In the optimal case, the better distribution of the seed during the optimization leads to a higher V100 and lower V200 by raising the homogeneity of the implant, because the implanted total dose remains constant. In the optimization example of Figure 17 on page 45 this can be seen by slightly shifts of the V100 up and V150, V200 down due to the needle-depth optimizer (blue background).

If the V100 constraint is not satisfying, the coverage optimizer searches for needle candidates in the under-dosed region of the target volume. Figure 17 however shows that these last seeds also raise the V200 due to more distant dose contributions to the target volume centre. Therefore, the needle is only placed if each seed contributes at least 0.5 % to the V100 in the condition 23 on page 30.

The statistical results displayed in Figure 19 on page 47 show that the treatment aim of a good coverage with the V100 = (99.1 ± 0.3) % is achieved in all ten cases with a very small standard deviation. The D90 = 125.9 ± 3.6 Gy is greater than 110 % D_{pr} = 110 Gy. As each plan achieved these constraints there is no need to generate multiple treatment plans for treatment planning as one might expect because if the risk of a trapped greedy optimizer. However, the treatment plans show variations in the V200 = (44.5 ± 5.5) % which can be attributed to the remove-seed algorithm where the decision of seed removal depends on the sample coordinates condition of equation 21. If the outer seed is considered too important to remove, the remove seed algorithm exits which finally may lead to a higher V200 and a higher seed number. The seed number varies only with

a standard deviation of 0.8 seeds. It can be noted that the secondary optimization by the remove seeds and coverage algorithms in total enables to remove up to five and add up to two seeds. Here there were removed three seeds in maximum. These algorithms hence diminished the seed variation by converging the plans to the optimal number of seeds.

Scenario 2 The treatment planning to the prostate CTV is equivalent to the state of the art prostate seed-BT in terms of target volume and planning constraints. The difficulty lies in sparing the urethra with the constraints D10(urethra) $< 1.5\,D_{pr}$ and D30(urethra) $< 1.3\,D_{pr}$ while achieving a V100 $> 95\,\%$. The urethra constraints can be maintained ensuring enough distance for seeds to the urethra as the seed deposits high dose in its close vicinity. However, as can be seen in Figure 20 on page 49 the fan-shaped geometry of the needle trajectories leads to many needle candidates with seed positions near to the urethra. Especially the caudal space from the urethra, the anterior fibromuscular stroma, can only be covered by these needle candidates. However, in the state of the art prostate seed-BT the latter is hard to be covered as well because of the urethra alignment.

This problem is solved by introducing an eight-millimeter urethra margin and adjusting the needle candidate domain. Needle trajectories pass the urethra margin enabling to cover the space behind the urethra with seeds while the urethra margin remains free of seeds. This important optimization information is pre-processed in the needle candidate domain minimizing the computational cost due to invalid solutions.

In contrast to scenario 1 the first needle cannot be placed centrally into the prostate due to the urethra. The first needle has the maximum number of possible seeds and is the one that maximizes the volume of equation 17. The latter rewards a large prescription dose volume and penalizes the V200 of the urethra margin. Therefore, the first needle is likely placed centrally of the hemigland with enough distance to the urethra margin.

The first DR in equation 18 is only limited by the upper boundary with $0.1\,D_{pr}$ e.g. ensuring a distance of at least 12 mm from a five seed strand and 145 Gy prescription dose. The greedy optimizer will then most likely choose the second needle candidate from the ones on the contra-lateral hemigland. The objective function then only minimizes the V200 of the urethra margin to ensure that the needle candidate is well distanced to the urethra. For the next needles the greedy optimizer will then choose needles with the maximum number of seeds which are distanced to the urethra margin and fulfill the second DR condition of equation 19 on page 27. Interestingly there is no need to map an incentive to the objective function to reach the V100 $> 95\,\%$. After covering the peripheral zones of the CTV, the optimizer is forced to reduce the number of seeds and place needles in the remaining uncovered space behind the urethra margin. As can be seen in Figure 20 a) the needles #16 to #21 contain two or one seed and are placed around the urethra.

It can be seen that the greedy optimizer had to be adapted to achieve the treatment goals. If the first DR (eq. 18) is chosen the same as the second DR (eq. 19) the optimizer would fail at a specific point of the optimization described in the following. Primary

it would set needle candidates with the maximum seed strands on one hemigland. At some point, the dose range has to enable choosing needle candidates with the tip points on the contra-lateral hemigland as well as with seeds coordinates within the dose range. Therefore, the greedy optimizer needs two needles with the maximum strand length to fulfil the treatment aims.

In Figure 20 it can as well be seen that the most needles are placed centrally of one gland. The dose by these needles containing long seed strands often is sufficient to spread the prescription dose's isodose line beyond the CTV contours. Therefore, more urethra sparing might be possible if there are more needles set near of the CTV contours. The reason for this behaviour is that the optimizer implicitly prefers strands with the maximum number of seeds. The more peripheral needle candidates contain less seeds due to the shorter path length through the CTV. Hence, the better treatment plan result is only achievable by using more needles with shorter seed strands. However, in the transrektal use case the number of needles puncturing the rectal wall is an important factor to minimize. In addition, the higher stability the longer the seed strand in terms of seed migration is to be considered by the physician.

The fan-shaped planning approach was also discussed by Van den Bosch et al. [80]. The idea was to implant needles with one or two rotation points just beneath the perineum skin using a robot to implant and retract the needle. The paper concluded that the fan shaped needle configuration reaches equal planning results. However, the in-house TPS used in their work allows needles with two spacers or two seeds in a row. Hence, a seed-spacer-spacer-seed strand can be used near the urethra to cover the space in front and behind the urethra to reach the planning goals. Interestingly seed placement around the urethra was solved differently in the transrektal approach of scenario 2. The area behind the urethra is covered by needles containing one to two seeds as explained before. The space in front of the urethra could be covered by needles with the tip on the urethra margin likewise to the planning of the given paper. However, due to the rotation point chosen quite closely to the prostate the density of needle trajectories is higher in front of the urethra than it is in the case of the perineal rotation point (compare fig. 20 a)). Therefore, the optimizer covers this space by long seed strands of the peripheral needles instead of referring to the needle candidates pointing on the urethra contour. The planning results are very close to the ones by this thesis comparing their results with $D_{pr} = 144\,\text{Gy}$ with V100(CTV) $= 96 \pm 1\,\%$, D10(urethra) $= 193 \pm 2,\text{Gy}$ and D30(urethra) $= 187 \pm x\,\text{Gy}$ ($x < 0.5$) for a single rotation point and 3 mm seed spacing. The results of the ten treatment plans of scenario 2 are given in Table 6. They yielded V100 $= 95.8 \pm 0.5\,\%$, D10 $= 194.6 \pm 5.6\,\text{Gy}$, D30 $= 185.5 \pm 5.1\,\text{Gy}$ respectively. However, the V150 $= 50 \pm x\,\text{Gy}$ was markedly lower than in the thesis with V150 $= 64.6 \pm 3.1\,\text{Gy}$. Comparing the rectal doses reveals a better rectal wall sparing by scenario 2. The paper reports D2cc $= 117 \pm 9\,\text{Gy}$ and $D_{0.1\,\text{cc}} = 155 \pm 11\,\text{Gy}$ versus D2cc $= 69.1 \pm 2.3\,\text{Gy}$ and $D_{0.1\,\text{cc}} = 126.6 \pm 11.4\,\text{Gy}$ respectively. This could be explained by the different seed orientations. In scenario 2 the seeds' longitudinal axes are pointing on the rectal wall with a much steeper dose gradient than seeds aligned with their lateral axes to the rectal wall as is the case for the transperineal approach (compare Fig. 8 on page 19).

Scenario 3 The greedy optimizer is used to generate an initial treatment plan with a high V100 coverage. However, in Figure 21 on page 50 it can be seen that only one of the four optimizations reached the stopping criteria of V100 > 97 %. The other three times the optimizer stopped, because no remaining needle candidate fulfilled the dose range criteria. This is no problem as the needle trajectory and hence the seed positions are another time optimized by the simulated annealing algorithm. It has to be noted that the inter-seed distance in these cases is shorter due to the higher prescription dose of $D_{pr} = 160\,Gy$. The simulated annealing optimization by adapting each needle alone is a time consuming technique, which is only acceptable in this scenario where the number of needles ranges from three to seven needles. Nonetheless, the results match the required treatment goals of a near to 100 % prescription dose coverage and very low OAR doses.

The needle candidate domain in scenario 3 allows longer pathways through the F-CTV. This can result in seed positions outside of the F-CTV after the optimization when the other seed is located centrally in the F-CTV. Therefore, the remove outer seed function was designed to detect the seeds contributing with minor importance to the F-CTV dose coverage. The optimizers were designed to produce plans containing a high V100 coverage of the F-CTV to ensure a good robustness to seed displacement, which is a greater issue for treatment plans with a small number of needles and seeds.

4.5 In-vivo seed displacement adaption

The needle placement accuracy (NPA) is modelled by the simulated implantations (SIs) for the following reasons. The treatment plan stability can be analysed by involving a given needle placement uncertainty which results in a different post treatment dose distribution. This gives information on the stability of given constraints such as OAR sparing and the V100. Secondly the impact of an improved NPA can be shown by these simulations. Thirdly, new strategies for in-vivo treatment plan adaption can be explored and tested.

The basic idea of the adaption strategy is to compensate the loss of the V100 coverage by re-ordering the remaining needles. The next needle is then located on a preferable position and it is assumed that this is the case as well for the area around. Then its displacement results statistically in a smaller loss of coverage. This is only the case when the position and its area around the optimized needle is better suited than it is around the pre-planned needle.

Scenario 1 The seed displacement adaption in scenario 1 aimed at reducing the aorta D1 dose during the implantation process while not violating the other constraints. The latter is the highest dose received by 1 % of the aorta volume. The aorta can be viewed as a serial OAR such that one might minimize the risk of puncturing it with the needle or causing damage to the aortic wall by an overshooting maximum dose. Figure 22 a) on page 51 shows the needle configuration of the treatment plan before the SI. The lowest needle near the aorta containing a three seed strand is the one relevantly contributing to the maximum dose. Therefore, one would expect the optimizer to shift this needle away from the aorta while adapting the other needles to compensate the V100 loss. In

Figure 22 b) the SAA optimizer shows this behaviour by shifting the needle three times up and one time back.

Scenario 2 For the prostate CTV a new greedy adaption optimizer was presented. In contrast to SAA, only the needle that is to be implanted next is adapted. In addition, the domain of the next possible needle tip coordinates is discrete which leads to less computation time. The computational cost of the SAA algorithm in contrast raises with the number of needles leading to too long optimization times.

The simulated implantation results however show that the greedy adaption can be omitted when the seed displacement is small like it is the case with the NPA of 1 mm. Also the results for the 3 mm are clinically acceptable. However, the greedy adaption algorithm shows almost the same dose coverage but markedly better urethra and rectum dose sparing. In practice, the seed registration and adaption would be helpful but should be automated in a way that it is worth the effort. For the prescription dose of 115 Gy the same trends are visible. For the NPA of 3 mm again the post treatment constraints in the greedy adaption approach have got much smaller standard deviations because the needle adaption corrects loss in the dose constraints caused by seed displacements.

Another way of adaption in the combined therapy with 115 Gy and 40 Gy of EBRT could be incorporating the seed dose in the EBRT TPS to allow under-dosage around urethra hot-spots. In practice, this seems infeasible when considering the inter- and intra-fraction movement of the prostate.

Scenario 3 The statistical error of NPA and its accompanied seed displacements result generally in a smearing out of the dose distribution because the inter-seed distance is increasing with more peripherally displaced seeds. This results in a higher coverage loss in small lesions with a small number of needles as for the prostate CTV in scenario 2. In the latter, the statistical displacement error corrects itself on average due to a high number of needles and a displacement error that is small against the CTV size. For small targets it could be necessary to actively adapt the treatment plan for given needle and seed displacements. Therefore, the simulated annealing adaption was compared to a not adapted simulated implantation.

It can be seen that small adjustments of the needle trajectories lead to an improved dose distribution with a higher F-CTV's V100 median. The seed displacement can result in a dose falloff inside the F-CTV at the initially planned position. The latter can be covered by shifting the upcoming needles in its direction with the SAA algorithm. Especially for F-CTV #1 the variation of the V100 is the highest for the SIs as displayed in Figure 26 on page 57. However, by adapting just the two remaining needles the number of plans failing the V100 $> 95\,\%$ constraint is reduced. This can be seen as well for the F-CTVs #3 and #4. Also for the largest F-CTV #5 with 1.7 ml size and eight needles an optimization effect is clearly visible.

This optimization effect is visible as well in Figure 24 on page 54 for both NPAs of 1 mm and 3 mm. However, for a NPA = 1 mm it is more distinct. Here more V100 values were over 95 % than for the SIs. A perturbation of a needle shift about 1 mm can be

compensated by the SAA algorithm with needle optimization shifts of at the maximum ±1.5 mm in each room direction. For a NPA of 3 mm these adaptation shifts are small in comparison to the perturbation factor. The constant shift of 2 mm is somewhere in between these two NPAs. The latter cannot be compensated totally with SAA shifts of at the maximum ±1.5 mm. Moreover, each needle is placed with the given shift and the optimizer can only compensate the coverage loss with the remaining needles. The less needles remain the less impact this strategy has on the dose constraints. Nonetheless a specific benefit in the mean of the V100 as well as for the lower whisker and 25^{th} percentile can be observed.

The adaptation strategy is generally only possible if the initial plan contains a high coverage with enough seeds, otherwise the seeds cannot be shifted without lowering the V100 at another place immediately. In Figure 24 it can be seen how the V200 in comparison to the pre-plan is lowered due to a reformation of the dose distribution.

The implanted seed coordinates resulted from the simulated needle shift and are assumed to be known. Next to the optimizer, effective seed registration is necessary to realize such an adapted implantation workflow. It has to be noted that such a seed registration also yields a specific uncertainty depending on the image modality used. Alternatively, the needle prior to the seed release can be registered. Then the uncertainty given by the seed release is neglected. On the other hand, the needle position can be validated and re-positioned if necessary. The latter is done in state of the art seed-BT as well.

4.6 Transrectal implantation experiment

The phantom experiment demonstrated the feasibility of the workflow and the accuracy of each step. From the simulations, it follows that only a highly adaptive workflow fully exploits the potential of this implantation technique. One example is the needle guide registration, which has to be done in an adaptive manner.

For the inverse adaptive treatment planning it is necessary to define an injection point for the needle trajectories but in this setup the rotation point coordinate is not remaining totally constant during the whole procedure. The needle guiding might result in changing the insertion depth of the needle guide or a shift introduced due to patient movement or pressure from the rectum wall. Therefore, the needle guide has either way registered just before the implantation with high resolution MR imaging. Then the actual needle trajectory can be recalculated with the new calibrated rotation point and the needle guide tip point coordinate extracted from the image set. The insertion depth can be adapted automatically if needed and the physician has to approve the needle or try to rearrange the needle guide.

The needle guide could be steered accurate enough such that the approved trajectories resulted in sub-millimetre seed displacements. A good strategy would be to allow higher displacements and a fast workflow only for the first needles as long as the algorithm is able to adapt seed displacements. The adaption is not possible for the last needle such that here a precise needle guide positioning is crucial for a successful treatment outcome. This can be done by fine-tuning the robot movement manually and repetitive

MR-imaging.

The seed displacement of the approved and pre-planned seed positions to the registered ones by CT imaging showed an accuracy, which is a little bit better than it is assumed of the state of the art approach. However, there sure is place for improvement. Firstly, I implanted the needles and released the seeds as an untrained user. Implanting the needle about the right depth and releasing the seeds are uncertainties that can be attributed to the physician's skill. These uncertainties are related to the needle depth deviation that were 0.35 ± 0.40 mm. As it can be seen, the user dependend uncertainty is quite small even for an untrained user. The short needle path-length might simplify this task in comparison to the state of the art prostate seed-BT. Secondly, the used 18 gauge needles had a little bit too much clearance inside the needle guide and their bevel tip caused needle displacement due to needle bending as well. The backward stranded seeds were displaced less than the forward ones because of needle bending, which can be seen in Table 10 on page 58. To adapt to the latter the needles' bevel tips were turned in a way that the needles bended into the direction of the initial needle tip coordinate. This resulted in a smaller seed displacement for the first seed of the second needle of the pre-planned coordinate of 3.6 mm against the approved one of 4.1 mm. Here the use of a symmetrically shaped more stable needle could improve the accuracy. Another possibility however would be using bevel-tipped MR-safe needles for in-bore implantations and live imaging to enable needle steering. However, for this possibility it remains to be explored if needle steering is necessary on these small path-lengths and given an accurate needle guide movement.

The approved and initially planned seed coordinates should deviate only slightly as the treatment planning is based on the initial seed coordinates. The registered seeds depth deviation along their needle trajectories in the MRI and MRI+CT images in Table 11 deviate more to the initially planned seed coordinates (In./MRI and In./MR+CT) than to the approved ones (app./MRI and app./MR+CT) (2.16 ± 2.38 and 0.67 ± 0.43 vs. 1.88 ± 2.30 and 0.35 ± 0.40) and the difference of the mean values between (IN./MRI to App./MRI and In./MR+CT to App./MR+CT) is in the same order than the (IN./App.) deviation as one would expect.

This effect on the other side is not visible in the spatial deviations in Table 10 on page 58. Here the median values of (IN./MRI to App./MRI and In./MR+CT to App./MR+CT) are very close to each other. The deviation of (In./App.) of 0.58 ± 0.22 mm has no influence to this deviation. The latter uncertainty is apparently small to the greater uncertainties by needle bending and the clearance inside of the needle guide.

Combining the results of Table 10 and 11 one can analyse if the seed deviates more into the needle depth or laterally. The needle depth depends more on the physicians needle feed and only little of needle bending. The spatial deviation in contrast depends on needle bending as well as needle feed. However, if the depth deviation is small than the spatial deviation error can be attributed to a lateral deviation mainly due to needle bending. By comparing (App./MR+CT) of both measures one can see that the seeds 1, 2 and 3 have small depth deviations but higher spatial deviations due to needle bending. The latter is the smallest for seed #S2 that is the second backward seed of needle #N1. However, the spatial deviation of seed #s4 (0.63 mm) can be attributed to a dominant

deviation along the needle trajectory with a needle depth deviation of 0.62 mm. This seed was placed too far into the patient. Technically this can happen it the user pushes the inner part of the needle during the seed release. The inner part of the needle however must remain on its position while the outer needle is pushed back such that the seeds are released on their correct position. This process requires some training and in the phantom the pressure of the gelatine on the outer needle made this task challenging.

The seed registration with MR-only to CT can be attributed to uncertainties introduced by the manual image registration, the manual seed registration on CT and on MR-only. The accuracy was in the range of the seed displacement after the implantation. Several improvements have to be made to enhance the accuracy of seed registration for a real adaptive workflow.

Vertical MR-images to the stitch canal are the most appropriate to register the seeds. Then one seed could be seen in up to four images and by scrolling through the images, one could get a feeling of the alignment of the unconnected strand. Even though the c4 spacers could not be seen appropriately, they did not result in image artefacts or showed a signal void. Their MRI signal has to be quite near of the gelatine material of the phantom. After all the spacers could not be confused with the seeds fulfilling their purpose in this experiment. In the case of vertical MR-images the seed's long side often is vertically to the image data which facilitates to measure them with e.g. slices of 1 mm thickness. For the first needle implanted the deviation of MR-only images from other directions were 2.0 and 12.5 mm and was corrected with the analysis of this approach to 1.2 and 1.9 mm. Optimizing the MR-protocols is another task to improve the registration outcome.

4.7 Limitations and clinical feasibility

Scenario 1 The TPS is principally independent of the tumour site in contrast to the state of the art seed prostate-BT. With the robotic navigation system, it is possible to plan and treat other tumour sites than liver metastases as well. Other treatment examples could be tumours in the abdomen, head and neck and thorax. However, one might have to adapt the optimization parameters and analyze the generation of the candidate needle domain. The TPS performance for these cases remains unknown. Practically one would generate for each tumour site a specific template to generously deal with the OARs corresponding to a well-defined standard operation procedure.

The prescription dose influences the greedy optimizer in equation 15. Therefore, this part is optimized and tested for prescription doses of $D_{pr} = (100 - 160)\,Gy$. The dose envelopes $0.25\,D_{pr}$ are more distanced to the $0.7\,D_{pr}$ envelope for a decreasing prescription dose because of the rapid dose falloff. Hence the number of needle candidates fulfilling this condition increases which influences the optimizer's performance.

The size of the candidate needle domain depends on the reachability of the tumour volume as well as the CTV size. The former depends on the number of risk structures surrounding the CTV. A high number of risk structures leads to a small candidate needle domain and the optimizer has fewer possibilities for the inverse dose planning. The risk for the greedy optimizer to be trapped in a local minimum raises. If the number of

injection points is too small it could be raised by allowing injection points that are only able to reach specific parts of the CTV during the path planning. For scenario 1, this might as well be the case for a real patient if additional OARs such as the pancreas and stomach are defined. Then plenty of the lateral injection points might be filtered out during the path planning.

The insertion depth has an influence on the needle bending effect and therefore should be as short as possible. In this path planner no needle candidate was filtered out by the insertion depth filter defined by the maximum insertion depth of 18.5 cm. Therefore, the candidate needles chosen first had the longest path length through the CTV allowing five seed strand needles from the lateral side. This makes sense in asymmetrically shaped CTVs where the optimally seed strand placement is more important than a slightly longer insertion depth. This optimizing strategy therefore focuses on minimizing the number of needles used to reduce the patient's injury as well as reducing the implantation time. However, if the CTV were more spherical it would make sense to favour needle candidates with the shortest pathway leading to a higher implantation accuracy. This could be implemented by introducing the needle insertion depth as a planning constrain during the optimization or by filtering out needle candidates with long insertion depths during the path planning. The latter is a hard constraint leading to less needle candidates for the optimization. One would need to adjust the allowed insertion depth if the optimizer fails to achieve the planning goals. Practically one could estimate it in the CT images from the preferred direction, especially when the tumour is located near the skin.

However, currently the seed implantation to non-prostatic cancer is lacking clinical studies. The latter have to show a benefit of treating the tumour or metastasis with the seed implantation. The research funding project associated to this thesis aims to treat patients in the oligometastatic state defined as a patient with at the maximum 3-5 diagnosed metastases [81]. However, treating all metastatic sites in an focal approach could show a survival benefit. This is indicated by two phase II studies using aggressive radiofrequency tumour ablation for unresectable liver metastasis [82] or stereotactic ablative radiotherapy with mixed sites such as breast, lung, colorectum and prostate [83].

In the TG-43 report and this thesis, the tissue is approximated as water equivalent. For the prostate and surrounding tissue, this is totally fine. However, for metastasis in the air-filled lung or close to the bone with a higher density as water the dose error is greater. Another dose effect not considered is the inter-seed interaction, which is mainly the presence of surrounding seeds as non-water equivalent objects.

Scenario 2 The planning study was only acquired for one prostate CTV with a specific volume size of V = 49.4 mL. The planning results for smaller or bigger prostate CTVs should not deviate very much, yet they remain to be tested.

The planning outcome depends also on the rotation point. In this thesis, the latter was assumed to be in the middle of a needle guide positioned with its tip close to the urethra. In Figure 20 on page 49 it can be seen that the contoured needle guide however would have to be inserted about one to two centimetres deeper. Placing the needle

guide this way was difficult in the prostate phantom but it is assumed that it is possible by correct patient positioning in the prone position resulting in a closer needle guide position as e.g. the figures 2 and 3 in [54] show. A rotation point in the needle guide's centre results in a symmetrical cone size of a possible needle guide movement to both the prostate and the sphincter. In contrast would the rotation point near the sphincter result in a bigger cone next to the prostate and vice versa to the sphincter. For the optimization, setting a rotation point next to the sphincter is interesting as well. The needle trajectories then fan out in more distance to the prostate, which might reduce the shadow between the urethra unreachable by needle candidates. This fan effect will also restrict the planning from setting the rotation point to near to the prostate, as the unreachable space behind the urethra gets too large to reach the planning constraints. It remains to be tested on the patient if the central rotation point is best suited to reach all parts of the prostate.

Scenario 2 describes a new method on treating state of the art prostate seed-BT. The planning resulted to be clinically acceptable. Therefore, by assuming a successful intervention the long-term outcomes such as local tumour control should be equivalent to that of transperineal prostate seed-BT. However, the feasibility of the whole workflow yet has to be shown in a patient study. The quality of life related outcomes however might also depend on the implantation procedure next to the quality of the implant. Changes to the latter must be observed in a patient study as well. The side effects related with the urethra dose should be equivalent to transperineal seed-BT given that the planning dose constraints match the post implantation ones.

However, a new retrospective study by Hathout et al. correlates not the whole urethra but more the bladder neck D2cc $> 50\,\%\,\mathrm{D_{pr}}$ to acute and late urinary toxicity [84]. Contouring the bladder neck can be done in TRUS and CT when a Foley catheter is present as well as in the MRI scanner due to the soft tissue contrast. Interestingly urinary toxicity was shown to be more common to LDR BT alone instead of the combined therapy [85]. EBRT in general adds a homogenious dose distribution to the urethra and the seed-BT uses less seeds for the reduced $\mathrm{D_{pr}} = 115\,\mathrm{Gy}$. Therefore, these symptoms seem to correlate with high punctual doses to the bladder neck caused by seeds in close proximity defining it as a serial OAR. It seems that a more precise seed implantation technique would enable to better spare small sub-organ structures in prospective studies to minimize side effects to the patient.

For the rectum there are to be expected differences. The planning results showed potentially reduced rectal doses because of the lower dose gradient along the long seed axis pointing to the urethra in this setting as can be seen in Figure 13 on page 40. However, the simulated implants with a NPA of 3 mm revealed two cases of failed rectum dose constraints with seeds placed very near to the rectal wall. Especially the seed placement accuracy regarding the seed release from the needle has to be done precisely. The occurring negative pressure while retracting the needle has to be considered, because a retracted strand will be placed closer to the rectal wall. In addition, seed migration into the rectum might be possible and is therefore of more concern than it is in the transperineal implantation setting. However, in the given treatment plans the dose near the rectum is contributed by long seed strands because the needle tips are near the

prostate contour on the opposite site. These long strands in practice are more stable against outer forces such as the displacement due to negative pressure and have been shown to migrate much less than single seeds [20].

On the other side, the rectal wall is damaged locally by implanting the needles transrectally. The latter could further raise the risk of infections through the rectum. Therefore, in the biopsy studies using the RCM, antibiotic medication was prescribed for five days to minimize the risk of infections such as prostatitis on the day of the biopsy and five days thereafter [54, 55]. Nonetheless one patient developed an urosepsis which could be treated with antibiotics in [55].

Scenario 3 A specific issue of this workflow is the limited transrectal movement of the needle guide. The needle guide movement is designed to rotate around the fixed rotation point chosen during the registration. The RCM is not able to adjust a specific trajectory by automatic movement, which is necessary to not only reach the tip point target but also adjust the correct trajectory to implant the seeds. Further, the chosen rotation point is not constant during the intervention. Consequently, the initial dose planning cannot be followed strictly as trajectories might change. To minimize this effect the patient has to be positioned in an optimal manner and the needle guide should be steered centrally on the lesion to define the rotation point for the initial planning. Ideally, every location is reachable by this rotation point and it changes only minimally when recalibrating the needle guide to recalculate the needle trajectory. As this is not the case, the online plan adaptation to the current needle guide position is important to verify and approve a possible trajectory shift.

The initial dose planning was designed to find robust treatment plans that yielded a $V100 = 99.2 \pm 1.2\,\%$ being the mean of 40 plans of four different F-CTVs. It was seen that the F-CTV L2 above the urethra can only be covered with a lower prescription dose of 115 Gy with still less coverage of $V100 = 93.9 \pm 4.5\,\%$ than the other F-CTVs due to the reduced reachability behind the urethra.

L2 was also planned with two rotation points near the sphincter to enable more trajectories around the urethra. However, this setup yielded no markedly improvements to the V100. The simulated annealing approach during the initial inverse optimization and the adaption in the simulated implants dismissed trajectories puncturing the urethra due to the collision check function. Therefore, the seed displacements cannot be adapted easily, which leads to a worse V100 than without adaption as the needle trajectories tended to move away from the urethra. However, without an adaption the simulated implant often resulted in trajectories puncturing the urethra. In summary the TPS was shown to optimize treatment plans for intra-prostatic target volumes up to 1.8 ml.

The simulated implantations show a potential benefit of needle adaption. Here the limitation is the technical issue of registering the seed positions accurately to have a precise measure of the online dose distribution and to enable its online optimization. An easier approach would be to use the approved trajectories for the feedback while omitting the seed displacement uncertainty. Then the TPS could adapt to these trajectories without the effort of registering the implanted seeds. The disadvantage however is the

given uncertainty to the assumed seed positions and the real implanted ones.

The phantom experiment is solely an approximation to the human anatomy and tissue properties. The stiffness of ballistic gelatine is different from that of rectal tissue. Therefore, the steering inside of the rectum might be different. The phantom could not be positioned in prone position as precise as the patient could in the in-bore biopsies because of lacking flexibility given by e.g. the hip joints. However, the patient storage might be crucial to enable reaching all parts of the prostate.

The target volume for the experiment was the nearest and easiest reachable in the phantom setting with short needle pathways. The needles used for the standard prostate seed-BT are not MR-safe. Hence, the needles had to be implanted outside of the bore without live imaging. Using MR-safe needles could improve the implantation procedure to enable observing the needle movement during implantation with live MR imaging. Then the bevel tip could also be used to steer the needle to the wanted position.

Otherwise, a symmetrically shaped tip could reduce the needle bending effect. The robot navigation software could be modified to enable entering the target DICOM coordinate directly to prevent the uncertainty of choosing the nearest DICOM coordinate in the actual image set.

Further optimization potential for the MRI only seed registration is using optimized imaging protocols to detect the C4 strands and reducing metal artefacts around the seeds. This was shown to be feasible using an endorectal coil for C4 strand imaging by Martin et al. [50]. However, in this setup using an endorectal coil is unpractical, as this would mean switching it with the RCM repeatedly which would require a recalibration and alignment of the RCM's needle guide.

The simulations showed a V100 = $78.9 \pm 15.9\,\%$ for the NPA = 3 mm. In the phantom experiment a seed displacement of 2.62 ± 1.24 mm were achieved such that one can expect an in-vivo V100 in the similar range. A higher implantation accuracy enables a higher V100 = $97.1 \pm 2.5\%$ for the NPA = 1 mm.

Therefore, further work to enhance the needle placement accuracy is beneficial to fulfil the in-vivo dose constraints. Otherwise, the target volume has to be enlarged with a security margin to account this uncertainty with a lower seed displacement effect due to a higher number of needles and seeds.

Scenario 3 shows a new implantation technique for focal seed brachytherapy with automated needle guide movement and adaption strategies. This approach enables using the MRI modality with optimal soft tissue contrast for image guidance and possibilities to adapt the implantation to the given situation for a higher safety and confidence to small F-CTVs. The transrectal needle placement approach benefits from the shortest needle path-length into the prostate in contrast to perineal or trans-gluteal treatment approaches. Needle bending is reduced as well as the need of realigning the needle with additional punctures. In a current review of brachytherapy robots the image guided transrectal approach was therefore concluded safer than the transperineal approach [86].

For a clinical implementation, studies have to show the practicability, time efficiency and accuracy of this intervention in patients. Improvements are necessary to stop the declining use of brachytherapy that can be seen currently. One factor of cost reduction could be the possibility of dispensing the anaesthesia in this setup to spare clinical

manpower during the intervention as this is done currently for transrectal biopsies with the RCM as well [55]. Reducing the number of needles for focal treatment improves the time costs for the use of the MR and personal.

The ultra-focal treatment approach with seeds on the prostate has yet to show a similar therapeutic effect for low risk prostate carcinoma and reduced side effects to justify reducing the target volume to a focal one. Another possibility is reducing the target volume of the combined therapy of EBRT with BT to an F-CTV for the seed boost. This could show the biochemical recurrence free survival benefit of the combined therapy shown in the ASCENDE-RT study against the EBRT only boost [13], while potentially reducing the toxicity to the patients by markedly reduced urethra and rectum constraints. Kishan et al. show a significantly improved distant metastasis free survival over ten years for EBRT with BT boost for high risk prostate carcinoma with Gleason score 9-10 compared to EBRT alone and radical prostatectomy (RP) [87]. 62 % of these boosts were low-dose-rate and 38 % high-dose-rate BT. The overall survival in this study was significantly improved for 7.5 years but was similar to EBRT and RP after ten years. The authors assumed that other-cause mortality aligns the cohorts on the long term.

The dose escalation to the dominant intraprostatic lesion (DIL) as an EBRT, LDR or HDR BT focal boost shows a benefit for five year biochemical recurrence free survival in the review by Feutren and Herrera [88] and the recent FLAME study shows an improvement of 85 % to 92 % of the latter by EBRT dose escalation [89]. However, the low 30 keV radiation of the seeds results in a steep dose gradient in the seeds close vicinity with doses over 300 Gy being ideally suited for such a focal dose escalation to be combined with EBRT.

4.8 Conclusion

The thesis presents an inverse treatment planning system that enables to generate clinically acceptable plans for two robotic systems in three proposed scenarios.

The path planning algorithm identifies all injection points capable to reach the target volume without hitting surrounding risk structures. The needle candidate domain is generated to structure all combinations of needle candidate injection- and tip points and number of seeds. The inverse planning contains a greedy optimizer for the initial treatment plan designed to rapidly generate a treatment plan to cover the target volume with the prescription dose with a good estimate on the number of needles and seeds to be used. The initial solution is then fine-tuned with additional optimization functions to limit the high dose regions and homogenize the dose distribution. The TPS takes all degrees of freedom into account which originate from the new robotic workflows.

In scenario 1, the needle can be injected from multiple directions independent of an injection template as used in the state of the art approach of prostate seed-BT.

The thesis further elaborates a highly flexible and adaptive workflow using the MRI-compatible RCM for transrektal prostate seed-BT. This is important as the limited movement range inside of the rectum might require adapting the pre-planned trajectories to the given situation. However, subsequent MRI-imaging enables to monitor the whole implantation process. This involves measuring precisely the current needle

guide's alignment to update the treatment plan and either approve the needle trajectory or further fine-tune the needle guide. Moreover, implanted seeds can be registered to feed back their displacements enabling adaptive optimization algorithms to compensate loss of dose coverage. The feasibility of the workflow was shown in a phantom test by implanting to needles with two seeds each. The alignment accuracy of the needle guide was submillimetre. However, due to needle bending the seed displacement was not satisfactory considering the high needle guide's alignment accuracy. An improvement can be expected by implanting in-bore with a MRI-safe needle or by using a symmetrically shaped needle tip to prevent needle bending.

Scenario 2 shows prostate seed-BT with the robotic transrectal approach. The treatment planning with these fan-shaped needle trajectories enables clinically acceptable treatment plans.

Scenario 3 highlights as well the possibility to use the RCM for focal treatment approaches on five lesions on different prostate regions. All lesions could be covered with a high escalation dose of $D_{pr} = 160\,Gy$ if not hidden behind the urethra.

Simulated implantations show the treatment plan robustness to seed displacement for two needle placement accuracies. Moreover, a higher robustness to poor post-treatment planning constraints as well as higher mean values of the latter could be shown by using adaptive optimization algorithms for the remaining needles. However, seed registration with CBCT or MRI itself is an object of research.

Further research should focus on automating seed registration on the used image modality such as MRI to take full advantage of the robotic possibilities. Moreover, the seed implantation to a body donator is a more realistic example and could give further insights on patient positioning and possible issues to validate the workflow's feasibility.

5 Summary

Seed-Brachytherapy (BT) is a guideline-conformal therapy for low-risk prostate cancer, which relies on the implantation of small radioactive sources (seeds) by interstitial needle placement. However, due to the complex workflow the number of interventions is declining which leads seed-BT to a niche existence. A learning phase of 20 interventions is required to reach a plateau of constant dose coverage. This learning curve and the lack of proper education programs might further enhance the trend of declining interventions. Introducing robotic navigation assistance tools and better image modalities could improve the intervention procedure in terms of reduced complexity and higher safety while decreasing costs by higher time efficiency. It then enables a broader access of patients with prostate carcinoma and other cancer types.

This thesis focuses on three treatment scenarios. Scenario 1 is the treatment of a liver metastasis with a navigation tool for trans-percutaneous needle implantations. Scenario 2 is the transrectal treatment of prostate seed-BT using a navigation tool for MRI guided needle implantations. Scenario 3 in contrast treats intra-prostatic lesions in a focal treatment approach or as a dose escalation scenario in combination with External-Beam Radiation Therapy.

In this thesis a novel Treatment Planning System (TPS) is presented. It is part of a novel flexible workflow, which integrates the robot as an automated navigation tool to precisely position an injection template on the patient. The physician then injects the needle. The TPS automates the needle path- and treatment planning by inverse optimization. In scenario 1 the path planning algorithm determines all suitable injection points to reach the target volume by circumventing risk structures. In scenario 2 and 3 the rotation point coordinate of the RCM (Remote Control Manipulator, Soteria medical, Arnhem, the Netherlands)) defines the needle trajectories together with the needle tip coordinates.

The needle candidate domain structures all combinations of valid injection points respectively rotation point and tip points as well as the number of seeds contained by the needle candidate. It then benefits the inverse optimization process in terms of computational cost and time efficiency by providing the pre-processed data. A greedy optimizer generates an initial treatment plan, which is further optimized until the planning constraints are fulfilled.

The robotic navigation assistance could further enable in-vivo plan adaptation to compensate needle displacement. Simulated implantations are executed with two assumed needle placement accuracies to evaluate in-vivo adaption algorithms and the stability of the treatment plans to a given implantation accuracy. The workflow's feasibility for the transrectal approach is tested with an implantation experiment using an anthropomorphic pelvis phantom.

The TPS showed a 98.5 % pass rate for the gamma 1%, 1 mm test indicating a nearly equivalent dose distribution as the same plan implemented in the commercial software (Oncentra Prostate v.4.0, Nucletron B.V., subsidiary of Elekta AB, The Netherlands). The path planning automatically avoided needle candidates through the organ at risks (OARs) in scenario 1 such as the ribs and the liver and the urethra in scenario 2.

The treatment plans matched the planning constraints for all scenarios. The V100 of each ten plans (mean ± standard deviation) yielded $(99.1 \pm 0.3)\,\%$ for scenario 1, $(95.8 \pm 0.5)\,\%$ for scenario 2 with $D_{pr,1} = 145\,Gy$ and $(99.2 \pm 1.2)\,\%$ for lesions L1/3/4/5 altogether in scenario 3. In scenario 2 the treatment plans were clinically acceptable fulfilling as well the dose constraints for the urethra D10 = $194.6 \pm 5.6\,Gy$, D30 = $185.5 \pm 5.1\,Gy$ as the rectum $D_{2\,cc} = 69.1 \pm 2.3\,Gy$, $D_{0.1\,cc} = 126.6 \pm 11.4\,Gy$.

The simulated implants (SIs) showed that needle displacements decrease the V100. However, the smaller the uncertainty the closer matched the post treatment planning parameters the pre-planned ones. This decrease could be partly compensated by in-vivo plan adaption which showed beneficial post treatment dose constraints for all three scenarios regardless of the needle placement accuracy (NPA) and the target volume size. In scenario 1, the dose sparing of the aorta was shown by using the simulated annealing adaption algorithm. The D1(aorta) was reduced from 96.98 Gy to $80.44 \pm 4.64\,Gy$ and $83.56 \pm 8.37\,Gy$ for the NPA of 1 mm and 3 mm respectively. In scenario 2, the greedy adaption reduced the risk of violating dose constraints of the OARs such as the urethra and rectum by smaller mean and standard deviation values of the latter. In Scenario 3, the small target volumes required a high NPA to successfully achieve a sufficient V100 coverage. The simulated annealing adaption here as well improved the post-treatment V100 regardless of the small number of needles with $97.1 \pm 2.5\,\%$ against the un-adapted SI with $96.1 \pm 3.3\,\%$.

The proposed transrectal intervention workflow for scenario 2 and 3 was tested by an experimental seed implantation to an anthropomorphic pelvis phantom. The robotic needle guide placement accuracy was $0.58 \pm 0.22\,mm$. The spatial displacement between the approved needle trajectory and registered seed position was $2.62 \pm 1.24\,mm$. The MRI only to MRI-CT matched seed registration deviated by $2.78 \pm 1.43\,mm$. However, the seed displacement and seed registration on the MRI images could further be improved by in-bore live imaging to guide the needle and registration methods able to handle image artifacts around the seeds.

Altogether, the TPS enables robotic seed-BT in a more flexible and automated workflow. The SIs demonstrate the potential of a fully integrated workflow of registering the needles for the feedback to the TPS and physician. The subsequent adaption algorithms enable to compensate seed displacements. The physician may benefit from the direct seed implantation feedback and the possibility to correct displacement errors in a way that the learning phase is shortened and the quality of implant is quickly raised.

6 Bibliography

References

[1] Nicholas G. Zaorsky, Brian J. Davis, Paul L. Nguyen, Timothy N. Showalter, Peter J. Hoskin, Yasuo Yoshioka, Gerard C. Morton, and Eric M. Horwitz. "The evolution of brachytherapy for prostate cancer". In: *Nature Reviews Urology* 14.7 (2017), pp. 415–439. ISSN: 1759-4820. DOI: 10.1038/nrurol.2017.76.

[2] Benj. Stockwell Barringer. "RADIUM IN THE TREATMENT OF PROSTATIC CARCINOMA". In: *Annals of Surgery* 80.6 (1924). ISSN: 0003-4932. URL: https://journals.lww.com/annalsofsurgery/Fulltext/1924/12010/RADIUM_IN_THE_TREATMENT_OF_PROSTATIC_CARCINOMA.7.aspx (Last accessed: April 26, 2023).

[3] R. H. Flocks. "Interstitial Irradiation Therapy With a Solution of Au^{198} as Part of Combination Therapy For Prostatic Carcinoma". In: *Journal of Nuclear Medicine* 5.9 (1964), pp. 691–705. ISSN: 0161-5505. URL: https://jnm.snmjournals.org/content/5/9/691 (Last accessed: April 26, 2023).

[4] Basil S. Hilaris, Willet F Whitmore Jr, Mostafa A Batata, and Harry Grabstald. "Radiation therapy and pelvic node dissection in the management of cancer of the prostate." In: *The American Journal of Roentgenology, Radium Therapy, and Nuclear Medicine* 121.4 (1974), pp. 832–838. DOI: 10.2214/ajr.121.4.832.

[5] William U. Shipley, George L. Nardi, Alfred M. Cohen, and C. Clifton Ling. "Iodine-125 implant and external beam irradiation in patients with localized pancreatic carcinoma. A comparative study to surgical resection". In: *Cancer* 45.4 (1980), pp. 709–714. DOI: 10.1002/1097-0142(19800215)45:4<709::AID-CNCR2820450416>3.0.CO;2-5.

[6] T. Peretz, D. Nori, B. Hilaris, S. Manolatos, L. Linares, L. Harrison, L. L. Anderson, Z. Fuks, and M. F. Brennan. "Treatment of primary unresectable carcinoma of the pancreas with I-125 implantation." In: *International Journal of Radiation Oncology, Biology, Physics* 17.5 (1989). 931–935, pp. 931–935. DOI: 10.1016/0360-3016(89)90138-7.

[7] Basil S. Hilaris, Dattatreyudu Nori, and Nael Martini. "Intraoperative radiotherapy in stage I and II lung cancer". In: *Seminars in Surgical Oncology* 3.1 (1987), pp. 22–32. DOI: 10.1002/ssu.2980030104.

[8] Rafael Martinez-Monge, Subir Nag, Carol A. Nieroda, and Edward W. Martin. "Iodine-125 brachytherapy in the treatment of colorectal adenocarcinoma metastatic to the liver". In: *Cancer* 85.6 (1999), pp. 1218–1225. DOI: 10.1002/(SICI)1097-0142(19990315)85:6<1218::AID-CNCR2>3.0.CO;2-F.

[9] Rogers CL, Theodore N, Dickman CA, Sonntag VK, Thomas T, Lam S, and Speiser BL. "Surgery and permanent 125I seed paraspinal brachytherapy for malignant tumors with spinal cord compression." In: *Int J Radiat Oncol Biol Phys.* 54.2 (October 2002), pp. 505–13. DOI: 10.1016/s0360-3016(02)02961-9.

[10] Peter J. Hoskin, Alessandro Colombo, Ann Henry, Peter Niehoff, Taran Paulsen Hellebust, Frank-Andre Siebert, and Gyorgy Kovacs. "GEC/ESTRO recommendations on high dose rate afterloading brachytherapy for localised prostate cancer: An update". In: *Radiotherapy and Oncology* 107.3 (June 2013), pp. 325–332. ISSN: 0167-8140. DOI: 10.1016/j.radonc.2013.05.002.

[11] Gustavo Arruda Viani, Caio Viani Arruda, Antonio Cassio Assis Pellizzon, and Ligia Issa De Fendi. "HDR brachytherapy as monotherapy for prostate cancer: A systematic review with meta-analysis". In: *Brachytherapy* 20.2 (2021), pp. 307–314. ISSN: 1538-4721. DOI: 10.1016/j.brachy.2020.10.009.

[12] Peter Grimm et al. "Comparative analysis of prostate-specific antigen free survival outcomes for patients with low, intermediate and high risk prostate cancer treatment by radical therapy. Results from the Prostate Cancer Results Study Group". In: *BJU International* 109.s1 (2012), pp. 22–29. DOI: 10.1111/j.1464-410X.2011.10827.x.

[13] W. James Morris, Scott Tyldesley, Sree Rodda, Ross Halperin, Howard Pai, Michael McKenzie, Graeme Duncan, Gerard Morton, Jeremy Hamm, and Nevin Murray. "Androgen Suppression Combined with Elective Nodal and Dose Escalated Radiation Therapy (the ASCENDE-RT Trial): An Analysis of Survival Endpoints for a Randomized Trial Comparing a Low-Dose-Rate Brachytherapy Boost to a Dose-Escalated External Beam Boost for High- and Intermediate-risk Prostate Cancer". In: *International Journal of Radiation Oncology, Biology, Physics* 98.2 (2017), pp. 275–285. ISSN: 0360-3016. DOI: 10.1016/j.ijrobp.2016.11.026.

[14] Peter J. Hoskin, Ana M. Rojas, Peter J. Bownes, Gerry J. Lowe, Peter J. Ostler, and Linda Bryant. "Randomised trial of external beam radiotherapy alone or combined with high-dose-rate brachytherapy boost for localised prostate cancer". In: *Radiotherapy and Oncology* 103.2 (May 2012), pp. 217–222. ISSN: 0167-8140. DOI: 10.1016/j.radonc.2012.01.007.

[15] Nicolas Mottet et al. "EAU-ESTRO-SIOG Guidelines on Prostate Cancer. Part 1: Screening, Diagnosis, and Local Treatment with Curative Intent". In: *European Urology* 71.4 (2017), pp. 618–629. ISSN: 0302-2838. DOI: 10.1016/j.eururo.2016.08.003.

[16] Bradley J. Stish, Brian J. Davis, Lance A. Mynderse, Robert H. McLaren, Christopher L. Deufel, and Richard Choo. "Low dose rate prostate brachytherapy". In: *Translational Andrology and Urology* 7.3 (2018). ISSN: 2223-4691. DOI: 10.21037/tau.2017.12.15.

[17] J. W. Schäfer, G. Welzel, L. Trojan, N. Eppler, K. Harrer, M. S. Michel, P. Alken, and F. Wenz. *Long-Term Health-Related Quality-of-Life Outcomes after Permanent Prostate Brachytherapy*. 2008. DOI: 10.1159/000162270.

[18] Daniel Buergy, Vincent Schneiberg, Joerg Schaefer, Grit Welzel, Lutz Trojan, Christian Bolenz, and Frederik Wenz. "Quality of life after low-dose rate-brachytherapy for prostate carcinoma - long-term results and literature review on QLQ-C30 and QLQ-PR25 results in published brachytherapy series". In: *Health and Quality of Life Outcomes* 16.1 (2018), p. 21. ISSN: 1477-7525. DOI: 10.1186/s12955-018-0844-8.

[19] Alfredo Polo, Carl Salembier, Jack Venselaar, and Peter Hoskin. "Review of intra-operative imaging and planning techniques in permanent seed prostate brachytherapy". In: *Radiotherapy and Oncology* 94.1 (2010), pp. 12–23. ISSN: 0167-8140. DOI: 10.1016/j.radonc.2009.12.012.

[20] Donald B Fuller, James A Koziol, and Anne C Feng. "Prostate brachytherapy seed migration and dosimetry: analysis of stranded sources and other potential predictive factors". In: *Brachytherapy* 3.1 (2004), pp. 10–19. ISSN: 1538-4721. DOI: 10.1016/j.brachy.2004.02.003.

[21] Nicolas Mottet et al. "EAU-EANM-ESTRO-ESUR-SIOG Guidelines on Prostate Cancer—2020 Update. Part 1: Screening, Diagnosis, and Local Treatment with Curative Intent". In: *European Urology* 79.2 (2021), pp. 243–262. ISSN: 0302-2838. DOI: 10.1016/j.eururo.2020.09.042.

[22] Bashar Al-Qaisieh, Josh Mason, Peter Bownes, Ann Henry, Louise Dickinson, Hashim U. Ahmed, Mark Emberton, and Stephen Langley. "Dosimetry Modeling for Focal Low-Dose-Rate Prostate Brachytherapy". In: *International Journal of Radiation Oncology, Biology, Physics* 92.4 (2015), pp. 787–793. ISSN: 0360-3016. DOI: 10.1016/j.ijrobp.2015.02.043.

[23] Stephen Langley, Jennifer Uribe, Santiago Uribe-Lewis, Adrian Franklin, Carla Perna, Alex Horton, Melanie Cunningham, Donna Higgins, Claire Deering, Sara Khaksar, and Robert Laing. "Hemi-ablative low-dose-rate prostate brachytherapy for unilateral localised prostate cancer". In: *BJU International* 125.3 (2020), pp. 383–390. DOI: 10.1111/bju.14948.

[24] Stephen Langley, Hashim U. Ahmed, Bashar Al-Qaisieh, David Bostwick, Louise Dickinson, Francisco Gomez Veiga, Peter Grimm, Stefan Machtens, Ferran Guedea, and Mark Emberton. "Report of a consensus meeting on focal low dose rate brachytherapy for prostate cancer". In: *BJU International* 109.s1 (2012), pp. 7–16. DOI: 10.1111/j.1464-410X.2011.10825.x.

[25] Thomas Brun, Jean-Marc Bachaud, Pierre Graff-Cailleaud, Bernard Malavaud, Daniel Portalez, Christian Popotte, Richard Aziza, Amélie Lusque, Thomas Filleron, and Soléakhéna Ken. "New approach of ultra-focal brachytherapy for low- and intermediate-risk prostate cancer with custom-linked I-125 seeds: A feasibility

study of optimal dose coverage". In: *Brachytherapy* 17.3 (May 2018), pp. 544–555. ISSN: 1538-4721. DOI: 10.1016/j.brachy.2018.01.011.

[26] Pierre Graff, Daniel Portalez, Amélie Lusque, Thomas Brun, Richard Aziza, Jonathan Khalifa, Mathieu Roumiguié, Marie-Laure (Quintyn Ranty), Thomas Filleron, Jean-Marc Bachaud, and Bernard Malavaud. "IDEAL 2a Phase II Study of Ultrafocal Brachytherapy for Low- and Intermediate-risk Prostate Cancer". In: *International Journal of Radiation Oncology, Biology, Physics* 102.4 (2018). Imaging in Radiation Oncology, pp. 903–911. ISSN: 0360-3016. DOI: 10.1016/j.ijrobp.2018.01.066.

[27] Tarun K. Podder et al. "AAPM and GEC-ESTRO guidelines for image-guided robotic brachytherapy: Report of Task Group 192". In: *Medical Physics* 41.10 (2014), p. 101501. DOI: 10.1118/1.4895013.

[28] Jean-Marc Cosset, Xavier Cathelineau, Georges Wakil, Noelle Pierrat, Olivier Quenzer, Dominique Prapotnich, Eric Barret, François Rozet, Marc Galiano, and Guy Vallancien. "Focal brachytherapy for selected low-risk prostate cancers: A pilot study". In: *Brachytherapy* 12.4 (July 2013), pp. 331–337. ISSN: 1538-4721. DOI: 10.1016/j.brachy.2013.02.002.

[29] Steven J. Frank et al. "The American Brachytherapy Society prostate brachytherapy LDR/HDR simulation workshops: Hands-on, step-by-step training in the process of quality assurance". In: *Brachytherapy* 19.6 (November 2020), pp. 787–793. ISSN: 1538-4721. DOI: 10.1016/j.brachy.2020.10.001.

[30] Jeffrey M. Martin, Elizabeth A. Handorf, Alexander Kutikov, Robert G. Uzzo, Justin E. Bekelman, Eric M. Horwitz, and Marc C. Smaldone. "The rise and fall of prostate brachytherapy: Use of brachytherapy for the treatment of localized prostate cancer in the National Cancer Data Base". In: *Cancer* 120.14 (2014), pp. 2114–2121. DOI: 10.1002/cncr.28697.

[31] W. Robert Lee, Allan F. deGuzman, Rick L. Bare, Mark G. Marshall, and David L. McCullough. "Postimplant analysis of transperineal interstitial permanent prostate brachytherapy: evidence for a learning curve in the first year at a single institution". In: *International Journal of Radiation Oncology, Biology, Physics* 46.1 (January 2000), pp. 83–88. ISSN: 0360-3016. DOI: 10.1016/S0360-3016(99)00359-4.

[32] Cordelia Hoinkis, Oliver W. Hakenberg, Dietmar Lehmann, Cornelia Winkler, Manfred P. Wirth, and Thomas Herrmann. "Evaluation of Dose-Volume Histograms after Prostate Seed Implantation". In: *Strahlentherapie und Onkologie* 180.9 (2004), pp. 550–556. ISSN: 1439-099X. DOI: 10.1007/s00066-004-1337-8.

[33] Peter Acher, Rick Popert, Janette Nichol, Louis Potters, Stephen Morris, and Ronald Beaney. "Permanent prostate brachytherapy: Dosimetric results and analysis of a learning curve with a dynamic dose-feedback technique". In: *International Journal of Radiation Oncology, Biology, Physics* 65.3 (2006), pp. 694–698. ISSN: 0360-3016. DOI: 10.1016/j.ijrobp.2006.01.035.

[34] Wang Zhongmin, Liu Yu, Liu Fenju, Chen Kemin, and Huang Gang. "Clinical efficacy of CT-guided iodine-125 seed implantation therapy in patients with advanced pancreatic cancer". In: *European Radiology* 20.7 (2010), pp. 1786–1791. ISSN: 1432-1084. DOI: 10.1007/s00330-009-1703-0.

[35] Liangrong Shi, Changping Wu, Jun Wu, Wenjie Zhou, Mei Ji, Hongyu Zhang, Jiemin Zhao, Yuanquan Huang, Honglei Pei, Zhong Li, Jingfang Ju, and Jingting Jiang. "Computed tomography-guided permanent brachytherapy for locoregional recurrent gastric cancer". In: *Radiation Oncology* 7.1 (2012), p. 114. ISSN: 1748-717X. DOI: 10.1186/1748-717X-7-114.

[36] Qianqian Cao, Hao Wang, Na Meng, Yuliang Jiang, Ping Jiang, Yang Gao, Suqing Tian, Chen Liu, Ruijie Yang, Junjie Wang, and Kaixian Zhang. "CT-guidance interstitial 125Iodine seed brachytherapy as a salvage therapy for recurrent spinal primary tumors". In: *Radiation Oncology* 9.1 (2014), p. 301. ISSN: 1748-717X. DOI: 10.1186/s13014-014-0301-8.

[37] Wang Junjie, Chai Shude, Wang Ruoyu, Zheng Guangjun, Zhang Kaixian, Huo Bin, Huo Xiaodong, Jiang Yuliang, Ji Zhe, Jiang Ping, and Peng Ran. "Expert consensus on computed tomography--assisted three-dimensional-printed coplanar template guidance for interstitial permanent radioactive ^{125}I seed implantation therapy." In: *Journal of Cancer Research & Therapeutics* 15.7 (2019), pp. 1430–1434. ISSN: 09731482. DOI: 10.4103/jcrt.JCRT_434_19.

[38] Xiaodong Ma, Zhiyong Yang, Shan Jiang, Bin Huo, Qiang Cao, Shude Chai, and Haitao Wang. "Effectiveness and safety of a robot-assisted 3D personalized template in 125I seed brachytherapy of thoracoabdominal tumors". In: *Journal of Contemporary Brachytherapy* 10.4 (2018), pp. 368–379. ISSN: 1689-832X. DOI: 10.5114/jcb.2018.77957.

[39] Xiaodong Ma, Zhiyong Yang, Shan Jiang, Guobin Zhang, Bin Huo, and Shude Chai. "Hybrid optimization based on non-coplanar needles for brachytherapy dose planning". eng. In: *Journal of contemporary brachytherapy* 11.31435434 (June 2019), pp. 267–279. ISSN: 2081-2841. DOI: 10.5114/jcb.2019.86167.

[40] Arman Smakic, Nils Rathmann, Michael Kostrzewa, Stefan O. Schönberg, Christel Weiß, and Steffen J. Diehl. "Performance of a Robotic Assistance Device in Computed Tomography-Guided Percutaneous Diagnostic and Therapeutic Procedures". In: *CardioVascular and Interventional Radiology* 41.4 (2018), pp. 639–644. ISSN: 1432-086X. DOI: 10.1007/s00270-017-1841-8.

[41] Andreas Rothfuss, Oliver Oesterle, Daniel Bürgy, Charles Nwankwo, Frank Schneider, Auguste van Poelgeest, Frederik Wenz, Jan Stallkamp, and Sven Clausen. "System and path planning algorithm for low-kV X-ray free-form surface irradiation". In: *The International Journal of Medical Robotics and Computer Assisted Surgery* 14.3 (2018). e1899 rcs.1899, e1899. DOI: 10.1002/rcs.1899.

[42] Michael Kostrzewa, Andreas Rothfuss, Torben Pätz, Markus Kühne, Stefan O. Schoenberg, Steffen J. Diehl, Jan Stallkamp, and Nils Rathmann. "Robotic Assistance System for Cone-Beam Computed Tomography-Guided Percutaneous Needle Placement". In: *CardioVascular and Interventional Radiology* 45.1 (2022), pp. 62–68. ISSN: 1432-086X. DOI: 10.1007/s00270-021-02938-7.

[43] AnthonyV. D'Amico, Robert Cormack, ClareM. Tempany, Sanjaya Kumar, George Topulos, HanneM. Kooy, and C. Norman Coleman. "Real-time magnetic resonance image-guided interstitial brachytherapy in the treatment of select patients with clinically localized prostate cancer". In: *International Journal of Radiation Oncology, Biology, Physics* 42.3 (1998), pp. 507–515. ISSN: 0360-3016. DOI: 10.1016/S0360-3016(98)00271-5.

[44] Hanne M. Kooy, Robert A. Cormack, George Mathiowitz, Clair Tempany, and Anthony V. D'Amico. "A software system for interventional magnetic resonance image-guided prostate brachytherapy". In: *Computer Aided Surgery* 5.6 (2000), pp. 401–413. DOI: 10.1002/igs.1002.

[45] Robert A Cormack, Clare M Tempany, and Anthony V D'Amico. "Optimizing target coverage by dosimetric feedback during prostate brachytherapy". In: *International Journal of Radiation Oncology, Biology, Physics* 48.4 (2000), pp. 1245–1249. ISSN: 0360-3016. DOI: 10.1016/S0360-3016(00)00742-2.

[46] V Lagerburg, M A Moerland, J H Seppenwoolde, and J J W Lagendijk. "Simulation of the artefact of an iodine seed placed at the needle tip in MRI-guided prostate brachytherapy". In: *Physics in Medicine & Biology* 53.5 (February 2008), N59. DOI: 10.1088/0031-9155/53/5/N01.

[47] E Beld, M A Moerland, F Zijlstra, M A Viergever, J J W Lagendijk, and P R Seevinck. "MR-based source localization for MR-guided HDR brachytherapy". In: *Physics in Medicine & Biology* 63.8 (April 2018), p. 085002. DOI: 10.1088/1361-6560/aab50b.

[48] Ellis Beld, Marinus A Moerland, Jochem R N van der Voort van Zyp, Max A Viergever, Jan J W Lagendijk, and Peter R Seevinck. "MRI artifact simulation for clinically relevant MRI sequences for guidance of prostate HDR brachytherapy". In: *Physics in Medicine & Biology* 64.9 (April 2019), p. 095006. DOI: 10.1088/1361-6560/ab15ed.

[49] Reyhaneh Nosrati, Abraam Soliman, Habib Safigholi, Masoud Hashemi, Matthew Wronski, Gerard Morton, Ana Pejović-Milić, Greg Stanisz, and William Y. Song. "MRI-based automated detection of implanted low dose rate (LDR) brachytherapy seeds using quantitative susceptibility mapping (QSM) and unsupervised machine learning (ML)". In: *Radiotherapy and Oncology* 129.3 (2018), pp. 540–547. ISSN: 0167-8140. DOI: 10.1016/j.radonc.2018.09.003.

[50] Geoffrey V. Martin, Thomas J. Pugh, Usama Mahmood, Rajat J. Kudchadker, Jihong Wang, Teresa L. Bruno, Tharakeswara Bathala, Pierre Blanchard, and Steven J. Frank. "Permanent prostate brachytherapy postimplant magnetic resonance imaging dosimetry using positive contrast magnetic resonance imaging markers". In: *Brachytherapy* 16.4 (2017). Magnetic Resonance Imaging-Based Brachytherapy, pp. 761–769. ISSN: 1538-4721. DOI: 10.1016/j.brachy.2017.04.004.

[51] Axel Krieger, Iulian I. Iordachita, Peter Guion, Anurag K. Singh, Aradhana Kaushal, Cynthia Menard, Peter A. Pinto, Kevin Camphausen, Gabor Fichtinger, and Louis L. Whitcomb. "An MRI-Compatible Robotic System With Hybrid Tracking for MRI-Guided Prostate Intervention". In: *IEEE Transactions on Biomedical Engineering* 58.11 (2011), pp. 3049–3060. DOI: 10.1109/TBME.2011.2134096.

[52] J. Adam Cunha, I-Chow Hsu, Jean Pouliot, Mack Roach III, Katsuto Shinohara, John Kurhanewicz, Galen Reed, and Dan Stoianovici. "Toward adaptive stereotactic robotic brachytherapy for prostate cancer: Demonstration of an adaptive workflow incorporating inverse planning and an MR stealth robot". In: *Minimally Invasive Therapy & Allied Technologies* 19.4 (2010). PMID: 20642386, pp. 189–202. DOI: 10.3109/13645706.2010.497000.

[53] Gregory S. Fischer, Iulian Iordachita, Csaba Csoma, Junichi Tokuda, Simon P. DiMaio, Clare M. Tempany, Nobuhiko Hata, and Gabor Fichtinger. "MRI-Compatible Pneumatic Robot for Transperineal Prostate Needle Placement". In: *IEEE/ASME Transactions on Mechatronics* 13.3 (2008), pp. 295–305. DOI: 10.1109/TMECH.2008.924044.

[54] J. G. R. Bomers, D. G. H. Bosboom, G. H. Tigelaar, J. Sabisch, J. J. Fütterer, and D. Yakar. "Feasibility of a 2nd generation MR-compatible manipulator for transrectal prostate biopsy guidance". In: *European Radiology* 27.4 (2017), pp. 1776–1782. ISSN: 1432-1084. DOI: 10.1007/s00330-016-4504-2.

[55] Nicolas Linder, Alexander Schaudinn, Tim-Ole Petersen, Nikolaos Bailis, Patrick Stumpp, Lars-Christian Horn, Jens-Uwe Stolzenburg, Thomas Kahn, Michael Moche, and Harald Busse. "In-bore biopsies of the prostate assisted by a remote-controlled manipulator at 1.5 T". In: *Magnetic Resonance Materials in Physics, Biology and Medicine* 32.5 (2019), pp. 599–605. ISSN: 1352-8661. DOI: 10.1007/s10334-019-00751-5.

[56] I. Kuhlemann, P. Jauer, F. Ernst, and A. Schweikard. "Robots with seven degrees of freedom: Is the additional DoF worth it?" In: *2016 2nd International Conference on Control, Automation and Robotics (ICCAR)*. 2016, pp. 80–84. DOI: 10.1109/ICCAR.2016.7486703.

[57] Timmy Siauw, Adam Cunha, Dmitry Berenson, Alper Atamtürk, I-Chow Hsu, Ken Goldberg, and Jean Pouliot. "NPIP: A skew line needle configuration optimization system for HDR brachytherapy". In: *Medical Physics* 39.7Part1 (2012), pp. 4339–4346. DOI: 10.1118/1.4728226.

[58] Dominik F. Bauer, Anne Adlung, Irène Brumer, Alena-Kathrin Golla, Tom Russ, Eva Oelschlegel, Fabian Tollens, Sven Clausen, Philipp Aumüller, Lothar R. Schad, Dominik Nörenberg, and Frank G. Zöllner. "An anthropomorphic pelvis phantom for MR-guided prostate interventions". In: *Magnetic Resonance in Medicine* 87.3 (2022), pp. 1605–1612. DOI: 10.1002/mrm.29043.

[59] Philip Mayer. "Inverse Radiation Treatment Planning for Robot Assisted, Iod-Seed-Based, Extraprostatic Brachytherapy". MA thesis. University Medical Centre Mannheim, University Heidelberg, June 2018.

[60] Mirjam Lena Dannert. "TPS Implementation of Robotic Guided Transrectal Prostate LDR Seed-Brachytherapy". MA thesis. University Medical Centre Mannheim, University Heidelberg, November 2021.

[61] Philipp Aumüller, Andreas Rothfuss, Martin Polednik, Yasser Abo-Madyan, Michael Ehmann, Frank A. Giordano, and Sven Clausen. "Multiple direction needle-path planning and inverse dose optimization for robotic low-dose rate brachytherapy". In: *Zeitschrift für Medizinische Physik* (2021). ISSN: 0939-3889. DOI: 10.1016/j.zemedi.2021.06.003.

[62] Philipp Aumüller, Andreas Rothfuss, Michael Ehmann, Frank A. Giordano, and Sven Clausen. "Simulated liver implantation (SLIM): Towards fully robotic LDR brachytherapy for liver tumors. Postersession 1803". In: *Radiotherapy and Oncology* 170 (May 2022), S1607–S1608. ISSN: 0167-8140. DOI: 10.1016/S0167-8140(22)03766-5.

[63] Jens T. Olesen. *DICOM-RT to Matlab*. URL: https://github.com/ulrikls/dicomrt2matlab (Last accessed: April 26, 2023).

[64] Herbert Edelsbrunner and Ernst P. Mücke. "Three-dimensional alpha shapes". In: *ACM Trans. Graph.* 13.1 (January 1994), pp. 43–72. ISSN: 0730-0301. DOI: 10.1145/174462.156635.

[65] *alphaShape: Polygons and polyhedra from points in 2-D and 3-D*. URL: https://ch.mathworks.com/help/matlab/ref/alphashape.html (Last accessed: April 4, 2023).

[66] Ravinder Nath, William S. Bice, Wayne M. Butler, Zhe Chen, Ali S. Meigooni, Vrinda Narayana, Mark J. Rivard, and Yan Yu. "AAPM recommendations on dose prescription and reporting methods for permanent interstitial brachytherapy for prostate cancer: Report of Task Group 137". In: *Medical Physics* 36.11 (2009), pp. 5310–5322. DOI: 10.1118/1.3246613.

[67] Nelson N. Stone, Louis Potters, Brian J. Davis, Jay P. Ciezki, Michael J. Zelefsky, Mack Roach, Paul A. Fearn, Michael W. Kattan, and Richard G. Stock. "Customized Dose Prescription for Permanent Prostate Brachytherapy: Insights From a Multicenter Analysis of Dosimetry Outcomes". In: *International Journal of Radiation Oncology, Biology, Physics* 69.5 (2007), pp. 1472–1477. ISSN: 0360-3016. DOI: 10.1016/j.ijrobp.2007.05.002.

[68] M. D. Stock Richard G, M. D. Stone Nelson N, M. S. Tabert Andrea, M. D. Iannuzzi Christopher, and Ph. D. DeWyngaert J.Keith. "A Dose-Response Study for I-125 Prostate Implants". In: *International Journal of Radiation Oncology, Biology, Physics* 41.1 (April 1998), pp. 101–108. ISSN: 0360-3016. DOI: 10.1016/S0360-3016(98)00006-6.

[69] Kent Wallner, Jitendra Roy, and Louis Harrison. "Dosimetry guidelines to minimize urethral and rectal morbidity following transperineal I-125 prostate brachytherapy". In: *International Journal of Radiation Oncology, Biology, Physics* 32.2 (1995), pp. 465–471. ISSN: 0360-3016. DOI: 10.1016/0360-3016(94)00599-G.

[70] Mark J. Rivard, Bert M. Coursey, Larry A. DeWerd, William F. Hanson, M. Saiful Huq, Geoffrey S. Ibbott, Michael G. Mitch, Ravinder Nath, and Jeffrey F. Williamson. "Update of AAPM Task Group No. 43 Report: A revised AAPM protocol for brachytherapy dose calculations". In: *Medical Physics* 31.3 (2004), pp. 633–674. DOI: 10.1118/1.1646040.

[71] Mark J. Rivard, Facundo Ballester, Wayne M. Butler, Larry A. DeWerd, Geoffrey S. Ibbott, Ali S. Meigooni, Christopher S. Melhus, Michael G. Mitch, Ravinder Nath, and Panagiotis Papagiannis. "Erratum: "Supplement 2 for the 2004 update of the AAPM Task Group No. 43 Report: Joint recommendations by the AAPM and GEC-ESTRO" [Med. Phys. Vol 44 (9), e297–e338 (2017)]". In: *Medical Physics* 45.2 (2018), pp. 971–974. DOI: 10.1002/mp.12728.

[72] Ravinder Nath, Lowell L. Anderson, Gary Luxton, Keith A. Weaver, Jeffrey F. Williamson, and Ali S. Meigooni. "Dosimetry of interstitial brachytherapy sources: Recommendations of the AAPM Radiation Therapy Committee Task Group No. 43". In: *Medical Physics* 22.2 (1995), pp. 209–234. DOI: 10.1118/1.597458.

[73] *scatteredInterpolant: Interpolate 2-D or 3-D scattered data*. URL: https://ch.mathworks.com/help/matlab/ref/scatteredinterpolant.html (Last accessed: April 25, 2023).

[74] Moyed Miften, Arthur Olch, Dimitris Mihailidis, Jean Moran, Todd Pawlicki, Andrea Molineu, Harold Li, Krishni Wijesooriya, Jie Shi, Ping Xia, Nikos Papanikolaou, and Daniel A. Low. "Tolerance limits and methodologies for IMRT measurement-based verification QA: Recommendations of AAPM Task Group No. 218". In: *Medical Physics* 45.4 (2018), e53–e83. DOI: 10.1002/mp.12810.

[75] *inShape: Determine if point is inside alpha shape*. URL: https://ch.mathworks.com/help/matlab/ref/alphashape.inshape.html (Last accessed: April 4, 2023).

[76] Sua Yoo, Michael E Kowalok, Bruce R Thomadsen, and Douglass L Henderson. "Treatment planning for prostate brachytherapy using region of interest adjoint functions and a greedy heuristic". In: *Physics in Medicine and Biology* 48.24 (December 2003), pp. 4077–4090. DOI: 10.1088/0031-9155/48/24/006.

[77] *simulannealbnd: Find minimum of function using simulated annealing algorithm.* URL: https://ch.mathworks.com/help/gads/simulannealbnd.html (Last accessed: April 4, 2023).

[78] Jean Pouliot, Daniel Tremblay, Jean Roy, and Santo Filice. "Optimization of permanent ^{125}I prostate implants using fast simulated annealing". In: *International Journal of Radiation Oncology, Biology, Physics* 36.3 (October 1996), pp. 711–720. ISSN: 0360-3016. DOI: 10.1016/S0360-3016(96)00365-3.

[79] Barbara Stam, Heike Peulen, Maddalena M. G. Rossi, José S. A. Belderbos, and Jan-Jakob Sonke. "Validation of automatic segmentation of ribs for NTCP modeling". In: *Radiotherapy and Oncology* 118.3 (March 2016), pp. 528–534. ISSN: 0167-8140. DOI: 10.1016/j.radonc.2015.12.014.

[80] Michiel R. van den Bosch, Irene M. Lips, Vera Lagerburg, Marco van Vulpen, Jan J. W. Lagendijk, and Marinus A. Moerland. "Feasibility of adequate dose coverage in permanent prostate brachytherapy using divergent needle insertion methods". In: *Radiotherapy and Oncology* 86.1 (January 2008), pp. 120–125. ISSN: 0167-8140. DOI: 10.1016/j.radonc.2007.10.037.

[81] Matthias Guckenberger et al. "Characterisation and classification of oligometastatic disease: a European Society for Radiotherapy and Oncology and European Organisation for Research and Treatment of Cancer consensus recommendation". In: *The Lancet Oncology* 21.1 (2020), e18–e28. ISSN: 1470-2045. DOI: 10.1016/S1470-2045(19)30718-1.

[82] Theo Ruers et al. "Local Treatment of Unresectable Colorectal Liver Metastases: Results of a Randomized Phase II Trial". In: *JNCI: Journal of the National Cancer Institute* 109.9 (March 2017). djx015. ISSN: 0027-8874. DOI: 10.1093/jnci/djx015.

[83] David A. Palma et al. "Stereotactic Ablative Radiotherapy for the Comprehensive Treatment of Oligometastatic Cancers: Long-Term Results of the SABR-COMET Phase II Randomized Trial". In: *Journal of Clinical Oncology* 38.25 (2020). PMID: 32484754, pp. 2830–2838. DOI: 10.1200/JCO.20.00818.

[84] Lara Hathout, Michael R. Folkert, Marisa A. Kollmeier, Yoshiya Yamada, Gil'ad N. Cohen, and Michael J. Zelefsky. "Dose to the Bladder Neck Is the Most Important Predictor for Acute and Late Toxicity After Low-Dose-Rate Prostate Brachytherapy: Implications for Establishing New Dose Constraints for Treatment Planning". In: *International Journal of Radiation Oncology, Biology, Physics* 90.2 (October 2014), pp. 312–319. ISSN: 0360-3016. DOI: 10.1016/j.ijrobp.2014.06.031.

[85] Michael F. Sarosdy. "Urinary and rectal complications of contemporary permanent transperineal brachytherapy for prostate carcinoma with or without external beam radiation therapy". In: *Cancer* 101.4 (2004), pp. 754–760. DOI: 10.1002/cncr.20446.

[86] Xuesong Dai, Yongde Zhang, Jingang Jiang, and Bing Li. "Image-guided robots for low dose rate prostate brachytherapy: Perspectives on safety in design and use". In: *The International Journal of Medical Robotics and Computer Assisted Surgery* 17.3 (2021), e2239. DOI: 10.1002/rcs.2239.

[87] Amar U. Kishan et al. "Radical Prostatectomy, External Beam Radiotherapy, or External Beam Radiotherapy With Brachytherapy Boost and Disease Progression and Mortality in Patients With Gleason Score 9-10 Prostate Cancer". In: *JAMA* 319.9 (March 2018), pp. 896–905. ISSN: 0098-7484. DOI: 10.1001/jama.2018.0587.

[88] Thomas Feutren and Fernanda G. Herrera. "Prostate irradiation with focal dose escalation to the intraprostatic dominant nodule: a systematic review". In: *Prostate international* 6.30140656 (September 2018), pp. 75–87. ISSN: 2287-903X. DOI: 10.1016/j.prnil.2018.03.005.

[89] Linda G. W. Kerkmeijer et al. "Focal Boost to the Intraprostatic Tumor in External Beam Radiotherapy for Patients With Localized Prostate Cancer: Results From the FLAME Randomized Phase III Trial". In: *Journal of Clinical Oncology* 39.7 (2021). PMID: 33471548, pp. 787–796. DOI: 10.1200/JCO.20.02873.

7 Curriculum vitae

Personal Details

Family name	Aumüller
First name	Philipp
Title	M.Sc.
Date of birth	16 September 1989
Place of birth	Augsburg

School education

Sep. 1997 – Jul. 2000	**Primary school**, *Herrenbach*, Augsburg
Sep. 2000 – Jul. 2009	**Secondary school**, *Holbein Gymnasium*, Augsburg
26 June 2009	**Abitur**

Academic education

Oct. 2010 – Jul. 2014	**Bachelor studies Physics**, *Karlsruher Institute for Technology*, *Grade: 2,7*
07 July 2014	**Bachelor of Science**
Oct. 2014 – May 2017	**Master studies Physics**, *University of Regensburg*, *Grade: 1,8* Courses i.a. Medical Physics, Light Matter Interaction, Semiconductor Physics
03 May 2017	**Master of Science**
Apr. 2019 – Sep. 2020	**Medical Physics: Radiation protection courses**, *University of Kaiserslautern* Courses: Radiation Protection, Radiotherapy, Nuclear Medicine and Diagnostic Radiology

Work

Sep. 2017 – Mar. 2018	**Software engineer, Software tester and Consultant**, *OptWare GmbH*, Regensburg
Aug. 2018 – Dec. 2021	**Medical physicist in training**, *Medical Faculty of Mannheim of the University of Heidelberg*
since Jun. 2021	**Expertise of Radiation Protection**, *Brachytherapy*, External Beam Radiotherapy, Kilovoltage Radiotherapy
since Jan. 2022	**Medical physicist**, *University Medicine Mannheim*

Mannheim, 08 May 2023

8 Own publications

[P.1] **Philipp Aumüller**, Philip Mayer, Oliver Oesterle, Andreas Rothfuss, Frank A. Giordano, and Sven Clausen. "Treatment planning system for robotic LDR-Brachytherapy. Postersession P23". In: *50. Jahrestagung der Deutschen Gesellschaft für Medizinische Physik in Stuttgart, Hrgs. Nils Wegner, Christian Gromoll.* September 2019, p. 207. ISBN: 978-3-948023-08-9. URL: https://www.dgmp.de/de-DE/131/dgmp-tagungsbaende/ (Last accessed: April 26, 2023).

[P.2] **Philipp Aumüller**, Andreas Rothfuss, Michael Ehmann, Frank A. Giordano, and Sven Clausen. "Simulated liver implantation (SLIM): Towards fully robotic LDR brachytherapy for liver tumors. Postersession 1803". In: *Radiotherapy and Oncology* 170 (May 2022), S1607–S1608. ISSN: 0167-8140. DOI: 10.1016/S0167-8140(22)03766-5.

[P.3] **Philipp Aumüller**, Andreas Rothfuss, Oliver Oesterle, Frank A. Giordano, and Sven Clausen. "Path-planning-algorithm for robotic LDR-brachytherapy. Postersession Day 1". In: *4th Image-Guided Interventions Conference, Digitalization in Medicine*. M²OLIE, STIMULATE. UMM, Mannheim, November 2019.

[P.4] **Philipp Aumüller**, Andreas Rothfuss, Martin Polednik, Yasser Abo-Madyan, Michael Ehmann, Frank A. Giordano, and Sven Clausen. "Multiple direction needle-path planning and inverse dose optimization for robotic low-dose rate brachytherapy". In: *Zeitschrift für Medizinische Physik* (2021). ISSN: 0939-3889. DOI: 10.1016/j.zemedi.2021.06.003.

[P.5] **Philipp Aumüller**, Andreas Rothfuss, Martin Polednik, Michael Ehmann, Frank A. Giordano, and Sven Clausen. "Planungssystem für robotische LDR-Brachytherapie. Presentation 39, Session 7: Brachytherapie und IORT". In: *51. Jahrestagung der Deutschen Gesellschaft für Medizinische Physik als digitaler Kongress, Hrgs. Bernhard Sattler, Ulrich Wolf.* Deutsche Gesellschaft für Medizinische Physik (DGMP) e.V. September 2020, p. 67. ISBN: 978-3-948023-10-2. URL: https://www.dgmp.de/de-DE/131/dgmp-tagungsbaende/ (Last accessed: April 26, 2023).

[P.6] Dominik Bauer, Irène Brumer, Anne Adlung, Alena-Kathrin Golla, Tom Russ, Eva Oelschlegl, Fabian Tollens, Sven Clausen, **Philipp Aumüller**, Lothar Schad, Dominik Nörenberg, and Frank Zöllner. "An Anthropomorphic Pelvis Phantom for MR-guided Prostate Biopsy. Session 3: iMRI Hardware". In: *5th Conference on Image–Guided Interventions (IGIC) Medical Imaging, Medical Devices and Robot Applications for Image–Guided Interventions.* October 2021, p. 23. URL: https://www.igic.de/deutsch/igic-2021/proceedings/index.html (Last accessed: April 4, 2023).

[P.7] Dominik F. Bauer, Anne Adlung, Irène Brumer, Alena-Kathrin Golla, Tom Russ, Eva Oelschlegel, Fabian Tollens, Sven Clausen, **Philipp Aumüller**, Lothar R. Schad, Dominik Nörenberg, and Frank G. Zöllner. "An anthropomorphic pelvis phantom for MR-guided prostate interventions". In: *Magnetic Resonance in Medicine* 87.3 (2022), pp. 1605–1612. DOI: 10.1002/mrm.29043.

9 Acknowledgement

Herrn Prof. Dr. med. Frank Giordano danke ich für die Betreuung dieser Arbeit und die nützlichen Kommentare vor allem bei der Veröffentlichung der Ergebnisse.

Herrn Dr. sc. hum. Sven Clausen danke ich für die Überlassung dieses tollen Themas und die fachliche Unterstützung all die letzten Jahre.

Außerdem möchte ich Herrn Dr. sc. hum. Polednik, Frau Mirjam Lena Dannert, Herrn Dr. sc. hum. Dominik Bauer für ihre gute Zusammenarbeit und Unterstützung danken. Nicht vergessen werden sollen die Stabstelle für medizinische Physik und Strahlenschutz sowie der Forschungscampus M^2OLIE, die ein interessantes Forschungsumfeld gegeben haben.

Herrn Dr. Paul Schlüter danke ich für das aufmerksame Korrekturlesen und das aufrichtige und umfassende Feedback.

Nicht zuletzt möchte ich meiner Familie und Liebsten für die Unterstützung danken.